

The Critical Current Density of $\text{YBa}_2\text{Cu}_3\text{O}_{7-x}$ Coated Conductors

by

Sang Il Kim

A dissertation submitted in partial fulfillment of
the requirements for the degree of

Doctor of Philosophy
(Materials Science Program)

at the
University of Wisconsin – Madison

2007

ABSTRACT

The Critical Current Density of $\text{YBa}_2\text{Cu}_3\text{O}_{7-x}$ Coated Conductors

Sang Il Kim

Under the supervision of Professor David C. Larbalestier
at the University of Wisconsin – Madison

The critical current density J_c of the 2nd generation high temperature superconducting wires of $\text{YBa}_2\text{Cu}_3\text{O}_{7-x}$ (YBCO), so-called YBCO coated conductors, is determined by the connectivity of the polycrystalline grain network and by vortex pinning. The aim of this work is to explore these two key scientific issues.

Current obstruction effects of the grain boundary network were first studied by measuring variable width tracks cut in variously-textured *ex situ* coated conductors. We found that the global texture exercises a significant effect on J_c especially in low fields. We then grew low angle (6-9°) [001]-tilt bicrystal YBCO films with controlled doping so as to study the influence that variable size and charge segregants would have on the inter-grain J_c . The beneficial effects of Ca doping was already proven, but here we were able to show that the optimum doping of low angle grain boundaries was obtained with the smaller substitutions of 15% Ca for Y, rather than the 30% previously employed. We then studied Ca-doping in the small rare-earth (RE) ion Yb variant of the RE-123 structure, $\text{YbBa}_2\text{Cu}_3\text{O}_{7-x}$, and the influence of substitutions for Y of the large RE ion Nd in $\text{YBa}_2\text{Cu}_3\text{O}_{7-x}$. We found that strain- and charge-driven segregation to the grain boundary was consistent with the segregation model of Gurevich. Very interestingly, the 6° Nd-doped

YBCO grain boundaries exhibited no degradation of inter-grain J_c compared to the intragrain J_c without significant T_c reduction. Regular YBCO exhibits reduction of the intergranular J_c already at 2-3°.

The vortex pinning was then studied by sequential ion milling of YBCO films with various vortex pinning microstructures. Pure YBCO films without strong pins exhibited two-dimensional collective pinning behavior and thermal fluctuation depinning effect, and thus J_c fell off fast with increasing thickness, magnetic field and temperature. In contrast, a YBCO film with dense, insulating, nanoscale pins exhibited strong three-dimensional pinning behavior, a high and uniform J_c through thickness and an enhanced irreversibility field H_{irr} . Analysis of the through-thickness properties of *ex situ* high J_c coated conductors showed them to be well into the three-dimensional strong pinning limit but to show some materials degradation effects in thicker films, due to artifacts of the the *ex situ* conversion process. Collectively, this study clearly shows the route to strong vortex pinning films.

In summary, we performed experiments on key aspects of J_c in YBCO films, and found ways (i) to minimize the obstruction of low angle grain boundaries by cation segregation engineering, and (ii) to avoid the generally observed degradation of J_c with increasing thickness by introducing dense arrays of insulating nanoparticles which push the vortex pinning into the strong three-dimensional pinning limit.

TABLE OF CONTENTS

Abstract	i
Chapter I. Introduction	1
I.1 YBa ₂ Cu ₃ O _{7-x} Coated Conductors	1
I.1.1 Cuprate high temperature superconductors and (RE)Ba ₂ Cu ₃ O _{7-x} System	2
I.1.2 YBCO coated conductors	5
I.1.3 Performance requirements of coated conductors	6
I.2 Scientific challenges of coated conductors	7
I.2.1 Weak superconducting coupling across grain boundaries	7
I.2.2 Thickness dependence of the critical current density	9
I.2.3 Flux pinning issue	10
I.3 Substrates and Buffer Layers in Coated Conductors	11
I.4 Superconducting Layer in Coated Conductors	12
I.4.1 <i>Ex situ</i> MOD process	12
I.4.2 <i>In situ</i> Pulsed Laser Deposition process	13
I.5 Motivation and outline	14
I.5.1 Motivation	14
I.5.2 Structure of the thesis	15
References	17
Chapter II. Experiment	20
II.1 Electromagnetic characterization	21
II.1.1 Electromagnetic characterization	20

II.1.2 Analysis of electromagnetic characteristics	22
II.2 YBCO thin film deposition by pulsed laser deposition	26
II.2.1 Brief introduction to pulsed laser deposition	26
II.2.2 PLD system setup	27
II.3 Other techniques	30
II.3.1 Electron backscatter diffraction, EBSD	30
II.3.2 Magneto-optic Imaging (MOI)	31
II.3.3 X-ray Diffraction (XRD)	32
References	34
Chapter III. Influence of the grain boundary network on the critical current density ...	36
III.1 Introduction	36
III.2 Experimental Details	40
III.3 Influence of global texture on the critical current density	42
III.4 Influence of the number of grains within the bridge width	46
III.5 Discussion	51
III.6 Summary	57
References	58
Chapter IV. Improvement of low angle grain boundary transparency	61
IV.1 Introduction to carrier doping effect on YBCO	64
IV.1.1 Charge carrier doping in YBCO grains	64
IV.1.2 Charge carrier doping at YBCO grain boundaries	70

IV.2 Flux Flow Behavior at Grain Boundaries	77
IV.3 Ca-doping in low angle YBCO grain boundaries	79
IV.4 Grain Boundary properties of $\text{Yb}_{0.9}\text{Ca}_{0.1}\text{Ba}_2\text{Cu}_3\text{O}_{7-\delta}$	94
IV.5 Grain Boundary properties of $\text{Y}_{0.9}\text{Nd}_{0.1}\text{Ba}_2\text{Cu}_3\text{O}_{7-\delta}$	101
IV.5.1 Background	101
IV.5.2 Growth of $\text{Y}_{0.9}\text{Nd}_{0.1}\text{Ba}_2\text{Cu}_3\text{O}_{7-\delta}$ at 300 mTorr	104
IV.5.3 Growth of $\text{Y}_{0.9}\text{Nd}_{0.1}\text{Ba}_2\text{Cu}_3\text{O}_{7-\delta}$ at 250 mTorr	105
IV.5.4 Growth of $\text{Y}_{0.9}\text{Nd}_{0.1}\text{Ba}_2\text{Cu}_3\text{O}_{7-\delta}$ at 200 mTorr	108
IV.5.5 Nd doping effect on YBCO	110
IV.6 Summary	111
References	115

Chapter V. Sequential ion milling studies of the critical current density in films and coated conductors of YBCO with varying vortex pinning microstructure 117

V.1 Introduction	117
V.2 Sample sets	119
V.3 Thickness dependence of J_c in PLD YBCO thin films	120
V.3.1 Experiments	121
V.3.2 Results	122
V.3.3 Discussion	134
V.4 Thickness dependence of J_c in YBCO film containing a high density of insulating, vortex-pinning nano-precipitates	138
V.4.1 Experiments	138
V.4.2 Results	139

V.4.3 Discussion	143
V.5 Thickness dependence of J_c in MOD YBCO coated conductors	145
V.5.1 Experiment	146
V.5.2 Results	147
V.5.3 Discussion	158
V.6 Two dimensional collective pinning vs. three dimensional strong pinning	165
V.7 Summary	169
References	171
Chapter VI. Summary	174
VI.1 Grain Boundaries in coated conductors	174
VI.2 Thickness dependence of critical current density in coated conductors	177
APPENDIX : Calculation of porosity from effective medium theory	179

Chapter I. Introduction

I.1 $\text{YBa}_2\text{Cu}_3\text{O}_{7-x}$ Coated Conductors

Since the discovery of high-temperature superconductors (HTS) in the late 1980s [1], great attention has been devoted to searching for ways to produce affordable flexible conducting HTS wires with high current density, which can use for many applications including magnetically levitated trains (MagLev), transformers, generators, motors, magnetic resonance imaging (MRI), fault current limiter, superconducting magnetic energy storage (SMES), superconducting magnets, and electricity transmission cables [2]. The $(\text{Bi,Pb})_2\text{Sr}_2\text{Ca}_2\text{Cu}_3\text{O}_3$ (BSCCO) tapes, the 1st generation HTS wires, have already been fabricated in 1000 m class long and several applications have been demonstrated [3,4]. However, the BSCCO wires exhibit rather low critical current density J_c under high magnetic fields in the range of 77 K (liquid nitrogen temperature), which limits the usage only at around 20 K for many practical in-field applications. Additionally, the cost reduction has been limited due to its relatively high volumetric silver ratio. Development of the 2nd generation HTS wires with $\text{YBa}_2\text{Cu}_3\text{O}_{7-x}$ (YBCO) or $(\text{RE})\text{Ba}_2\text{Cu}_3\text{O}_{7-x}$ (RE123; RE stands for a rare earth element) is expected to overcome these weak points of the 1st generation BSCCO wires, since the YBCO and RE123 essentially have a high J_c potential at liquid nitrogen temperature 77K and in high magnetic fields. Recently, collaborated researches on the 2nd generation YBCO-based wires (so-called YBCO coated conductors, CC) between universities, national laboratories, and industries around the world are being

made more extensively to achieve robust, high-performance *YBCO Coated Conductors* which could revolutionize the electric power grid and various electric power applications.

This chapter starts with introducing YBCO and RE123 systems, which is adapted as superconducting materials of the 2nd generation HTS wires. Then, how the YBCO materials can be developed as useful conductor forms will be discussed, followed by discussion on the performance requirement for various applications.

I.1.1 Cuprate high temperature superconductors and (RE)Ba₂Cu₃O_{7-x} System

Many of cuprates (copper-oxide-based materials), including YBCO [5], BSCCO [6], Hg-compounds [7], and Tl-compounds [8] exhibits high superconducting critical temperature T_c well above the liquid nitrogen temperature of 77 K, thus there has been tremendous endeavor to produce commercial and industrial application to take advantages of cost efficiency originated from a cheap cryogen (liquid nitrogen) technologically as well as large interest in fundamental mechanism of high T_c scientifically. However, their complex structure and incomplete physics understanding have retarded the development of applications. Among these cuprate HTS, YBCO has been considered as one of the most promising candidates for potential HTS wire applications. Very recently, (RE)Ba₂Cu₃O_{7-x} (RE123; RE is a rare earth element) materials are also vastly being investigated to take advantages of superior performance – higher T_c , higher irreversibility field H_{irr} , and better pinning.

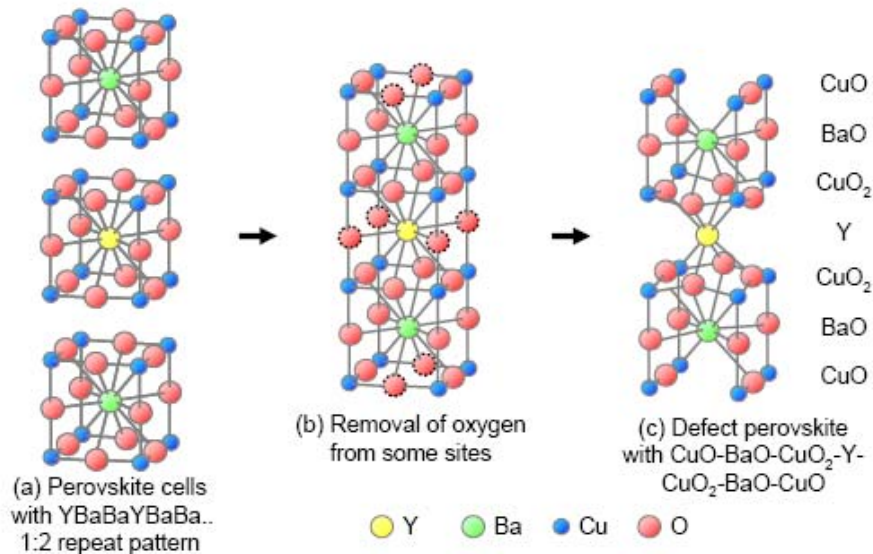


Figure I.1 Crystal structure of YBCO as an oxygen-deficient perovskite.

The cuprate superconductors exhibit large anisotropies, resulting in two-dimensionality in their physical properties. This large anisotropy is due to a complex, layered perovskite crystal structure (Figure I.1), which is believed to be essential for the high T_c . The layers are composed of CuO_2 planes, separated from each other by planes of various other oxides and rare earths (called as charge reservoirs or insulating planes). On both experimental and theoretical grounds, it is understood that superconductivity and charge transport are mostly confined to the CuO_2 planes. For example, YBCO is a layered perovskite structure centered on a Y layer, around which are stacked the CuO_2 plane of strong superconductivity and double charge-reservoir layers of O-Ba-O and O-Cu (see Figure I.1(c)). Cuprate superconductors are hard mechanically and very brittle, exhibiting very poor ductility.

YBCO exhibits relatively low anisotropy (electron mass anisotropy $\gamma = (m_c/m_{ab})^{0.5} \sim 5-7$), compare to other HTS materials, which makes it the most promising HTS materials for commercial applications. It is because the charge reservoir layers are metallic. For instance BSCCO has very large γ values of 30 minimum. Adequately textured YBCO thin films have high J_c above a few MA/cm² at self field at 77K, and relatively high in-field performance (irreversibility field at 77 K $\sim 6-7$ T). It is also known that the J_c and irreversibility field can be increased by introducing many kinds of pinning centers. In addition, YBCO indeed exhibits vastly improved in-field performance in the temperature range 30 – 65 K, where closed cycle cooling system based on mechanical cryocoolers can be used. The lattice structure is an orthorhombic with lattice parameters, $a=3.82 \text{ \AA}$, $b=3.89 \text{ \AA}$, and $c =11.68 \text{ \AA}$ when x value ($\text{YBa}_2\text{Cu}_3\text{O}_{7-x}$) is ~ 0 or very small, whereas in case of $x=1$, it becomes a tetragonal and non-superconducting. In addition, YBCO is non-toxic and environmental-friendly.

Recently, RE123 is also considered as alternatives of YBCO in coated conductor researches. The examples of rare earth ions are Yb, Tm, Er, Ho, Y, Dy, Gd, Eu, Sm, and Nd (in order of ionic size – smaller to larger). Many RE123 compounds exhibit mostly similar physical properties to YBCO. The lattice parameters are systematically correlated with ion radius of rare earth ions and T_c is ranging from 90 to 95 K, also exhibiting rough systematic correlation with ion radius of rare earth ions. However, it is expected RE123 compounds containing larger rare earth ions (Eu, Sm, and Nd) can behave rather differently to YBCO since substitution of the rare earth ion for the Ba is allowed. Only non-superconducting $\text{PrBa}_2\text{Cu}_3\text{O}_{7-x}$ is the exception on RE123, which is used in tunneling devices.

I.1.2 YBCO coated conductors

A superconducting wire is a fundamental structure for many other superconducting applications, which is usually the composite material structure. Low temperature superconductors (LTS) such as NbTi and Nb₃Sn have been made in the multi-filamentary wire forms in which many superconducting filaments are embedded in a matrix of a normal metal. However, HTS are hard to be made in the wire form with useful J_c due to high anisotropy and weak coupling across grain boundaries. At present, the HTS conductor in production [3,4] is Ag-sheathed multi-filamentary BSCCO compound wire (the 1st generation HTS wire) in the tape form (Figure I.2). While long lengths of BSCCO wire can be manufactured, its superconducting properties and commercial price yet make it not quite suitable for high J_c in high magnetic field application at around 77 K.

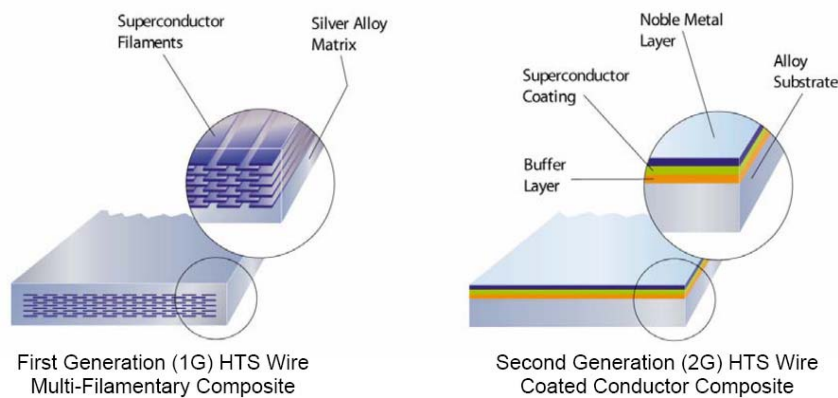


Figure I.2 Illustrations of HTS wire structures – the 1st generation vs. the 2nd generation HTS wires
(From American Superconductor Corp. homepage; <http://www.amsuper.com>)

In order to manufacture YBCO in useful conductor with acceptable J_c values in long length, it is necessary to produce YBCO thin films with minimizing the number of high

angle grain boundary which detrimentally affects J_c . This has been done most successfully in multi-layered tape form, called coated conductors or the 2nd generation HTS wires (Figure I.2), made by epitaxial-growth of YBCO on textured oxide-buffered metal tapes. The typical structure is illustrated in Figure I.3. The number of high angle grain boundaries in YBCO is reduced through biaxial alignments of grains of either metal tapes or oxide buffer layers. Texturing of metal tapes is achieved by a deformation method [9], while that of oxide buffer layers is achieved under an ion beam assisted [10,11]. Details of the techniques will be described in section I.3.

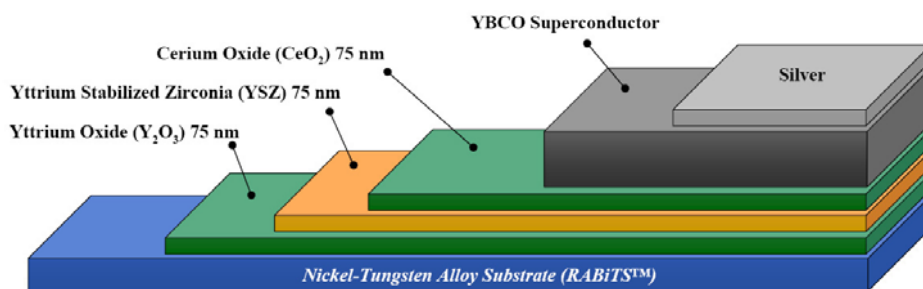


Figure I.3 A schematic illustration of typical coated conductors.
(From American Superconductor Corp. homepage; <http://www.amsuper.com>)

I.1.3 Performance requirements of coated conductors

Practically, coated conductors can be characterized by three important parameters – critical current density J_c , critical current per unit width I_c^* , and irreversibility field H_{irr} (or H^*). High J_c of 4-7 MA/cm² has been routinely achieved by many deposition techniques for thin YBCO films (thickness of a few hundreds nanometers). However, the high J_c at thin films yields only $I_c^* \sim 200 - 300$ A/cm-width. Thus, the main challenge is to achieve sufficiently thick films with high J_c to reach over 500-1000 A/cm-width of I_c^* at 77 K. The

H_{irr} defines the practical limitation of applied magnetic field of superconductors, where critical current and flux pinning is no longer effective (no effective J_c). Thus, obtaining high H_{irr} is very crucial task for the high field applications. In-field J_c must attain 10^4 - 10^5 A/cm² in fields of 0.1-10 T at temperatures of 20 – 77 K [2] for applications. In addition, length in the order of a km is required.

I.2 Scientific challenges of coated conductors

While progress in the development of YBCO coated conductor is being made extensively, some critical issues are not fully understood scientifically yet. In this section, the critical scientific challenges in YBCO coated conductor research will be discussed, including the weak coupling across grain boundaries, J_c reduction with increasing film thickness, and flux pinning issue.

I.2.1 Weak superconducting coupling across grain boundaries

The grain boundaries (GBs) in YBCO are structurally and compositionally heterogeneous on a scale of 1 – 5 nm, comparable to the coherence length ξ of YBCO at 77K. (The coherent length ξ is a measure of the distance within which the superconducting electron concentration cannot change drastically in a spatially-varying magnetic field, simply being interpreted as the pairing length of the superconducting electron pairs.) Low angle GBs consists of grain boundary dislocation cores and conductive, grain-like channels [12], as shown in Figure I.4(a). The atomic disruptions at the dislocation cores and the

strain fields surrounding the cores depress the superconducting order parameter [12,13] and disrupt the supercurrent over a region of 1-2 nm near the grain boundary cores. Wider depleted regions have been seen for higher misorientations, resulting weaker coupling across the GBs [14].

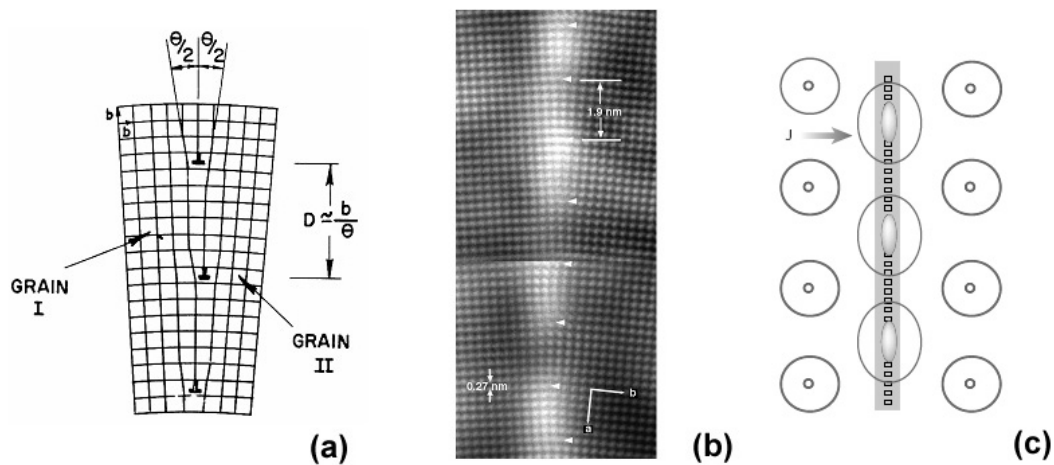


Figure I.4 (a) Low angle grain boundary. Dislocation cores are highly distorted and strained regions and likely to be insulating. (b) HRTEM image of 8° [001] tilt GB in BSCCO [2] (c) A schematic illustration of the vortices structure at GB. Abrikosov vortices are indicated within the grains, but their cores become elongated at GB (Abrikosov-Josephson vortices), owing to the reduced J_c of the GB.

The GBs reduce critical current density J_c . Initial experiment by Dimos *et al.* [15] established that the J_c across grain boundaries was strongly dependent on the misorientation angle. Now it has been well established that J_c of GBs decreases exponentially with increasing the misorientation angle beyond a given critical angle θ_c from [100] tilt bicrystal experiments [16] and micro-bridge experiments on coated conductors [17]. The critical

angle θ_c occurs at about 3-4° [16-19] at self-field and 77 K, when J_c of the GBs is below that of the grain. Figure I.5 shows the exponential J_c dependence on GB misorientation angle at 4.2 K. It is therefore very important to reduce GB misorientation angles in the conductor development in order to maximize current carrying capability – J_c and I_c .

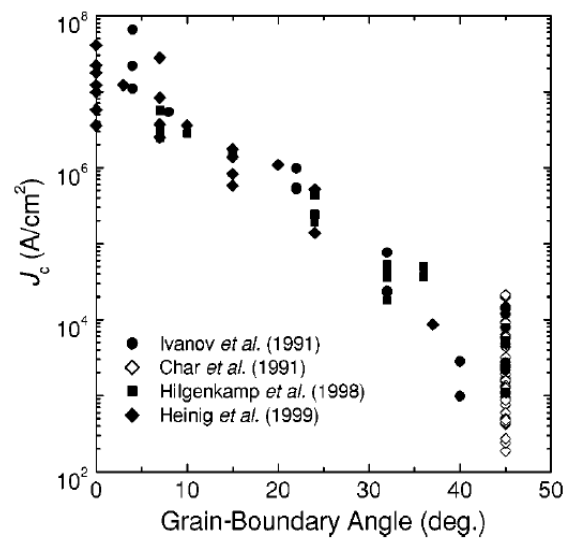


Figure I.5 Transport J_c of [001]-tilt grain boundaries in YBCO films as a function of tilt angle at 4.2 K [20] .

I.2.2 Thickness dependence of the critical current density

The obvious route to high I_c is to increase the thickness of the YBCO layer. However, significant reductions of J_c with increasing film thickness have been generally observed [21-25] as shown in Figure I.6. While this dependence is predicted from intrinsic effect of two dimensional (2D) collective pinning [26], it is believed to be largely material dependent as well. However, whether this reduction is due to fundamental vortex physics or thickness-dependent material microstructure is not yet fully clear.

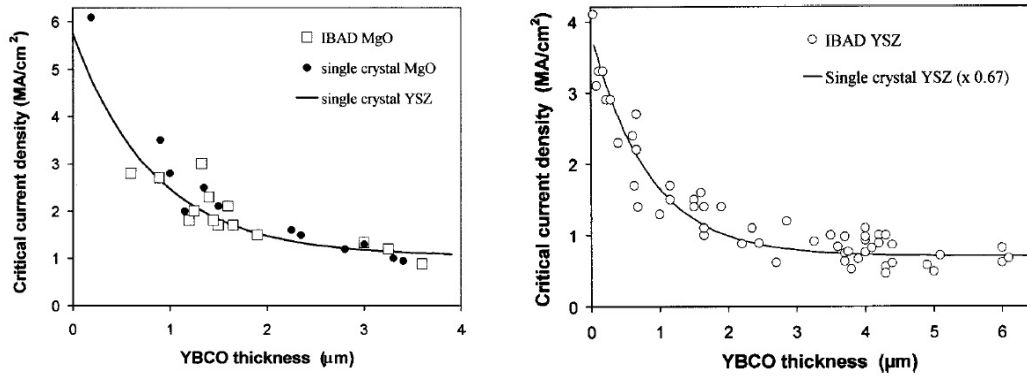


Figure I.6 J_c dependence of YBCO films of varying thickness. In situ PLD YBCO films grown on IBAD-MgO/single crystals and IBAD-YSZ of Los Alamos National Lab [24].

I.2.3 Flux pinning issue

Within a single grain, the J_c is controlled by the flux pinning properties of the materials. Flux pinning is the mechanism where by the dissipative movement of vortex under the Lorentz force is prevented by flux pinning centers. The flux pinning centers can be various defects such as point (cation disorder, oxygen vacancies), line (dislocations), planar (antiphase boundaries, stacking faults, twin boundaries), and volume (precipitates, macroscopic non-uniformity) defects. Good flux pinning is essential for significant transport current density to be sustained in the superconducting state, and to maximize J_c and H_{irr} . Studies from LTS materials have established the optimum size and density of the pinning defects [27]. The size is set by the coherence length ξ , and the optimal density of defects is determined by the vortex spacing, given approximately by $(\phi_0/B)^{1/2}$, where B is the applied field. The pinning defects are largely unknown for HTS materials, because the coherence length is so small ($\xi_{ab}(\text{YBCO}) \sim 3.5 \text{ nm}$ at 77K) that even atomic-size defects

can pin vortex. This extreme sensitivity of HTS to nanoscale defect structure is vitally important in determining the current-carrying capability of conductors.

I.3 Substrates and Buffer Layers in Coated Conductors

The two most successful techniques for developing biaxial texture in coated conductors are Ion Beam Assisted Deposition (IBAD) [10,11] and Rolling Assisted Biaxially Textured Substrate (RABiTS) [9]. In the IBAD technique, the texture is introduced in the oxide buffer layers, usually yttria-stabilized zirconia (YSZ) or MgO. The deposition occurs under an ion beam assist, giving rise to biaxial texture. This process allows for the use of strong, non-magnetic substrates and can result in a very high degree of texture for MgO and YSZ. Very high degree of texture (FWMH $\sim 2^\circ$) has been achieved by this technique, though it is quite expensive and slow process.

In RABiTS, texture is introduced into the metal substrate, generally Ni-W alloy, by mechanical deformation and recrystallization. This can be readily done continuously in long lengths, but the degree of texture (4 - 6° FWHM) is not yet as good as can be obtained with IBAD. Also, the grain size of the metal template is larger with the RABiTS technique (50 μm vs. 1 μm of IBAD). Modeling has shown that there is a positive correlation between increased critical current density and decreasing grain size at fixed tape width [28]. Despite this, the RABiTS technique can produce high J_c values exceeding $\sim 3 \text{ MA/cm}^2$, and presently appears to be the principal commercial low cost technique [29]. The usual buffer layers for RABiTS consist of seed, diffusion barrier, cap layers suitable for

epitaxial YBCO growth. Buffer layer structures can vary, but a very common architecture is $\text{Y}_2\text{O}_3/\text{YSZ}/\text{CeO}_2/\text{YBCO}$, respectively (see Figure I.3).

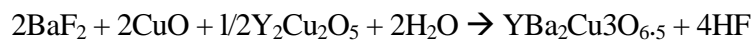
I.4 Superconducting Layer in Coated Conductors

There are various techniques for deposition of the YBCO layer on the buffered substrate, including *in situ* pulsed laser deposition (PLD), metal organic chemical vapor deposition (MOCVD), liquid phase epitaxy (LPE), and sputtering, and *ex situ* conversion of BaF_2 -based precursor deposited either by electron-beam evaporation (e-beam BaF_2 process) and metal-organic deposition (MOD process). The thickness of the YBCO may vary from a few hundred nanometers to several microns.

I.4.1 *Ex situ* MOD process

One attractive combination of techniques involves use of a RABiTS template for the formation of the textured substrate along with the *ex situ* metal organic deposition (MOD) of the YBCO layer [30,31]. The MOD process is based on the formation of the YBCO layer from a solution-based precursor coated on the surface of the buffered substrate. The combination of MOD/RABiTS technologies was adopted by American Superconductor Corporation (AMSC) and is particularly attractive based on its low projected price/performance ratio. At present, the coated conductor produced by the MOD process has the highest performance and is perhaps the strongest candidate for commercialization due to its low cost and high scalability.

In MOD process, YBCO precursors are deposited on the buffered substrates by an industrial web-coating process using a trifluoroacetate (TFA)-based materials. The MOD film is pyrolyzed at 400 °C in a humid, oxygen atmosphere to a precursor film with a nominal composition of BaF₂, CuO and Y₂O₃, and then converted to epitaxial YBCO at 700 – 800 °C in an O₂/H₂O/N₂ environment. After the reaction, the composition of the film is oxygen deficient YBa₂Cu₃O_{6.5}, being needed to be annealed in the oxygen environment. The overall reaction that occurs can be represented by the following equation.



I.4.2 *In situ* Pulsed Laser Deposition process

The PLD technique is one of the most popular and effective techniques used in the present days for the deposition of high quality oxide films in scientific research. This PLD method involves congruent evaporation of a target in a vacuum chamber by means of focused high-energy laser pulses. Because of the vacuum environment, the laser-induced plasma is more or less adiabatically ablated. Such a plasma plume contains positive and negative ions, neutral atoms, molecules, atoms, and other species. These particles move preferentially normal to the target surface and deposit on the heated substrate. The method also allows one to oxygenate the film *in situ*. Some of the films investigated throughout this work are made by PLD. In addition, more details of PLD technique will be described in Chapter II.

I.5. Motivation and outline

I.5.1 Motivation

The aim of the current research is to elucidate a few critical scientific issues of YBCO coated conductors, including *grain boundary issue* and *thickness dependence of J_c* by means of extensive transport critical current density measurements. First of all, the study on grain boundary issue covers (i) a broad understanding of grain boundary network effects of real coated conductors made by RABiTS techniques over wide range of field and temperature, and (ii) the improvement of low angle grain boundary transparency by Ca- or other cation doping. The objective is to develop a unified description of the low angle grain boundary found in coated conductors along with the provided modeling and electron microscopy. Secondly, the thickness dependence of J_c of YBCO films made by various techniques are studied by depth profiling of normal state properties and superconducting characteristics using ion milling. The purpose is to get a much better understanding of the relative contributions of physics- and materials-related effects in different types of YBCO films based on their microstructure.

My principal tool has been on extensive transport critical current density measurements over wide field H and temperature T for various bridge widths, and various YBCO thicknesses. In addition, the growth of YBCO and cation-doped YBCO films on bicrystal SrTiO_3 substrates by pulsed laser deposition technique has been used for investigation of cation doping influence on low angle grain boundaries.

I.5.2 Structure of the thesis

In this chapter I, background on YBCO coated conductors has been described, including the architecture of typical YBCO coated conductors, the requirements for commercialization, and a few critical scientific issues, including the motivation of current work.

Chapter II discusses the experimental techniques, which has been used over the current research. Electromagnetic characterization technique, which includes extended V-I characteristics and $J_c(H)$ dependencies, will be described in detail, followed by the discussion on analysis of the results. PLD technique, which used for cation-doping effect on low angle grain boundary, is described, including details of our PLD system setup. Other techniques, including electron backscattering diffraction, magneto-optic imaging, x-ray diffraction, will be explained briefly as well.

Chapter III reports the study on influence of grain boundary network on the critical current density of *real* coated conductors. Detailed study on J_c and V-I characteristics over a broad range of magnetic fields and temperatures in a series of three 1 μm thick $\text{YBa}_2\text{Cu}_3\text{O}_{7-x}$ samples with variable textures, including a single crystalline film and two coated conductors on RABiTS substrate made by metal-organic deposition (MOD) process (American Superconductor Corporation) is described. In addition, the influence of the number of grains within the bridge width is investigated by successively narrowing the bridge on the better-textured sample. The results delineate several ways in which the grain boundary network properties including its misorientation distribution and the grain density within width can control J_c .

In Chapter VI, the improvement of low angle grain boundary transparency by means of Ca-doping or other cation doping will be extensively discussed. The low angle GBs with different Ca content x ($Y_{1-x}Ca_xBa_2Cu_3O_{7-\delta}$) is tested to verify the influence of the density of carriers at GB due to the Ca doping level. In addition, Ca-doping effect on $YbBa_2Cu_3O_{7-x}$ is studied to further investigate the strain effect around the GB cores. Finally, Nd^{3+} ion was proposed as a possible cation dopant for GB improvement, and tested.

Chapter V reports the study on thickness dependence of J_c on YBCO samples with different microstructure made by various techniques including MOD and PLD. Depth profiling of normal state properties and superconducting properties was measured and analyzed based on its microstructure. It was found that the thickness dependence of J_c on YBCO can be very much dependent of its microstructure.

Lastly, chapter VI summarizes the results, and emphasizes the significance of the current research.

References

- [1] J. G. Bednorz & K. A. Muller, *Z Phys B Con Mat* **64**, 189 (1986).
- [2] D. Larbalestier, A. Gurevich, D. M. Feldmann & A. Polyanskii, *Nature* **414**, 368 (2001).
- [3] K. Hayashi, T. Hikata, T. Kaneko, M. Ueyama, A. Mikumo, N. Ayai, S. Kobayashi, H. Takei & K. Sato, *IEEE T Appl Supercon* **11**, 3281 (2001).
- [4] N. J. Kelley, C. Wakefield, M. Nassi, P. Corsaro, S. Spreafico, D. W. Von Dollen & J. Jipping, *IEEE T Appl Supercon* **11**, 2461 (2001).
- [5] M. K. Wu, J. R. Ashburn, C. J. Torng, P. H. Hor, R. L. Meng, L. Gao, Z. J. Huang, Y. Q. Wang & C. W. Chu, *Phys Rev Lett* **58**, 908 (1987).
- [6] H. Maeda, Y. Tanaka, M. Fukutomi & T. Asano, *Jpn J Appl Phys 2* **27**, L209 (1988).
- [7] A. Schilling, M. Cantoni, J. D. Guo & H. R. Ott, *Nature* **363**, 56 (1993).
- [8] Z. Z. Sheng, W. Kiehl, J. Bennett, A. Elali, D. Marsh, G. D. Mooney, F. Arammash, J. Smith, D. Viar & A. M. Hermann, *Appl Phys Lett* **52**, 1738 (1988).
- [9] A. Goyal, D. P. Norton, J. D. Budai, M. Paranthaman, E. D. Specht, D. M. Kroeger, D. K. Christen, Q. He, B. Saffian, F. A. List, D. F. Lee, P. M. Martin, C. E. Klabunde, E. Hartfield & V. K. Sikka, *Appl Phys Lett* **69**, 1795 (1996).
- [10] Y. Iijima, N. Tanabe, Y. Ikeno & O. Kohno, *Physica C* **185**, 1959 (1991).
- [11] X. D. Wu, S. R. Foltyn, P. N. Arendt, W. R. Blumenthal, I. H. Campbell, J. D. Cotton, J. Y. Coulter, W. L. Hults, M. P. Maley, H. F. Safar & J. L. Smith, *Appl Phys Lett* **67**, 2397 (1995).
- [12] M. F. Chisholm & S. J. Pennycook, *Nature* **351**, 47 (1991).
- [13] N. D. Browning, J. P. Buban, P. D. Nellist, D. P. Norton, M. F. Chisholm & S. J. Pennycook, *Physica C* **294**, 183 (1998).
- [14] I. F. Tsu, S. E. Babcock & D. L. Kaiser, *J Mater Res* **11**, 1383 (1996).
- [15] D. Dimos, P. Chaudhari & J. Mannhart, *Phys Rev B* **41**, 4038 (1990).

- [16] D. T. Verebelyi, D. K. Christen, R. Feenstra, C. Cantoni, A. Goyal, D. F. Lee, M. Paranthaman, P. N. Arendt, R. F. DePaula, J. R. Groves & C. Prouteau, *Appl Phys Lett* **76**, 1755 (2000).
- [17] D. M. Feldmann, D. C. Larbalestier, D. T. Verebelyi, W. Zhang, Q. Li, G. N. Riley, R. Feenstra, A. Goyal, D. F. Lee, M. Paranthaman, D. M. Kroeger & D. K. Christen, *Appl Phys Lett* **79**, 3998 (2001).
- [18] N. F. Heinig, R. D. Redwing, J. E. Nordman & D. C. Larbalestier, *Phys Rev B* **60**, 1409 (1999).
- [19] D. M. Feldmann, J. L. Reeves, A. A. Polyanskii, A. Goyal, R. Feenstra, D. F. Lee, M. Paranthaman, D. M. Kroeger, D. K. Christen, S. E. Babcock & D. C. Larbalestier, *IEEE T Appl Supercon* **11**, 3772 (2001).
- [20] H. Hilgenkamp & J. Mannhart, *Rev Mod Phys* **74**, 485 (2002).
- [21] X. D. Wu, S. R. Foltyn, P. Arendt, J. Townsend, I. H. Campbell, P. Tiwari, Q. X. Jia, J. O. Willis, M. P. Maley, J. Y. Coulter & D. E. Peterson, *IEEE Trans Appl Supercon* **5**, 2001 (1995).
- [22] S. R. Foltyn, P. Tiwari, R. C. Dye, M. Q. Le & X. D. Wu, *Appl Phys Lett* **63**, 1848 (1993).
- [23] S. R. Foltyn, Q. X. Jia, P. N. Arendt, L. Kinder, Y. Fan & J. F. Smith, *Appl Phys Lett* **75**, 3692 (1999).
- [24] S. R. Foltyn, P. N. Arendt, Q. X. Jia, H. Wang, J. L. MacManus-Driscoll, S. Kreiskott, R. F. DePaula, L. Stan, J. R. Groves & P. C. Dowden, *Appl Phys Lett* **82**, 4519 (2003).
- [25] J. R. Groves, P. N. Arendt, S. R. Foltyn, Q. X. Jia, T. G. Holesinger, H. Kung, E. J. Peterson, R. F. DePaula, P. C. Dowden, L. Stan & L. A. Emmert, *J Mater Res* **16**, 2175 (2001).
- [26] A. Gurevich, Presentation at http://www.energetics.com/meetings/supercon04/pdfs/presentations/f_uw_coated_conductor_peer_rev_04final.pdf
- [27] C. Meingast, P. J. Lee & D. C. Larbalestier, *J Appl Phys* **66**, 5962 (1989).
- [28] N. A. Rutter, B. A. Glowacki & J. E. Evetts, *Supercond Sci Tech* **13**, L25 (2000).

- [29] X. Li, M. W. Rupich, W. Zhang, N. Nguyen, T. Kodenkandath, U. Schoop, D. T. Verebelyi, C. Thieme, M. Jowett, P. N. Arendt, S. R. Foltyn, T. G. Holesinger, T. Aytug, D. K. Christen & M. P. Paranthaman, *Physica C* **390**, 249 (2003).
- [30] P. C. McIntyre, M. J. Cima & A. Roshko, *J Appl Phys* **77**, 5263 (1995).
- [31] A. Gupta, R. Jagannathan, E. I. Cooper, E. A. Giess, J. I. Landman & B. W. Hussey, *Appl Phys Lett* **52**, 2077 (1988).

Chapter II. Experiment

II.1 Electromagnetic characterization

The current research have mainly involved electromagnetic characterization of various YBCO coated conductor samples from many sources in both normal and superconducting state, which includes resistance (or resistivity), superconducting critical temperature T_c , critical current density J_c , and irreversibility field H_{irr} . In this section, details of the electromagnetic characterization technique are given.

II.1.1 Electromagnetic characterization

Samples were prepared as a small piece, size of $5 \times 10 \text{ mm}^2$ rectangles with bare YBCO without Ag cap layers. Four gold electrical contacts (two are for current and the other two for voltage) were deposited by DC magnetron sputtering using a shadow mask. It is very important to have as low a contact resistance as possible for successful measurements, however, we found no problem with the contact resistance after a short period Ar ion milling before the deposition of contacts. Then, the majority of films were patterned using Nd-YAG laser ablation of YBCO layers, which is relatively quick and easy compared to photolithography that was used occasionally for small bridge width ($< 40 \text{ }\mu\text{m}$). Bridges are defined typical size of $50 - 300 \text{ }\mu\text{m}$ wide by $500 - 1000 \text{ }\mu\text{m}$ long using an automated x-y stage developed by N. Nelson, a former graduate student in our group.

Measurements were made by DC transport measurement using standard four-point probe method, while current reversal algorithm being used to remove thermal voltage effect.

Most of the measurements setups described below were made by Dr. D. Matthew Feldmann, a former scientist in our group. The sample was placed on the Cu block at the end of measuring probe with LakeShore Cernox Resistance Temperature Sensor close. Temperature was monitored and controlled usually within ± 0.001 K by a LakeShore 340 temperature controller and heater wires on the Cu block. The measuring probe used gold plated Pogo™ pins to make contact with the sample with spring force, and bare Cu-to-Cu connections are retained all the way to the pre-amplifiers (Keithley 1801) to minimize the voltage noise down to the nano-voltage level. The pre-amplifiers permit nano-volt sensitivity on voltage measurement. Small transport currents less than 100 mA were applied using a Keithley 2420 3A source-meter. However, transport current over 100 mA was applied as a short pulse (50 ms) using a KEPCO bipolar operational power supply/amplifier to prevent possible excessive heating. This allowed currents up to 10 A without excessive heating. The resistance - temperature $R(T)$ curves were measured using an excitation current of 1 - 10 μ A as the sample cooling down. The voltage - current $V-I$ curves were measured by sweeping the current and measuring the voltage at a certain magnetic field. LabVIEW programs were written by D. Matthew Feldmann for automated data collection, which also allowed for remote control and observation. Measurements were performed in an OXFORD Instruments variable temperature inset (VTI) installed in a superconducting 14 T magnet. Temperature of VTI space is controlled roughly by the flow rate of He gas, independent of sample space. The field measurements were performed with field applied perpendicular to film surface in the OXFORD magnet system.

Recently it was suggested and demonstrated that angular J_c measurement is a very useful tool for studying the pinning mechanism of YBCO films [1,2], especially for those related with correlated (directional) pinning. Accordingly, angular J_c measurement $J_c(\phi)$ capability was designed and built by Zhijun Chen, a graduate student in our group. The rotation of the sample is controlled by a high resolution stepper motor with variable step sizes from 0.5° up to 1.2° per second. The rotation is configured such that the applied magnetic field is always perpendicular to the current bridge. The sample temperature is monitored and controlled by a Lakeshore 331S temperature controller with an accuracy of better than ± 0.005 K with a 10 W heater. Sample preparation steps are the same, however, it uses soldering wire to the gold contact because of lack of space to accommodate Pogo pins. The rotating measuring probe is placed in a 9 T QuantumDesignTM Physical Property Measurement System (PPMS). The automated program for this system was coded by Z. Chen as well.

II.1.2 Analysis of electromagnetic characteristics

Using the described transport measurement setup, a few major data sets are obtained and analyzed; (i) resistance curve $R(T)$, (ii) voltage-current characteristics V-I curves, (iii) critical current density as a function of magnetic field, $J_c(H)$, and (iv) J_c as a function of angle between sample plane and magnetic field. First three data sets are usually obtained in the OXFORD magnet system, while the angular J_c measurement $J_c(\phi)$ is obtained in PPMS.

R(T) curve provides superconducting critical temperature T_c , width of T_c transition ΔT_c , room temperature resistivity ρ_{300K} , and oxygenation state of the sample. The T_c was defined as the onset of zero resistance ($\sim 1\%$ of normal state resistance) and the ΔT_c can be defined the full-width half-maximum (FWHM) of derivative of R(T) near T_c . The ρ_{300K} can be calculated from the geometry of the bridge ($\rho_{300K} = R_{300K} \cdot w \cdot t / l$, where R_{300K} is resistance at 300 K, w is width, t is thickness, and l is length of the bridge). The typical ρ_{300K} values of high-quality, well oxygenated, and dense YBCO films is 200 – 250 $\mu\Omega\text{cm}$ [3-5]. An effective medium theory (EMT) [6] permits to calculate the fraction of current-blocking defects in the YBCO matrix, if the ρ_{300K} value is higher than the typical value. The curvature of the R(T) plot indicates the oxygenation state of the YBCO layer [7] as well. An upward curvature indicates a slightly oxygen over-doped YBCO (see Figure II.1), while a downward curvature suggests a oxygen under-doped YBCO.

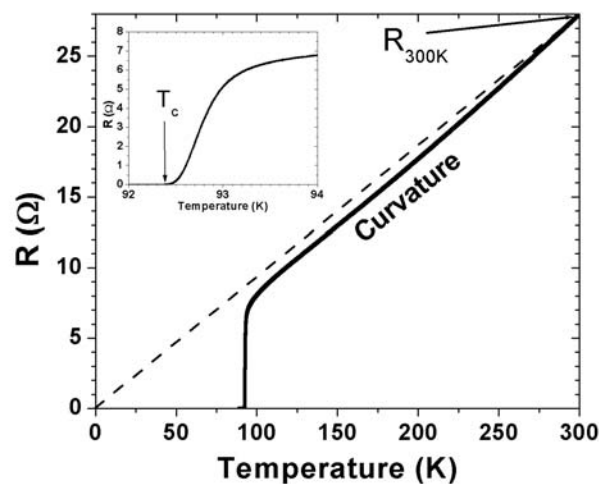


Figure II.1 R(T) curves of a typical MOD sample. The resistivity ρ can be calculated based on the resistance R value and geometry of the bridge; $\rho = R \cdot w \cdot t / l$. Upward curvature indicates a slight oxygen over-doped nature of the MOD YBCO sample.

Voltage-current (V-I) curves (Figure II.2(a)) represent the electrical responses in the superconducting state. V-I curves were often normalized to electrical field - critical current (E - J) curves. I_c and J_c values were determined using an electric field criterion of $1 \mu\text{V}/\text{cm}$. Often, irreversibility field H_{irr} is defined in the V-I curves by the curvature change in $\log(E) - \log(J)$ curves, which indicates the vortex glass-liquid transition [8]. However, more convenient way to define the irreversibility field H_{irr} in $J_c(H)$ plot is where J_c becomes very low, $100 \text{ A}/\text{cm}^2$. Usually there is clear distinction between V-I curve shape between intra-grain and inter-grain, which will be described in Chapter III in detail.

$J_c(H)$ is the most widely-used superconductor characteristics and a fundamental tool to study superconducting properties, which is derived from the V-I curves as a function of fields. The pinning properties can be well represented by plotting bulk flux pinning force curve, $F_p(H) = J_c(H) \cdot H \text{ (N/m}^3\text{)}$. Shape of $F_p(H)$ is a characteristic of dominant pinning type. Larger maximum pinning force at larger field is desirable for high field applications. Examples of E-J curves, $J_c(H)$, and $F_p(H)$ for a sample are shown in Figure II.2.

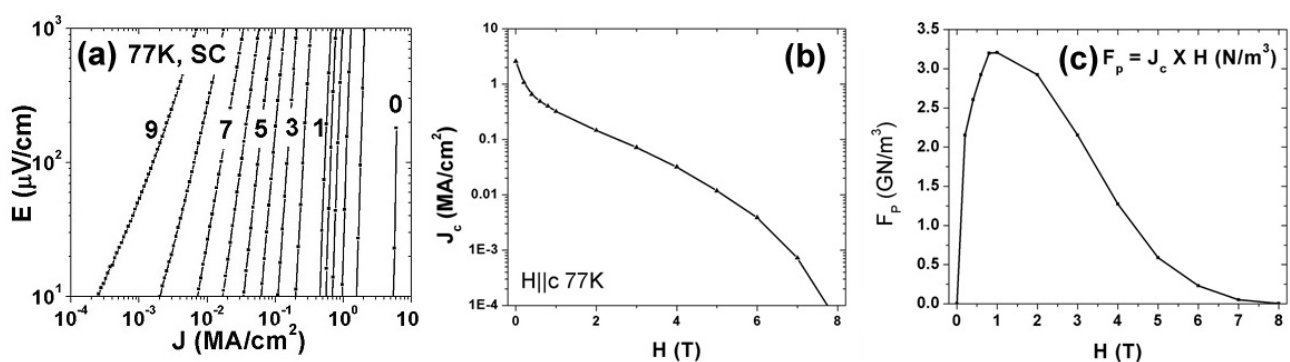


Figure II.2 Examples of (a) E-J characteristics, (b) $J_c(H)$, and (c) $F_p(H)$.

Angular J_c measurement $J_c(\phi)$ is recently proposed as a tool for studying the pinning nature of YBCO films [1,2]. YBCO typically shows anisotropy of $\sim 5-7$, which is also represented J_c ratio as well; typically $J_c(H\parallel c)$ is much smaller than $J_c(H\parallel ab)$, while the ratio is dependent of process and microstructure of YBCO. However, it has been found that J_c peaks exist due to correlated pinning effect of directional defects in the YBCO – for example, c-axis peaks exist due to dislocations, twin boundaries, and anti-phase boundaries and ab-axis peaks are present due to correlated pinning defects, such as intergrowth, and stacking faults (shown in Figure II.3).

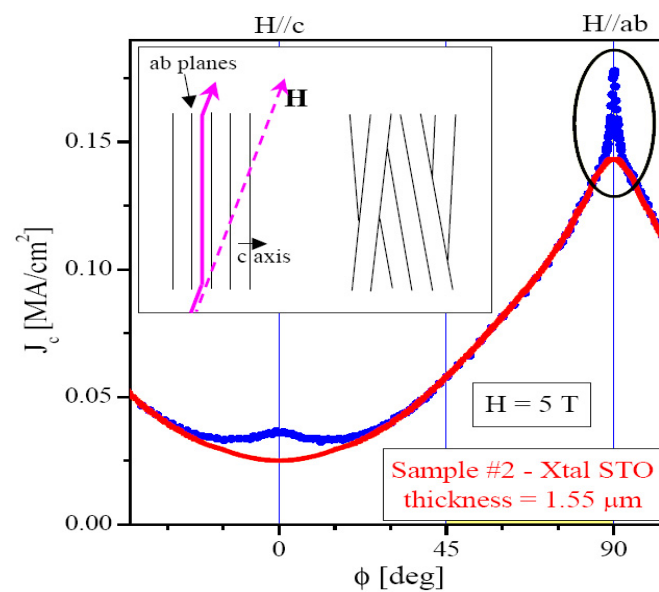


Figure II.3 Examples of angular $J_c(\phi)$ measurement. Red curve shows J_c anisotropy due to mass aniotropy of YBCO. However, the measured data (blue curve) shows correlated pinning peaks at $H\parallel c$ and $H\parallel ab$ [9]

II.2 YBCO thin film deposition by pulsed laser deposition

II.2.1 Brief introduction to pulsed laser deposition

After Venkatesan and co-workers successfully demonstrated *in situ* preparation of YBCO thin films with high critical temperature T_c and high critical current density J_c by the pulsed laser deposition (PLD) technique during late 1987 and early 1988 [10,11], PLD has been widely used to prepare epitaxial thin films of any oxide material, including HTS materials. PLD is becoming one of the most important techniques to engineer thin film growth in research laboratories, because it has a number of advantages over most other deposition processes. The energy at the target can be controlled independently of the process pressure and gas mixture, and stoichiometric deposition can easily be conducted. High energy densities, high rates and high process flexibility are characteristic features of the process. Moreover, the method is a relatively fast and cost effective way to produce high quality films, which also allows oxygenation of the films *in situ*. However, traditionally PLD is limited to small areas (typically 1 cm^2) and the pulsed deposition process has a large impact on the morphology of the sample. It often forms droplets of submicron size are formed on the surface of the deposited film.

The essential process of PLD consists of melting and evaporating of target materials with the pulsed laser beam. Film deposition by PLD is carried out by irradiation of a single

or multiple targets by a focused excimer laser beam. Excimer laser ($\lambda = 308 \text{ nm}, 248 \text{ nm}$) has a energy density $1\text{-}3 \text{ J/cm}^2$ per shot and frequency of several hertz typically. A pulsed laser beam with a typical duration time of $20 \sim 30 \text{ nsec}$ impinges on the target surface. During ablation a luminous cloud (plume) is formed along the normal of the target by evaporating a few hundreds angstrom of materials from the target. The photons of the laser beam with high energy interact only with the free electrons of the target material, and the laser-induced plasma is more or less adiabatically ablated due to the vacuum environment. Such a plasma plume contains positive and negative ions, neutral atoms, molecules, atoms, and other species. These particles move preferentially normal to the target surface and deposit on the substrate. The hot substrate, often rotating, is placed at a carefully chosen position with respect to the plume characteristics. Nevertheless, a great deal of complex chemistry and physics goes on in the plume. The main problems with the technique are that it depends on ablation from a point source, so measures must be taken to enforce film thickness uniformity. The laser power must be scaled up if enough material is to be ablated to give large area coverage at useful rates. Modern lasers can achieve these power levels.

II.2.2 PLD system setup

A new PLD system was set up with a multi-target capability with a automated Neocera 6 multi-target carousel. The laser source is Lambda Physik LPX® 210i, KrF excimer laser with dielectric rare mirror for 248 nm and uncoated MgF_2 window for all

wavelengths. The laser has a wavelength of 248 nm, which is very effective for congruent ablation within 25 nm range. It can be operated up to 60 Hz. Tested pulse energy is 894 mJ and the energy density is varied by either laser output or beam size on the target. Laser beam dimensions are $5-12 \times 23 \text{ mm}^2$ and can be adjusted by means of demagnification. The laser optic is set up with a reflective coated mirror and a planoconcave quartz lens. A mask (aperture) can be used across the beam so non-uniform edges of the beam are cut off. Pulsed duration is 25 ns of FWHM and pulse-to-pulse stability is within $\pm 3 \%$ in our Laser system.

Vacuum chamber provides base pressure $< 10^{-6}$ torr with a turbo molecular pump. The oxygen pressure of the chamber is controlled by a butterfly valve, a valve controller, and the gas flow mass controllers. The 2 inch conductive heater is attached in the vacuum chamber, which has maximum temperature 950 °C with ± 1 °C stability with type K thermocouple and temperature controller. The multi-target capability up to six targets allows producing many different compositions in a single deposition run to arrive at optimum composition having the desired material properties. Heat/contamination shield is placed in front of target. In addition, target change and rotation can be controlled automatically by program provided by Neocera.

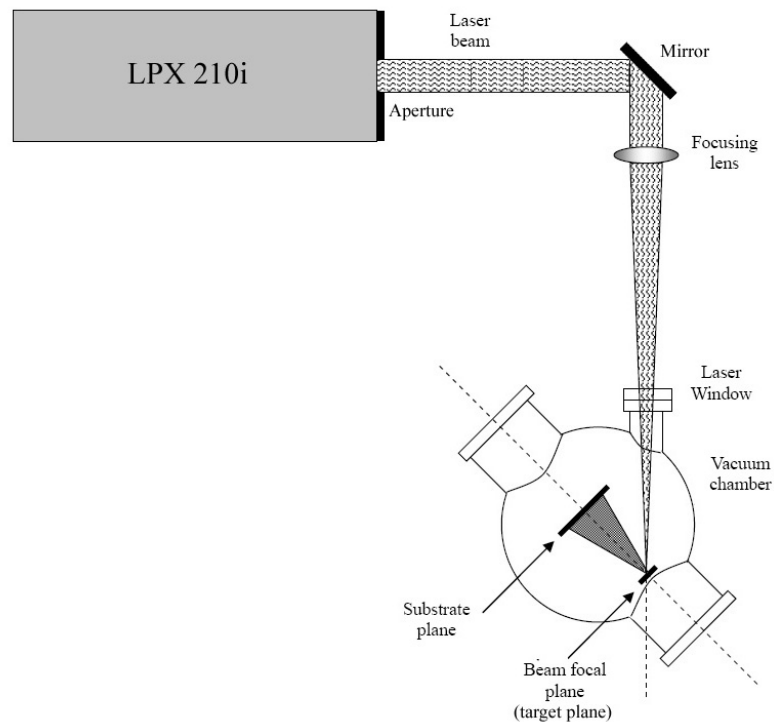


Figure II.4 Schematic diagram of PLD system. Laser beam is cut off by aperture to obtain the uniformity, and focused by planoconcave quartz lens at the target plane. The focused beam produce plasma plume, which reaches at heated substrate.

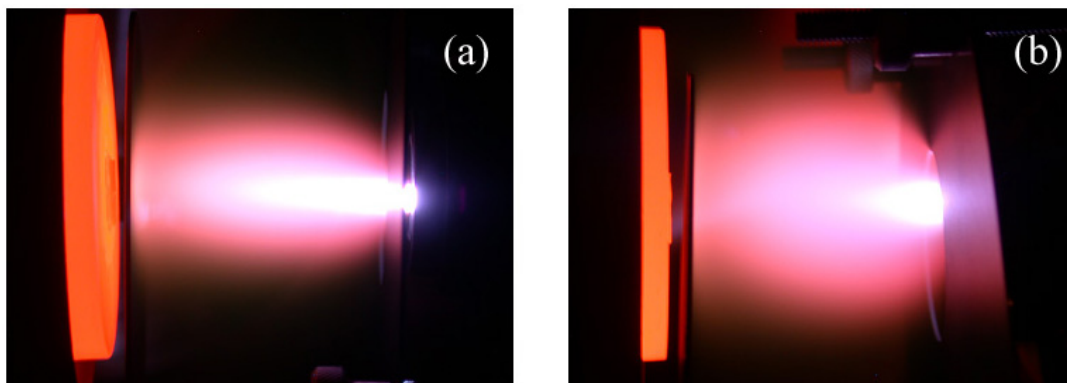


Figure II.5 Pictures of plumes from YBCO targets (1 Hz, 1 sec exposure); (a) top-view and (b) side-view. The rectangular beam shape produces the beam shape elongated to one direction.

II.3 Other techniques

Various characterization techniques have been used throughout this work. Brief descriptions of these techniques are given in this section, including electron backscatter diffraction (EBSD), magneto-optic imaging (MOI), and X-ray diffraction (XRD).

II.3.1 Electron backscatter diffraction, EBSD

Electron backscatter diffraction (EBSD) is a common technique used in the characterization of polycrystalline materials for determining grain/crystal orientations [12,13]. EBSD patterns are generated by backscattered electrons in the SEM by electron illuminating a 70° tilt sample and captured by the phosphor screen. These EBSD patterns, called *Kikuchi* patterns as well, are a reciprocal projection of the lattice plane geometry in a crystal. Cameras may vary from real-time imaging to long-term exposure systems depending on the application and required signal-to-noise ratio. Orientation mapping using EBSD is obtained by an array of crystal information determined by EBSD patterns. Using the software, EBSD pattern is collected and automatically indexed and the crystallographic orientation calculated. In turn, a orientation map of the sample can be generated. The technique is used to determine local misorientation matrix of the bridges of the measured samples in Chapter III.

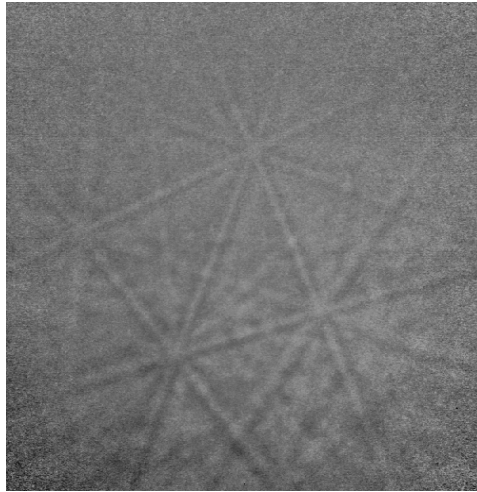


Figure II.6 Example of EBSD pattern (Kikuchi pattern) of SrTiO₃.

II.3.2 Magneto-optic Imaging (MOI)

The magneto-optical imaging technique provides a spatial map of the perpendicular component of the magnetic field above the surface of a material that can be compared directly with a conventional light microscope image of the same region for structure-property relationship determinations. The technique is an old one, and was first applied to superconductivity in 1957 by P.B. Alers [14]. This visualizes magnetic flux and has been an invaluable tool in identifying inhomogeneities in many types of superconducting samples. Regions of higher magnetic field strength image more brightly in this image. It is quick and non-destructive. The Magneto-Optical Imaging Facility maintains a 0 - 0.12 T magneto-optical microscope with a spatial resolution of ~5 microns, a cold stage (< 10 K to room temperature), and integrated image analysis capabilities. The magneto-optic measurement was carried with help of A. Polyanskii, a senior scientist in our group.

II.3.3 X-ray Diffraction (XRD)

X-ray diffraction has been used often for the structural study of epitaxial thin YBCO films, as it allows probing the crystal structure of epitaxial films non-destructively. For thin film sample characterization, a 4-circle x-ray diffractometer can be used. By using the 4-circles of the diffractometer, the sample can be oriented at different angles to the incident beam so that different crystallographic planes contribute to diffraction [15]. Using a 4-circle diffractometer, the in-plane and out-of-plane texture can be determined, which are very important parameters in the grain boundary issue.

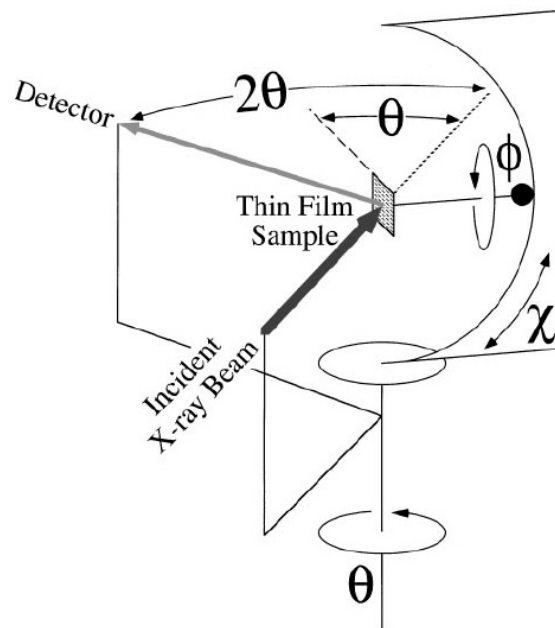


Figure II.7 A schematic diagram of a 4-circle x-ray diffractometer used to determine the texture of coated conductor samples (Figure from Fig.2 of [15]).

Out-of-plane texture is measured by rocking curve measurements (θ scan at a fixed 2θ angle), usually of YBCO (005) peak. In-plane texture measurement is done by the off-axis ϕ -scan at fixed θ - 2θ angle) of YBCO (103) reflections. Often, a texture measurement is also referred to as a pole figure as it is often plotted in polar coordinates consisting of the tilt and rotation angles with respect to a given crystallographic orientation.

References

- [1] L. Civale, Maiorov B., Serquis A., Willis J. O., Coulter J. Y., Wang H., Jia Q. X., Arendt P. N., MacManus-Driscoll J. L., Maley M. P. & Foltyn S. R., *Appl Phys Lett* **84**, 2121 (2004).
- [2] L. Civale, Maiorov B., Serquis A., Foltyn S. R., Jia Q. X., Arendt P. N., Wang H., Willis J. O., Coulter J. Y., Holesinger T. G., MacManus-Driscoll J. L., Rupich M. W., Zhang W. & Li X., *Physica C* **412-14**, 976 (2004).
- [3] C. B. Eom, Marshall A. F., Suzuki Y., Geballe T. H., Boyer B., Pease R. F. W., Vandover R. B. & Phillips J. M., *Phys Rev B* **46**, 11902 (1992).
- [4] A. C. Westerheim, Anderson A. C., Oates D. E., Basu S. N., Bhatt D. & Cima M. J., *J Appl Phys* **75**, 393 (1994).
- [5] O. Castano, Cavallaro A., Palau A., Gonzalez J. C., Rossell M., Puig T., Sandiumenge F., Mestres N., Pinol S., Pomar A. & Obradors X., *Supercond Sci Tech* **16**, 45 (2003).
- [6] J. D. Jackson, "*Classical Electrodynamics*", John Wiley & Sons, New York (1998).
- [7] R. Feenstra, Christen D. K., Klabunde C. E. & Budai J. D., *Phys Rev B* **45**, 7555 (1992).
- [8] J. W. Anderson, Parrell J. A., Polak M. & Larbalestier D. C., *Appl Phys Lett* **71**, 3892 (1997).
- [9] L. Civale, *presented at 2003 Dept. of Energy Peer Review*
- [10] D. Dijkkamp, Venkatesan T., Wu X. D., Shaheen S. A., Jisrawi N., Minlee Y. H., Mclean W. L. & Croft M., *Appl Phys Lett* **51**, 619 (1987).
- [11] A. Inam, Hegde M. S., Wu X. D., Venkatesan T., England P., Miceli P. F., Chase E. W., Chang C. C., Tarascon J. M. & Wachtman J. B., *Appl Phys Lett* **53**, 908 (1988).
- [12] D. J. Dingley, Baba-Kishi K. Z. & Randel V., *Atlas of Backscattering Kikuchi Diffraction Patterns, Microscopy in Materials Science Series, Institute of Physics Publishing, 1995*
- [13] V. Randel, *The Measurement of Grain Boundary Geometry, Electron Microscopy in Materials Science Series, Institute of Physics Publishing, 1993*

- [14] P. Alers, *Phys Rev B* **105**, 104 (1957).
- [15] D. G. Schlom, Hellman E. S., Hartford E. H., Eom C. B., Clark J. C. & Mannhart J., *J Mater Res* **11**, 1336 (1996).

Chapter III. Influence of the grain boundary network on the critical current density

III.1 Introduction

Grain boundaries (GBs) of $\text{YBa}_2\text{Cu}_3\text{O}_{7-x}$ (YBCO) are well known as regions of weakened superconductivity. These are structurally and compositionally heterogeneous on scales of 1 – 5 nm, comparable to that of the coherence length, ξ . Low angle GBs consist of GB dislocations separated by conductive, grain-like channels [1]. The atomic disruptions and strain fields of the core depress the superconducting order parameter [1,2] and, thus, depress the supercurrent density. At small angles, e.g. 5° of [001] tilt, dislocation cores are separated by ~ 4 nm, so the channel can be more than ξ_{ab} (~ 3.5 nm at 77 K) wide, but the GB dislocation separation decreases inversely with increasing misorientation angle θ so that at about 10° the disruptive effects of strain and disorder close the channel. An important and poorly understood component of the disruption is loss of oxygen as means of minimizing the GB strain, which additionally weakens superconductivity across the GBs [3,4]. Wider oxygen-depleted regions have been seen at higher misorientations, exacerbating the weak coupling across the GB [3,4].

Suppressed superconductivity at the GB causes a reduced critical current density (J_c). It has been well established from [001] tilt bicrystal experiments [5-7] and micro-bridge experiments on coated conductors (CCs) [8] that J_c of GBs in bicrystals decreases exponentially with increasing misorientation angle θ , falling below that of the grain beyond

a critical angle θ_c of 3 - 4°. However, it is also becoming clear that θ_c is both field and temperature dependent [8-10], although so far θ_c is determined only at self-field.

Not only are J_c values across the GB depressed but so also do the vortex properties change, as is apparent in the voltage – current (V - I) characteristics. Typical V - I characteristics within the grain exhibit rather straight and evenly spaced traces when plotted in log-log V - I space [10] (Figure III.1(a)). However, V - I characteristics for a GB with $\theta > \theta_c$ show a steep rise in V and a ‘knee’ at higher voltage as shown in Figure III.1(b). The steep rise is a consequence of depinning of hybrid Abrikosov-Josephson vortices along the GB [11] before depinning of Abrikosov vortices within the grains adjacent to the GB [9].

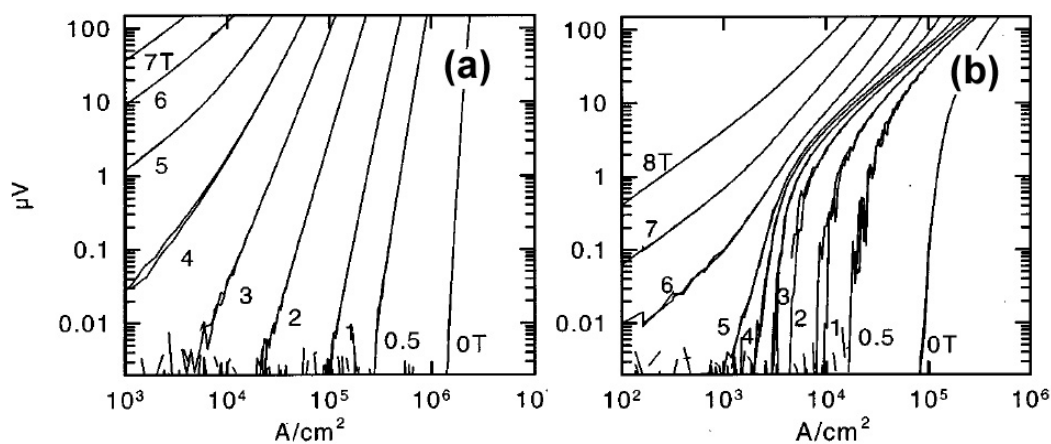


Figure III.1 Typical V - I plots (a) within the grains and (b) across a 10° [001] tilt GB [10].

The nature of the GB dissipation depends on both magnetic and electric field. In intermediate magnetic fields the V - I traces across a single GB often show hybrid behavior, in which there is grain-like dissipation at low voltage levels followed by a steep rise

characteristic of depinning of the GB vortices at mid-voltage levels, followed by a knee which makes the transition to broad flux flow dissipation in the grains at higher voltage levels [10]. The $V-I$ traces become more grain-like in higher magnetic fields as the GB dissipation signature disappears and flux flow in the grains dominates. The crossover field at which the grain starts to dissipate prior to the GB dissipation depends on misorientation angle. For a 7° bicrystal, the crossover field is between 5 T and 6 T at 77 K as shown in Gurevich *et al.* [11]. Verebelyi *et al.* found that the crossover field is around 4 T for a 3.8° GB and 0 T for a 2.0° ($< \theta_c$) GB [7] while Holzapfel *et al.* found a crossover field of 1 T for a 4° GB, 4 T for an 8° GB, and 6 T for a 12° GB [12].

The GB superconducting properties are affected by temperature too. Polyanskii *et al.* found by low field (~ 0.1 T) magneto-optic study [13] that $J_c(T)$ of low angle GBs with $3 - 10^\circ$ are less temperature dependent than $J_c(T)$ in the grain and thus that the difference between J_c of the grains and J_c of the GBs becomes less pronounced at higher temperature. In summary, the studies of single low-angle GBs shows that they become more single-crystal-like as temperature and magnetic field increases.

How this diversity of single GB behavior controls the J_c of coated conductors (CCs) is both interesting and technologically important. CCs are quasi-single-crystals consisting of a series-parallel network of predominantly low angle GBs, whose global properties result from series-parallel, multi-path percolative current transport [14,15].

The most practical way to evaluate the grain misorientation of CCs over large length scales is by x-ray diffraction, from which the full width half maximum (FWHM) of both in-plane ($\Delta\phi$) and out-of-plane ($\Delta\omega$) misorientations can be determined. However, it is

the grain-to-grain misorientation which actually determines the local intergranular current density. Although this local misorientation matrix can be determined by electron backscattering diffraction (EBSD) analysis, it is not feasible to do this on scales larger than about 1 mm^2 . Numerical simulations of the global J_c of CCs have been addressed by various models [16-18], which include the influence of the degree of texture, the number of grains in the tape width, and tape length. Such models indeed show that J_c values are reduced with worsening texture and decreasing number of grains within the tape width. However, such models suffer from a certain quantitative imprecision because the range of texture found in present CCs (FWHM of $\sim 4 - 8^\circ$) lies within the same range that the GB misorientation obstructs the current.

Based on the simplest analogy of a CC to the known properties of single GBs in bicrystals, it is expected that J_c of CCs gets reduced as the texture worsens, and that GB effects would become less pronounced as field and temperature rise. Consistent with this expectation, Fernandez *et al.* [19] found that a CC with a YBCO in-plane FWHM of 8° exhibited both significantly reduced J_c values compared to those expected from the intragranular behavior and a distinctive GB dissipation signature in the $V-I$ characteristics below 4 T at 77 K, while showing no GB limitation of J_c beyond 4 T at 77 K. They also reported that this GB-grain crossover field became progressively larger as the temperature decreased, consistent with the magneto-optical study of GB effects by Polyanskii *et al.* [13]. They clearly established that the domain within which the GB reduced J_c depended strongly on the temperature T and magnetic field H.

The purpose of the present experiment is to deepen the understanding of the influence of global texture on the critical current density using two recent CCs made by American Superconductor Corporation with smaller FWHM than that studied by Fernandez *et al.* [19]. Current study is amplified by cutting progressively narrower tracks into the better textured CC so as to observe changes in $J_c(H,T)$ behavior as the conductor moved from many grains to about one grain in width. These results on CCs are compared to a similarly made YBCO film grown on a single crystal substrate. The layout of this chapter is as follows. Section III.2 describes the experimental details. Section III.3 contrasts three nominal 1 μm -thick films with different textures by using broad-range measurements of $J_c(H,T)$ and electric field – current density (E - J) characteristics. Then, section III.4 reports the influence of the number of grains in the track width is explored by contrasting the transport behaviors of different bridge widths on the better-textured CC sample. In section III.5, it will be discussed how the current study delineates the influence of the grain boundary network in controlling the J_c properties at lower field and temperature, transitioning to a grain-dominated regime at higher fields and temperatures.

III.2 Experimental Details

All three nominal 1 μm thick YBCO films were grown using the same *ex situ* trifluoroacetate (TFA) – based precursor metal-organic deposition (MOD) process [20,21] at American Superconductor Corporation. Current bridges were defined on the CC samples ($\sim 300 \mu\text{m}$ wide by $\sim 500 \mu\text{m}$ long) by Nd-YAG (Yttrium Aluminum Garnet) laser ablation,

and on the single crystal (30 μm wide by 100 μm long) by photolithography so as to restrict critical current (J_c) to < 10 A at full thickness. The bridges on the CCs were more than 10 grains wide given the observed Ni-W template grain sizes of $\sim 20 - 40$ μm . The $V-I$ characteristics were obtained with standard four-point measurements. The measurements were performed over a wide range of magnetic fields up to 12 Tesla applied perpendicular to the film surface at temperatures of 77, 65, 50, 40 and 27 K. The J_c values were determined using the usual electric field criterion of 1 $\mu\text{V}/\text{cm}$. Although the MOD/TFA process produces a high- J_c YBCO layer, it is also porous with a surface roughness of order about 10 % of the thickness, which limits the absolute accuracy of our critical current density numbers to about the same value. The superconducting critical temperature (T_c) was determined as the onset of zero resistance.

The effect of the number of grains in the bridge width was investigated with the more highly textured CC. Bridges were initially defined by laser cutting tracks ~ 400 μm wide by ~ 1 mm long, after which the bridges were successively narrowed to ~ 50 μm width, about the grain size. To check the local GB misorientation distribution within the bridges, orientation mapping by electron backscattering diffraction (EBSD) was performed. Due to the surface roughness, we could not get good EBSD patterns from the YBCO and had to do this on the Ni-W after etching away the oxides. A magneto-optic image was taken on the bridge region by field-cooling the sample in a perpendicular field of 60 mT to 10 K. These showed up regions where the GB current density was lower than the grain current density.

Global texture measurements were made by x-ray diffraction. The in-plane texture was determined by the FWHM of the in-plane off-axis (ϕ) scan of the (103) YBCO peak while the out-of-plane texture was measured from the rocking curve of the (005) YBCO peak.

III.3 Influence of global texture on the critical current density

The key properties of the three samples are shown in Table III.1. The better textured, higher J_c sample (CC1) had 5.5° of in-plane FWHM ($\Delta\phi$) and 3.8° of out-of-plane FWHM ($\Delta\omega$), while the worse textured, lower J_c sample (CC2) had $\Delta\phi$ of 6.6° and $\Delta\omega$ of 6.1° , respectively. The $J_c(77\text{K},\text{self-field})$ values are directly correlated to the degree of texture. The single crystal sample (SC) achieved the very high J_c value of 5.3 MA/cm^2 at self-field, but $J_c(77\text{K},\text{sf})$ was reduced to 2.4 and 0.9 MA/cm^2 for CC1 and CC2, respectively. However at 1 T and 77 K relative differences in J_c were markedly smaller, values of 0.41 , 0.36 , and 0.11 MA/cm^2 being observed.

Sample No.	$\Delta\phi_{\text{YBCO}}$	$\Delta\omega_{\text{YBCO}}$	Bridge width (μm)	T_c (K)	$J_c(77\text{K},\text{sf})$ (MA/cm^2)	$J_c(77\text{K},1\text{T})$ (MA/cm^2)	$H^{cr}(77\text{K})$ (T)
SC	–	–	30	92	5.3	0.41	–
CC1	5.5°	3.8°	330	91	2.4	0.36	2
CC2	6.6°	6.1°	300	89	0.9	0.11	none
Ref. 19	8°	–	300	–	0.3	0.04	4

Table III.1 Key results of the measured samples (SC, CC1, CC2) and of [L. Fernandez et al., Phys. Rev. B 67, 052503 (2003)]

Figure III.2 shows $J_c(H)$ of the three samples at 77, 65, 50, 40, and 27 K. Some low-temperature, low-field data do not exist because of our 10 A current limit. The worse textured CC2 ($\Delta\phi \sim 6.6^\circ$, $\Delta\omega \sim 6.1^\circ$) always had significantly lower J_c values, in strong contrast to CC1 ($\Delta\phi \sim 5.5^\circ$, $\Delta\omega \sim 3.8^\circ$) and SC, which showed very similar $J_c(H)$ behavior over a large range of magnetic field (H) and temperature (T). At 65, 50, and 40 K, CC1 exhibits reduced J_c with respect to SC only at low fields. An interesting feature of Fig. III.2 is the parallel field dependence of $J_c(H)$ for all three samples in fields above a few Tesla. Only close to the irreversibility field at 77 K do the $J_c(H)$ curves differ. CC2 has about half the J_c of the SC and CC1 in high fields. It is striking that the differences in $J_c(H)$ between SC and CC1 disappear at the rather low field of ~ 2 T.

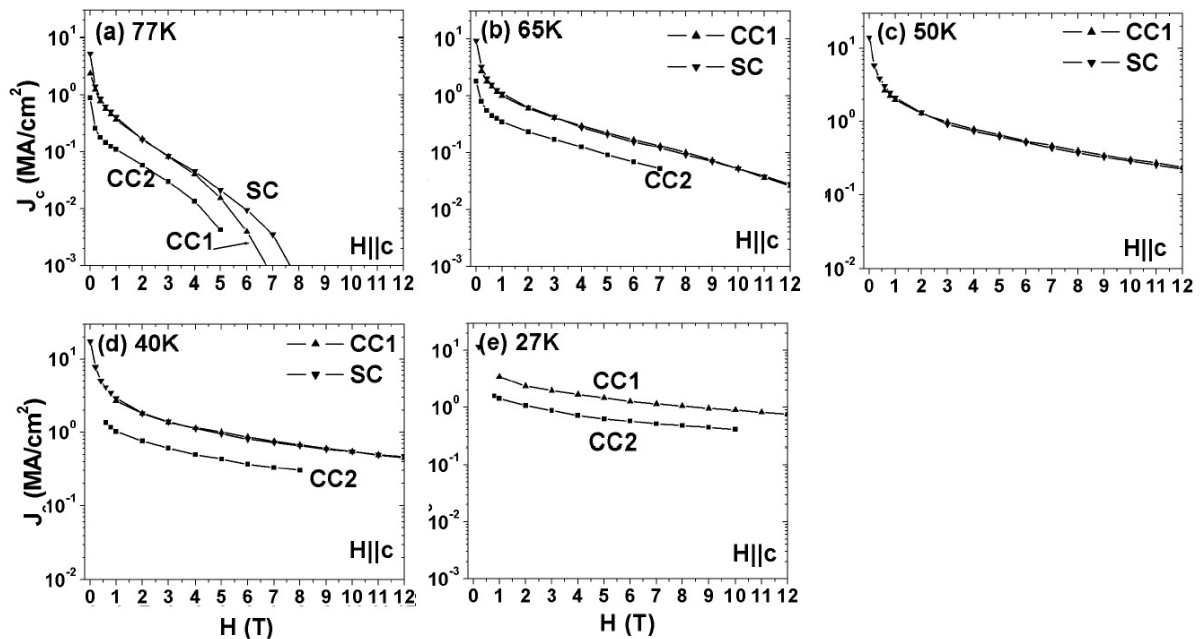


Figure III.2 $J_c(H)$ at variable temperatures (SC, CC1, and CC2); (a) 77 K, (b) 65 K, (c) 50 K, (d) 40 K, and (e) 27 K. The worse textured CC2 has significantly lower J_c values, in strong contrast to CC1 and SC, which showed very similar $J_c(H)$. Note that $J_c(H)$ of CC1 falling faster than that of SC at 77 K because of the T_c difference.

Figure III.3 presents the electric field – current density (E - J) characteristics of SC, CC1, and CC2 at 77 K and 65 K. SC exhibits typical intra-grain E - J characteristics. CC1 shows rather single-crystal-like E - J characteristics, as also, perhaps more surprisingly, does CC2. In fact there was no evidence of significant GB dissipation in the E - J curves of CC2, in spite of its strongly reduced J_c values.

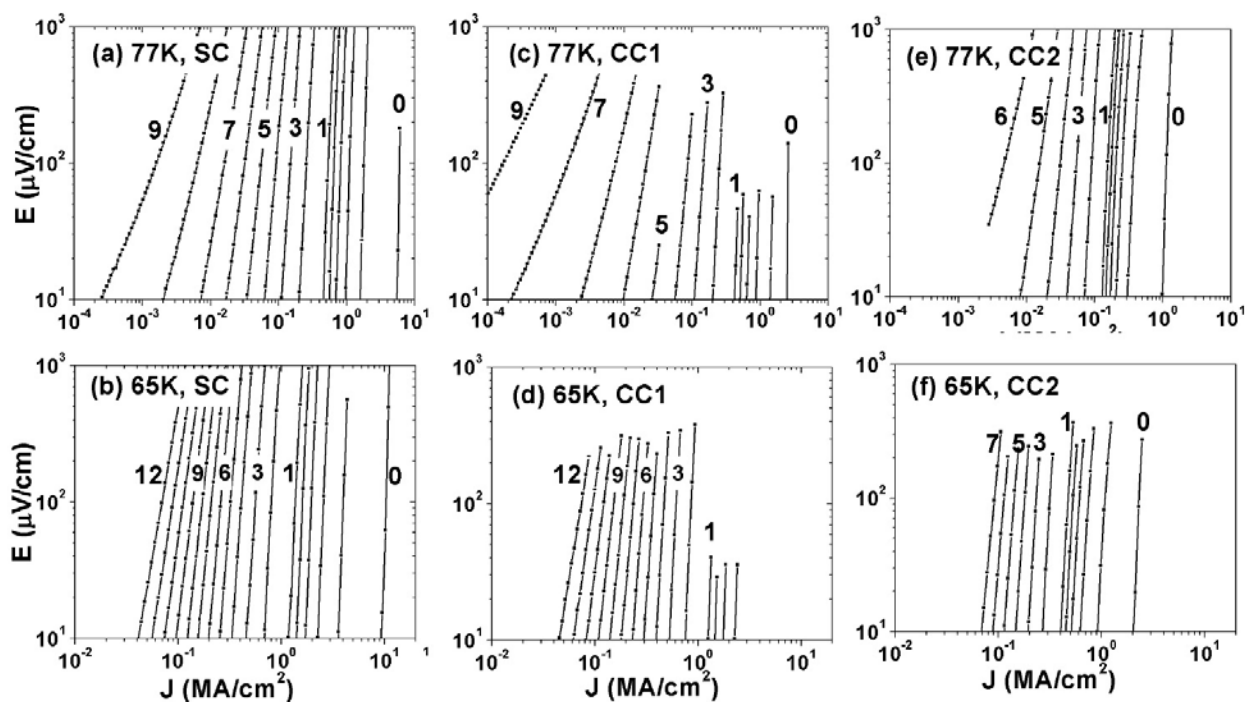


Figure III.3 E - J characteristics of (a)(b) SC, (c)(d) CC1, (e)(f) CC2 at (a)(c)(e) 77 K and (b)(d)(f) 65 K. The three samples show very similar single-crystal-like E - J characteristics in terms of their curve shape and their field dependence even for CC2 that has significantly lower J_c values.

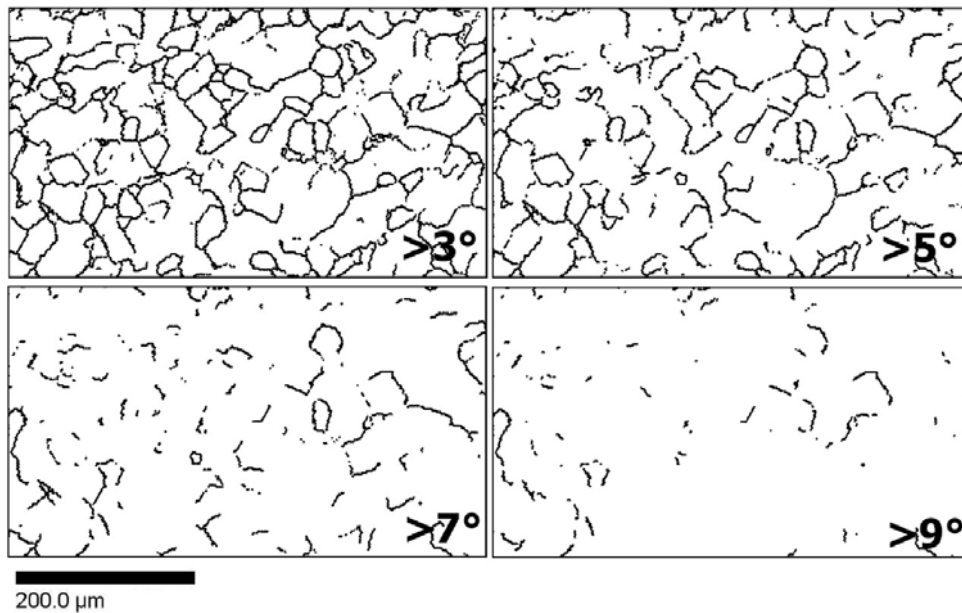


Figure III.4 Orientation mapping by electron-backscattering diffraction (EBSD) on the Ni-W substrate of the bridge region of CC2. The indicated angles are the combined one-angle-common-axis misorientation.

Figure III.4 shows the results of grain orientation mapping on the Ni-W substrate in the bridge region of CC2. The indicated angles (θ) are the combined one-angle-common-axis misorientation. The grain boundary network is almost completely developed for θ values of 3° , while at 7° most apparent grain boundaries are disconnected segments. Quite a few θ values exceed 9° , but these GB segments are even more isolated. Note that these misorientation angles are between grains on the Ni-W substrate, not on the YBCO. The GB in the YBCO could be smaller angle than in the Ni-W substrate [22], but not likely more than $1\text{-}2^\circ$. The discussion on the results follows in section III.5.

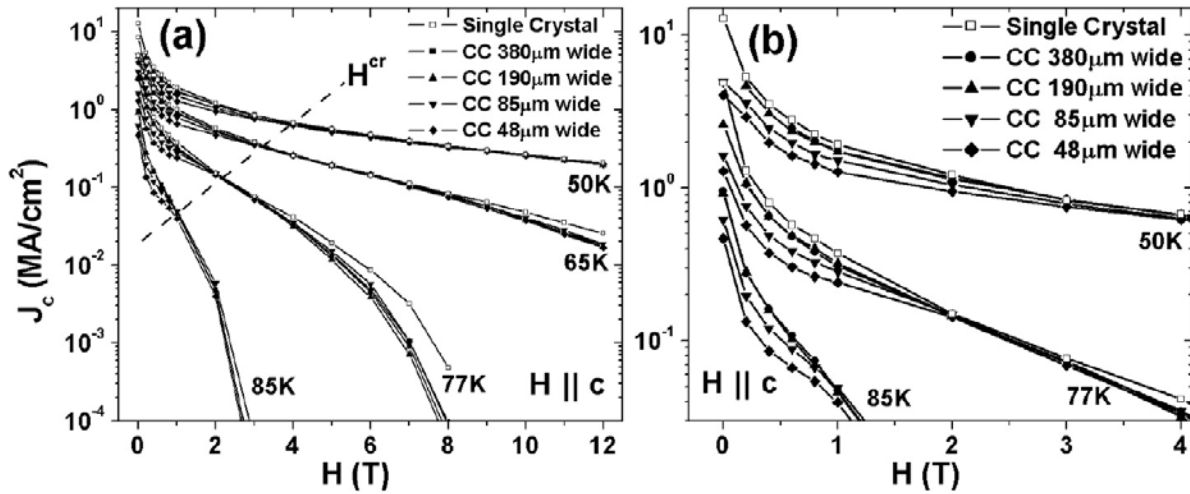


Figure III.5 (a) $J_c(H)$ for four different widths at 50, 65, 77 and 85 K up to 12 T. There is a noticeable reduction in J_c low magnetic fields as the track width is reduced, while all tracks behave identically beyond a crossover field indicated with a dashed line. This crossover field is surprisingly low, only 2 T at 77 K, rising to about 4 T at 50 K. (b) This expands the scale at low fields to emphasize the differences between the different track widths. The 65 K data is omitted to avoid overlapping. The two wider bridges - 380 μm and 190 μm widths - are identical, while the narrower bridges exhibit reduced J_c .

III.4 Influence of the number of grains within the bridge width

The influence of the number of grains within the bridge width was investigated with a second sample of the better-textured CC1. The $\Delta\phi$ and $\Delta\omega$ of the YBCO layer on this sample were 5.9° and 3.8° , respectively. T_c was 91 K, and J_c was 2.6 MA/cm^2 at 77 K and self-field.

The $J_c(H)$ characteristics for four different track widths varying from 380 to 48 μm at 50, 65, 77 and 85 K are shown in Figure III.5(a). There is a noticeable reduction in J_c at low magnetic fields as the track width is reduced, while all tracks behave identically beyond a crossover field (H^{cr}) shown by the dashed line. This crossover field is surprisingly low, only 2 T at 77 K, rising to about 4 T at 50 K. The open symbols are data for the single crystalline film. They show excellent agreement with the J_c curves of CC1 beyond the crossover field. The small high-field difference at 77 K and 65 K is again due to the 1 K higher T_c of the single crystalline sample (see Table III.1), an effect which becomes less pronounced as temperature decreases. Figure III.5(b) expands the scale at low fields to emphasize the differences between the different track widths. The two wider bridges – 380 μm and 190 μm width – are always identical, regardless of field and temperature and have only a slightly reduced J_c for $H < H^{cr}$ with respect to the single crystalline film. However, the 85 μm wide bridge does show a reduced J_c , while the 48 μm wide bridge exhibited even more reduced J_c below the crossover field. For example, the 85 μm wide bridge shows about 35 % reduced $J_c(\text{self-field})$ compare to the wide bridges and the 48 μm wide bridge about 50 % reduced $J_c(\text{self-field})$.

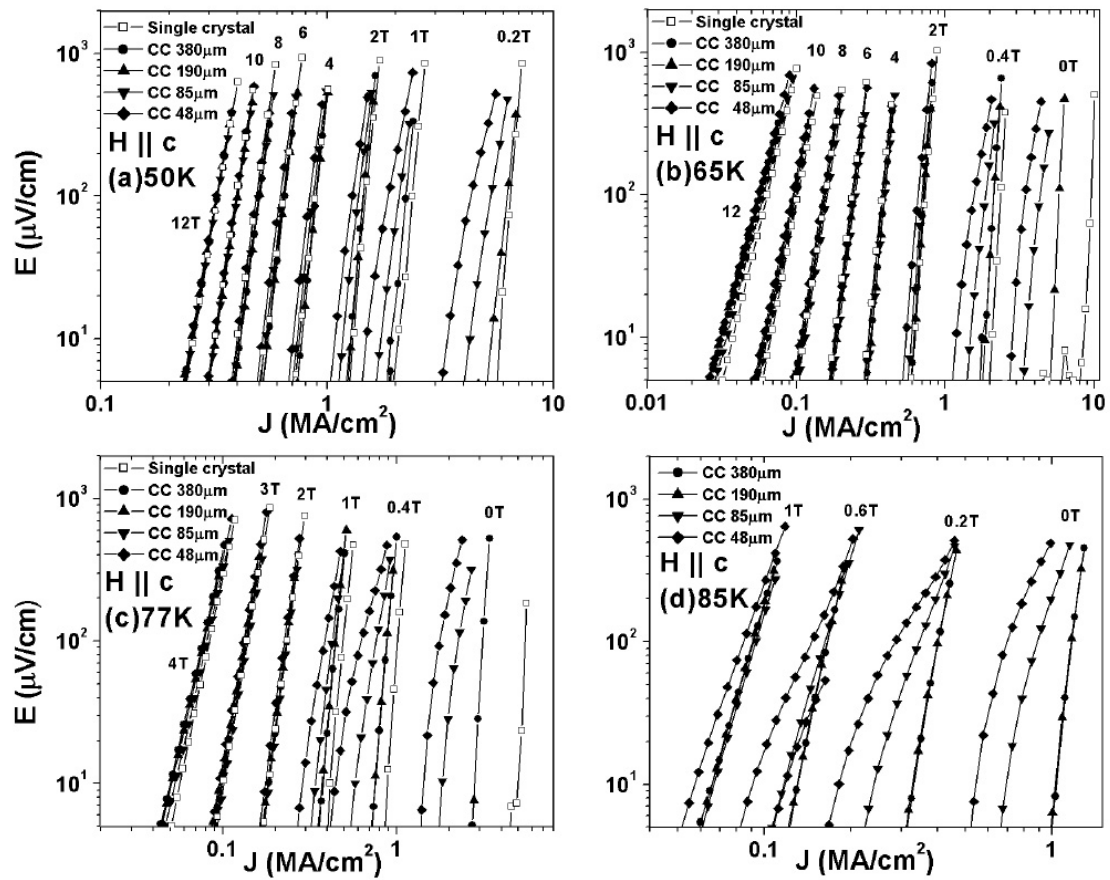


Figure III.6 E - J characteristics at (a) 50 (b) 65 (c) 77 and (d) 85 K. Open symbols are normalized data of the single crystalline film. Little GB dissipation signature is seen for the wider bridges, while GB dissipation signature is seen for the narrower bridges at low fields. The GB dissipation signature progressively weakens as field increases.

The E - J characteristics were measured and are shown in Figure III.6. The E - J characteristics of the two wide bridges are identical regardless of temperature and magnetic fields as already implied by their identical $J_c(H)$ behavior in Fig. III.5. (Note that some of self-field data for the widest bridge do not exist, because of the 10 A current limit of the experiment.) The E - J characteristics of the two wide bridges are also similar to those of the

single crystalline sample; neither set exhibits any significant GB dissipation signature. However, the two narrow bridges show a distinct broadening of the E - J characteristics at low voltage, typical of additional GB dissipation occurring in the narrower links. The 48 μm -wide bridge shows this GB dissipation more extensively than the 85 μm -wide bridge. However, the GB dissipation signature progressively weakens as the applied magnetic field increases, and disappears beyond the crossover field, H^{cr} .

Figure III.7 shows the results of grain orientation mapping on the Ni-W substrate in the bridge regions. Some θ values exceed 9° ; however such GB segments are always isolated ones. If the misorientation criterion is reduced to 3° , virtually all GB segments are linked, while at 5° many terminating GB segments appear. Note that these misorientation angles are between grains on the Ni-W substrate, not on YBCO. From x-ray measurements on this sample, we observed that the in-plane texture worsened slightly from 5.2° on the Ni-W to 5.9° on the YBCO, while the out-of-plane texture improved significantly from 6.0° to 3.8° . To understand better the source of the dissipation in the narrower tracks we performed magneto-optic (MO) imaging. The MO images were taken in the field-cooled condition in 60 mT at 10 K so as to emphasize any GB-current-limiting effects. The image shown in the middle of Fig. III.7 shows that only a few GBs with lower J_c than the grains appear in the 48 μm wide track and only one completely crosses the track. As noted later, the misorientation of this GB cluster is rather high.

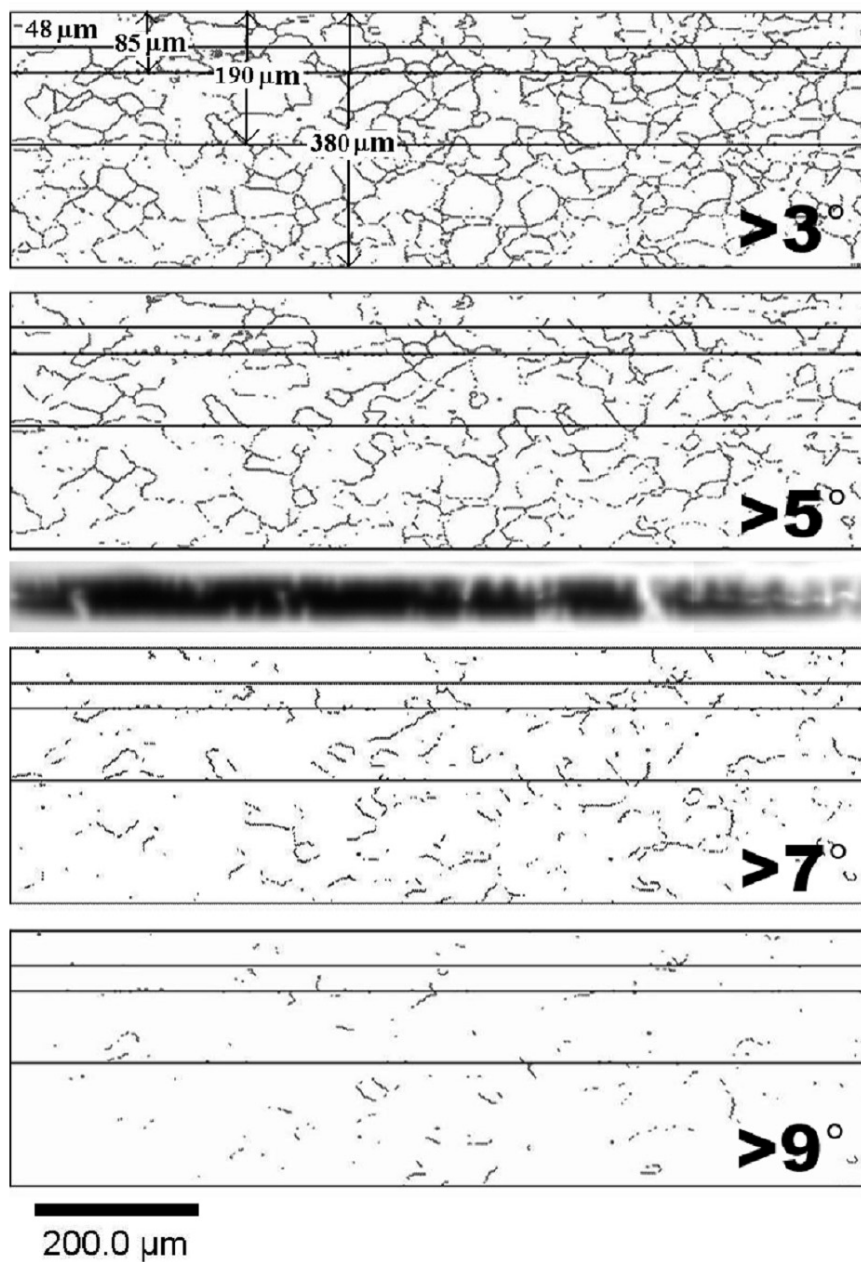


Figure III.7 Orientation mapping by electron-backscattering diffraction (EBSD) on the Ni-W substrate of the bridge region. The indicated angles are the combined one-angle-common-axis misorientation. Field-cooled magneto-optic image (MOI) on the narrowest bridge region is shown in the middle. Only a few GBs with lower J_c than the grains appears in the narrowest bridge and only one completely crosses the track.

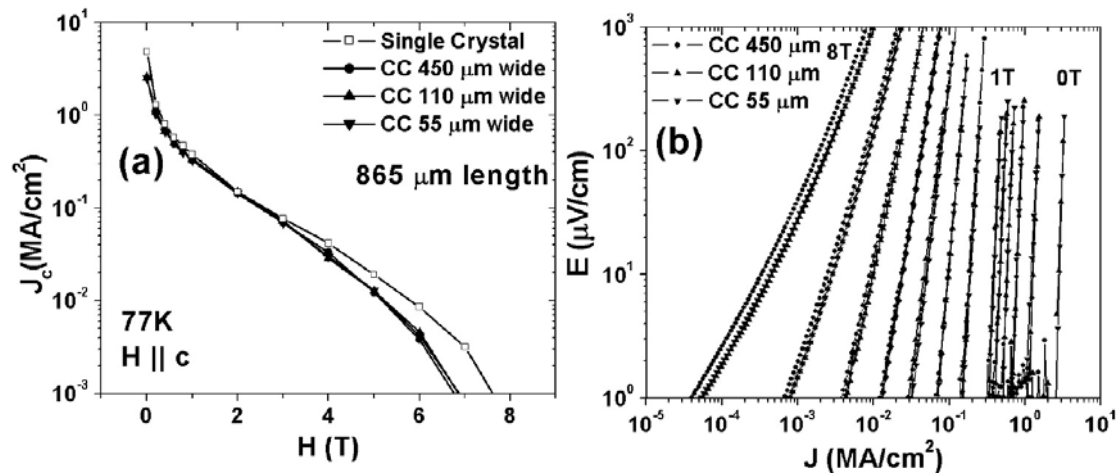


Figure III.8 (a) $J_c(H)$ and (b) E - J characteristics at 77 K of a second bridge set cut on other region of the same sample. No width dependence at all of either $J_c(H)$ or the E - J curves was seen. The E - J characteristics lack the grain boundary dissipation signature.

We also observed a second bridge set cut on other region of the same sample, whose width was successively narrowed from 450 μm to 55 μm. In this case, no width dependence at all of either $J_c(H)$ or the E - J curves was seen, even down to the 55 μm-wide bridge, as is shown in Figure III.8. The EBSD maps on the Ni-W substrate (Fig. III.9.) show several GBs with $\theta > 7^\circ$ in the narrowest bridge, making it especially interesting that the E - J characteristics lack the grain boundary dissipation signature (Fig.III.8(b)).

III.5 Discussion

A key issue for understanding the attainable critical current density of coated conductors is first to understand the range of fields and temperatures over which J_c is reduced by the grain boundary network. The present work suggests several ways in which

the GB network and its misorientation distribution can control J_c given that a CC is generally many grains wide and presents a complex set of series-parallel current paths defined by obstacles around which current flows percolatively. The recent study of a RABiTS conductor by Fernandez *et al.* [19] was clearly able to distinguish the domain in which the GBs controlled $J_c(H,T)$ in their conductor. They found a non-ohmic linear dissipation (NOLD) in the E - J curves of their 6-7-grain-wide conductor and a power-law dependence of $J_c(H,T)$ when GBs controlled J_c and an exponential dependence without any NOLD signature when flux pinning within the grains controlled J_c . At 77 K this crossover occurred at about 4 T and a current density of 0.01 MA/cm². Our study nicely complements theirs because the FWHM of the YBCO of their conductor was $\sim 8^\circ$, rather larger than our three samples.

It is clear from comparing the J_c and FWHM data in Table III.1 that the FWHM exercises a powerful effect on J_c . $J_c(77K,0T)$ rises from 0.3 MA/cm² ($\Delta\phi$ FWHM 8°) through 0.9 MA/cm² (6.6°) through 2.4 MA/cm² (5.5°) to 5.3 MA/cm² for the single crystal. At 1 T where the GB network influence is somewhat reduced for all three CC, the respective J_c values are 0.04, 0.11, 0.36 and 0.41 MA/cm². At 77 K the crossover field H^{cr} at which the GB and intragrain J_c become identical was 4 T for Fernandez *et al.* ($\Delta\phi_{YBCO} \sim 8^\circ$), while curiously no crossover was seen for our CC2 ($\Delta\phi_{YBCO} \sim 6.6^\circ$). For the better-textured CC1 ($\Delta\phi_{YBCO} \sim 5.5^\circ$), a crossover from GB to grain control was observed at ~ 2 T at 77 K. As FWHM values of YBCO layers have come down in recent years, e.g. 4.5° on

RABiTS [21] and 2.5° on IBAD-MgO [21], the possibility of real single-crystal-like behavior on CC indeed increases.

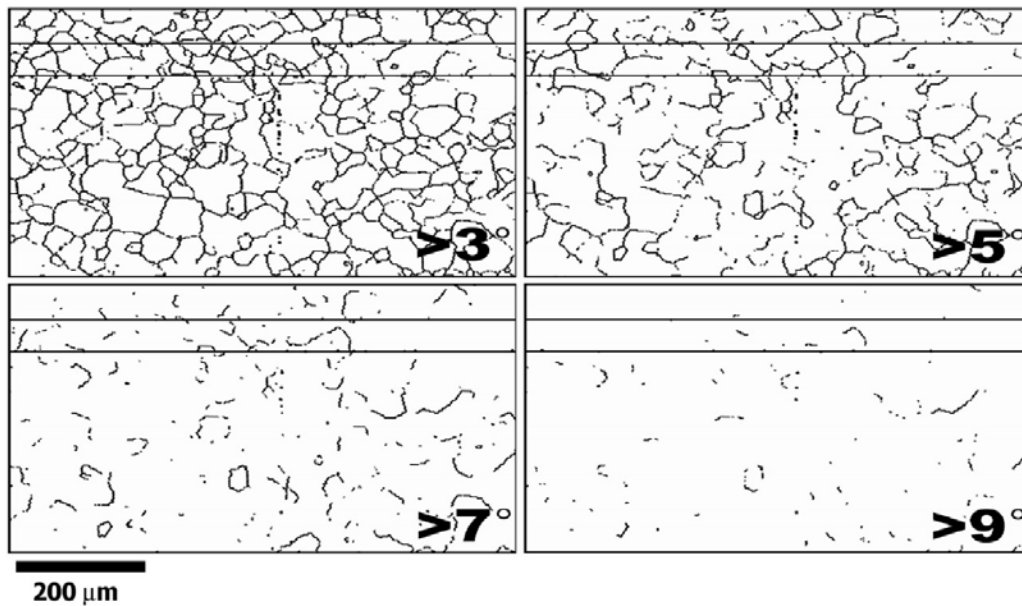


Figure III.9 Orientation mapping by electron-backscattering diffraction (EBSD) on the Ni-W substrate of the second bridge region. Several GB angles are higher than 7° in the narrowest track.

A second significant difference between the conductor of Fernandez *et al.* and ours was that they saw the NOLD signature of GB dissipation very widely, while we saw this signature only when we narrowed the bridge to 1-2 grains wide, as shown in Fig. III.6. In our ~ 7 -grain-wide bridges, no NOLD signature was visible in either CC1 or CC2 at any field or temperature. More explicitly, we did not observe any NOLD signature even for the narrowest track of the second bridge set, which contains several GBs with θ higher than 7° (Fig III.8).

The collective behavior observed in our two studies can be summarized briefly as follows: (i) the highest J_c values were seen in the single crystals where no grain boundaries are present. In spite of much data that show significant degradation of J_c with increasing thickness [23-28], $J_c(77K,0T)$ was much higher for the 1 μm thick MOD film than for the 0.2 μm thick PLD film of Fernandez *et al.*, 5.3 versus 2 MA/cm². The lower $J_c(H,T)$ properties of the PLD CC were seen at all fields – for example at 4 T and 77 K (H^{cr} for the PLD CC), J_c was ~ 0.01 MA/cm² compared to 0.05 MA/cm² for the MOD single crystal film, (ii) Although the crossover from GB to grain control of J_c is clearly seen in the E - J curves for the wide-bridge PLD CC [19], no crossover in the E - J curves is seen for the higher J_c MOD coated conductors. A distinctive GB signature was shown when we narrowed the track to one or two grains but the influence on the MOD-CC E - J curves was much less strong than in the PLD-CC, as can be seen by comparing our Fig. III.6 to Fig. 4 of Ref. 19. However we were able to see the crossover from GB to grain control by comparison of the $J_c(H,T)$ of the single crystal to CC1 and especially in the narrow track $J_c(H,T)$ data taken on CC1.

An overview of the GB misorientation distributions in the Ni-W templates of CC1 and CC2 is given in Fig. III.4 (CC2) and Figs. III.7 and III.8 (CC1). It is clear for both CC1 and CC2 that a major change in connectivity occurs at misorientations between 5° and 7°. At 5° or less the GB network is essentially complete so that long-range current flow must cross this whole grain boundary network. However, if only grain boundaries with $\theta > 7^\circ$ are considered, then continuous current paths exist which do not cross the GB network, although current would still be obstructed by the set of predominantly disconnected GB

segments appear that would be expected to act as partial obstacles with strong dissipation at their ends [29,30]. If we reduce these θ values by 1-2° to account for the usual orientation improvement on YBCO growth, the critical change appears to occur at about 5-6° of YBCO misorientation for both conductors, although it does appear that the obstacle density at this θ is visibly greater in CC2 than in CC1. This conclusion is made even more explicit by the magneto-optical image in Fig. III.7. In this case only one grain boundary shows up as having a lower J_c than the rest of the track. The majority of this visible GB has $\theta_{Ni-W} > 7^\circ$ and a small portion $> 9^\circ$. Many small segments with the same misorientations exist in the track but do not show up at all or just as partial penetrations.

The result of many bicrystal studies of YBCO grown by PLD on STO or YSZ bicrystals is that the critical angle is 3-4° [7,8,10]. Thus a substantial GB signature and reduced J_c would be expected from all 3 coated conductors. But, only the PLD-RABiTS conductor shows NOLD behavior, although all three do show a J_c reduction at zero field and 77 K.

In considering the role of grain boundaries in controlling $J_c(H,T)$ of coated conductors it has generally been assumed that data taken on 200 – 400 nm thick films grown generally by PLD on SrTiO₃ or YSZ bicrystal substrates are equally valid for 1-2 μ m thick coated conductors. Indeed a number of modeling studies take this input and use it to compute the critical current of long conductors as a function of their FWHM distributions [16-18]. But several prior experiments have shown that the influence of grain boundaries is complex. The fact that the ratio of J_{gb}/J_g depends on field is attested by multiple studies [7,10,13]. More recently Durrell *et al.* [31] have shown that the angle made by the magnetic

field to the grain boundary plane affects both the magnitude of J_{gb} and the appearance of the distinctive NOLD GB signature. When the field lay within the GB plane of their 4.9° [001] tilt bicrystal, a distinctive NOLD signature and reduction of J_{gb} was found. However, when they placed the magnetic field within the ab plane and rotated H with respect to the grain boundary plane which lay parallel to the c axis, they found that J_{gb} was neither reduced nor was there any NOLD signature when the field deviated by more than $\sim 30^\circ$ from the GB plane. The NOLD signature is developed both by the distortion of vortex core structure produced by depressed superconductivity at the GB [11] and by alignment of the vortices in the GB so that a channel of weakly pinned hybrid Abrikosov-Josephson vortices is depinned at a rather sharp value of Lorentz force. Durrell's observation develops this model for the case where the field makes an angle to the GB so that only a small segment of any one vortex possesses a weakly pinned GB segment. Evidently the intragrain components of such vortices are sufficient to pin the GB segments, removing the NOLD signature in the E - J curve and enhancing J_{gb} .

The geometry of the present case is different from that of Durrell *et al.*[31] In our case all testing was done in the usual way with field parallel to the c -axis. But recent observations by Feldmann *et al.*[22] and Holesinger *et al.*[32] show that thick MOD films have grain boundaries which do not grow vertically, but at oblique angles that are often as small as 10 - 15° to the substrate. Thus the conditions of the Durrell experiment can be frequently fulfilled in these MOD conductors too. Experiments to test this hypothesis explicitly are currently in progress.

III.6 Summary

Extensive measurements of the E - J characteristics of recent 1 μm thick MOD conductors were made, and the results were compared to the earlier study of an 0.2 μm thick PLD conductor [19]. It is found that the influence of $\Delta\phi$ on J_c is highly non-linear, $J_c(77K,0T)$ rising by more than 8 times as the FWHM of $\Delta\phi_{YBCO}$ decreases only from 8 to 5.5°. This is very good news for the technology of coated conductors because it makes it clear that the critical angle is significantly greater than found in previous, significantly thinner scientific bicrystal studies [5-11]. The second striking result is that the MOD coated conductors do not possess the strongly dissipative NOLD signature familiar from thin PLD films [7,9,10,19,31] and that, even when we were able to conclusively identify a dissipative GB, its misorientation was much larger than expected ($\sim 6^\circ$) and the NOLD signature was very attenuated. Thus although the low field performance of these high- J_c coated conductors is still limited by grain boundaries, the effects appear to be much less than should be expected from the FWHM distributions.

References

- [1] M. F. Chisholm & Pennycook S. J., *Nature* **351**, 47 (1991).
- [2] N. D. Browning, Buban J. P., Nellist P. D., Norton D. P., Chisholm M. F. & Pennycook S. J., *Physica C* **294**, 183 (1998).
- [3] Y. M. Zhu, Zuo J. M., Moodenbaugh A. R. & Suenaga M., *Philos Mag A* **70**, 969 (1994).
- [4] S. E. Babcock, Cai X. Y., Larbalestier D. C., Shin D. H., Zhang N., Zhang H., Kaiser D. L. & Gao Y. F., *Physica C* **227**, 183 (1994).
- [5] D. Dimos, Chaudhari P., Mannhart J. & Legoues F. K., *Phys Rev Lett* **61**, 219 (1988).
- [6] D. Dimos, Chaudhari P. & Mannhart J., *Phys Rev B* **41**, 4038 (1990).
- [7] D. T. Verebelyi, Christen D. K., Feenstra R., Cantoni C., Goyal A., Lee D. F., Paranthaman M., Arendt P. N., DePaula R. F., Groves J. R. & Prouteau C., *Appl Phys Lett* **76**, 1755 (2000).
- [8] D. M. Feldmann, Larbalestier D. C., Verebelyi D. T., Zhang W., Li Q., Riley G. N., Feenstra R., Goyal A., Lee D. F., Paranthaman M., Kroeger D. M. & Christen D. K., *Appl Phys Lett* **79**, 3998 (2001).
- [9] A. Diaz, Mechin L., Berghuis P. & Evetts J. E., *Phys Rev B* **58**, R2960 (1998).
- [10] N. F. Heinig, Redwing R. D., Nordman J. E. & Larbalestier D. C., *Phys Rev B* **60**, 1409 (1999).
- [11] A. Gurevich, Rzechowski M. S., Daniels G., Patnaik S., Hinaus B. M., Carillo F., Tafuri F. & Larbalestier D. C., *Phys Rev Lett* **88**, 097001 (2002).
- [12] B. Holzapfel, Verebelyi D., Cantoni C., Paranthaman M., Sales B., Feenstra R., Christen D. & Norton D. P., *Physica C* **341**, 1431 (2000).
- [13] A. A. Polyanskii, Gurevich A., Pashitski A. E., Heinig N. F., Redwing R. D., Nordman J. E. & Larbalestier D. C., *Phys Rev B* **53**, 8687 (1996).
- [14] J. E. Evetts, Hogg M. J., Glowacki B. A., Rutter N. A. & Tsaneva V. N., *Supercond Sci Tech* **12**, 1050 (1999).

- [15] B. Holzapfel, Fernandez L., Schindler F., de Boer B., Reger N., Eickemeyer J., Berberich P. & Prusseit W., *IEEE Trans Appl Supercon* **11**, 3872 (2001).
- [16] N. A. Rutter, Glowacki B. A. & Evetts J. E., *Supercond Sci Tech* **13**, L25 (2000).
- [17] E. D. Specht, Goyal A. & Kroeger D. M., *Supercond Sci Tech* **13**, 592 (2000).
- [18] Y. Nakamura, Izumi T. & Shiohara Y., *Physica C* **371**, 275 (2002).
- [19] L. Fernandez, Holzapfel B., Schindler F., de Boer B., Attenberger A., Hanisch J. & Schultz L., *Phys Rev B* **67**, 052503 (2003).
- [20] M. W. Rupich, Schoop U., Verebelyi D. T., Thieme C., Zhang W., Li X., Kodenkandath T., Nguyen N., Siegal E., Buczek D., Lynch J., Jowett M., Thompson E., Wang J. S., Scudiere J., Malozemoff A. P., Li Q., Annavarapu S., Cui S., Fritzemeier L., Aldrich B., Craven C., Niu F., Schwall R., Goyal A. & Paranthaman M., *IEEE Trans Appl Supercon* **13**, 2458 (2003).
- [21] X. Li, Rupich M. W., Zhang W., Nguyen N., Kodenkandath T., Schoop U., Verebelyi D. T., Thieme C., Jowett M., Arendt P. N., Foltyn S. R., Holesinger T. G., Aytug T., Christen D. K. & Paranthaman M. P., *Physica C* **390**, 249 (2003).
- [22] D. M. Feldmann, *Ph.D. thesis, University of Wisconsin - Madison, 2001*
- [23] S. R. Foltyn, Tiwari P., Dye R. C., Le M. Q. & Wu X. D., *Appl Phys Lett* **63**, 1848 (1993).
- [24] X. D. Wu, Foltyn S. R., Arendt P., Townsend J., Campbell I. H., Tiwari P., Jia Q. X., Willis J. O., Maley M. P., Coulter J. Y. & Peterson D. E., *IEEE Trans Appl Supercon* **5**, 2001 (1995).
- [25] S. R. Foltyn, Jia Q. X., Arendt P. N., Kinder L., Fan Y. & Smith J. F., *Appl Phys Lett* **75**, 3692 (1999).
- [26] B. W. Kang, Goyal A., Lee D. R., Mathis J. E., Specht E. D., Martin P. M., Kroeger D. M., Paranthaman M. & Sathyamurthy S., *J Mater Res* **17**, 1750 (2002).
- [27] K. J. Leonard, Goyal A., Kroeger D. M., Jones J. W., Kang S., Rutter N., Paranthaman M., Lee D. F. & Kang B. W., *J Mater Res* **18**, 1733 (2003).
- [28] D. M. Feldmann, Larbalestier D. C., Feenstra R., Gapud A. A., Budai J. D., Holesinger T. G. & Arendt P. N., *Appl Phys Lett* **83**, 3951 (2003).
- [29] A. Gurevich & Friesen M., *Phys Rev B* **62**, 4004 (2000).

- [30] D. Abraimov, Feldmann D. M., Polyanskii A. A., Gurevich A., Daniels G., Lerbalestier D. C., Zhuravel A. P. & Ustinov A. V., *Appl Phys Lett* **85**, 2568 (2004).
- [31] J. H. Durrell, Hogg M. J., Kahlmann F., Barber Z. H., Blamire M. G. & Evetts J. E., *Phys Rev Lett* **90**, 247006 (2003).
- [32] T. G. Holesinger, (*private communication*)

Chapter IV. Improvement of low angle grain boundary transparency

The rapid decrease of the critical current density J_c with grain boundary misorientation angle θ essentially limits the current-carrying capability of YBCO coated conductors (CC) as discussed in Chapter III. Even though the in-plane texture of the YBCO coated conductors made by the RABiTS route becomes improved, generally only 4-6° of full-width half-maximum FWHM, the previous study of the current-limiting mechanisms of the grain boundary network in real MOD coated conductors has shown that even the very best CC made on RABiTS today still have their low field J_c limited by the grain boundary network. In addition, the GB network effect becomes more serious when the tape is subdivided into narrow bridges in order to reduce AC losses. Since most electric utility applications use fields less than 3 T and are expected to operate in AC conditions, the enhancement of grain boundary properties in low magnetic fields remains very important. This chapter concentrates on further understanding GBs to explore ways to enhance the GB transport properties of YBCO, $J_{c,gb}$.

The approach is to investigate enhancement of GB transport properties by reducing the underdoping (oxygen vacancies) at GBs that deteriorate GB properties [1]. *Ca-doping* in YBCO ($Y_{1-x}Ca_xBa_2Cu_3O_{7-\delta}$) is the presently proven method [2-4]. The number of charge carriers (holes) increases at the GB by substituting bivalent Ca^{2+} for trivalent Y^{3+} , thereby

reducing the charge carrier depletion near the boundaries. Another possibility to reduce the carrier depletion near the GB is reducing strain field (induced by lattice distortion) around the GB dislocation by the proper *cation substitution*, which reduces the amount of ejected oxygen. Thus, Ca-doping or other cation-substitution can recover the optimal carrier doping state near the GB dislocation, and thus, can improve grain boundary critical current density $J_{c,gb}$.

This chapter begins with the detailed introduction to carrier doping effects in YBCO. Carrier doping is important since the superconducting properties (mainly T_c) of the YBCO depend strongly on the carrier density, while the carrier density can be modified by Ca-doping or more general cation-doping. Therefore, it is necessary to understand carrier doping in *the YBCO grains* (section IV.1.1) and *at the grain boundaries* (section IV.1.2). Then, section IV.2 briefly discusses the flux flow behavior at the GB, from which the grain boundary depairing current density can be derived.

Transport characteristics of low angle GBs with different Ca content x ($Y_{1-x}Ca_xBa_2Cu_3O_{7-\delta}$) have been first examined to verify the influence of the density of carriers at the GB due to the Ca doping level. The results will be described in section IV.3. A cation segregation model [5] recently developed by A. Gurevich predicts that Ca^{2+} segregates at the GB dislocation due to the pressure field and the electric potential around low angle GB dislocation cores. The driving force for Ca segregation is the size and valence difference between Y^{3+} and Ca^{2+} . Ca^{2+} segregation at the GB dislocation core produces an enhanced charge carrier density (holes) both by the substitution and by the strain relief produced by expanding the core, thus causing the transport properties to

change according to the Ca doping level. The goal is to find the optimum Ca concentration for lower angle (6-9°) grain boundaries found in CCs. Section IV.4 focuses on the Ca-doping influence in the $(\text{Yb})_{1-x}\text{Ca}_x\text{Ba}_2\text{Cu}_3\text{O}_{7-\delta}$ system. Ca segregation at the $\text{YbBa}_2\text{Cu}_3\text{O}_{7-\delta}$ GB cores is expected to be stronger than at YBCO GBs, since the size difference between smaller Yb^{3+} and Ca^{2+} is larger than between Y^{3+} and Ca^{2+} . Therefore, less Ca doping should be optimum. Lastly in section IV.5, the transport characteristics of $\text{Y}_{1-x}\text{Nd}_x\text{Ba}_2\text{Cu}_3\text{O}_{7-\delta}$ grain boundaries will be reported. The pressure field around GB cores would drive the larger Nd^{3+} ion to segregate at the GB dislocation, while the substitution of trivalent Nd^{3+} for trivalent Y^{3+} does not modify carrier density in the grains. It is expected that the Nd segregation at the GB dislocation can relieve the strain, so enhancing the GB transport properties. This could be very useful, since the substitution of Nd^{3+} for Y^{3+} is known not to degrade the T_c of the grains significantly, unlike Ca-doping. The summary will be given in section IV.6

The predictions of the cation segregation model [5] will be used to interpret the transport characteristics of each system investigated. The details of the cation segregation model will be given in section IV.1.2. Further study beyond the current thesis work will explicitly check the atomistic and carrier density predictions of the segregation model by atomic resolution analytical electron microscopy, including advanced transmission electron microscopy (TEM), Z-contrast scanning transmission electron microscopy imaging, and electron energy-loss spectroscopy (EELS). The collaboration has been arranged with a skilled analytical electron microscopist, Dr. Yan Xin, Associate Scientist at National High Magnetic Field Laboratory. This work will not be the part of the current thesis work.

IV.1 Introduction to carrier doping effect in YBCO

IV.1.1 Charge carrier doping in YBCO grains

High temperature superconductor (HTS) materials, including YBCO, undergo an insulator \rightarrow superconductor \rightarrow normal metal transition as the charge carrier concentration increases (Figure IV.1). The T_c of the superconducting phase depends on the carrier level in the system and the maximum T_c , $T_{c,max}$, appears at an optimum carrier level c_m . Carrier doping in YBCO is more subtle because the charge carrier density can be changed either by the oxygen contents, substituting other cations with different valence ions (e.g. Ca^{2+} for Y^{3+}), or varying the ratio of cations in the formula unit (e.g. $(RE)_{1+x}Ba_{2-x}Cu_3O_{7-\delta}$). The charge carrier in YBCO is a hole in the CuO_2 plane.

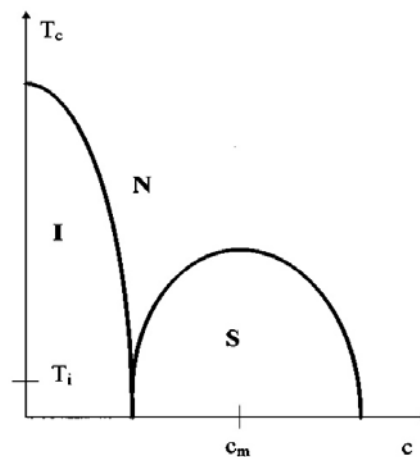


Figure IV.1 (a) Phase diagram $T_c(c)$ of HTS, where I, N, and S correspond to the insulating, normal, and superconducting states, respectively. c is hole (charge carrier) concentration on the Cu-O planes and c_m is the optimum concentration, which generally occurs at a value c_m of ~ 0.16 .

First of all, charge carrier density in YBCO is changed by the oxygen contents. In the YBCO structure there are two different copper layers (see Fig. I.1), one (Cu-O chain) between the barium planes and two (CuO₂ planes) between the yttrium and barium planes. The Cu-O chains act as charge reservoirs that transfer holes to the CuO₂ planes, whose density can be modified by varying the total oxygen content '7- δ ' in YBa₂Cu₃O_{7- δ} (δ ~ oxygen deficiency) [6-8] by controlling the oxygen annealing condition. However, fully oxygenated YBCO only enters the slightly overdoped regime. It is known that the oxygen deficiency δ shows up in the Cu-O chains, making their formula CuO_{1- δ} . When the total oxygen is less than 6.4 ($\delta > 0.6$), YBCO is in the anti-ferromagnetic insulating phase. However, below $\delta \sim 0.6$ where YBCO exhibits superconductivity, the hole concentration at the CuO₂ planes increases with further decreasing oxygen deficiency δ [9]. As δ varies, the number of hole carriers varies [10] as shown in Figure IV.2, and so does the T_c, as shown in Figure IV.3 [6,7].

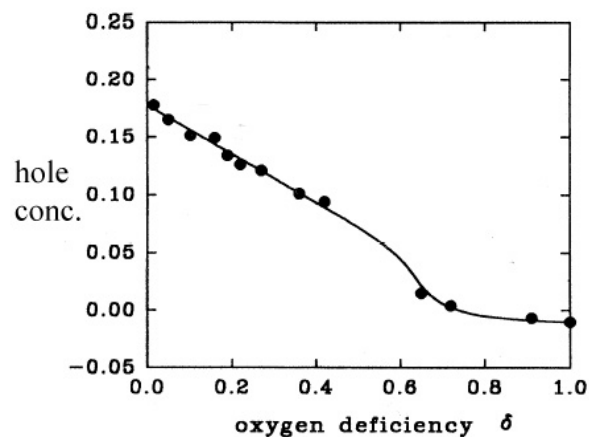


Figure IV.2 Hole concentration per Cu atom versus oxygen deficiency δ for YBa₂Cu₃O_{7- δ} . The hole concentration is estimated by the bond valence sum (J.L. Tallon *et al.* [10]).

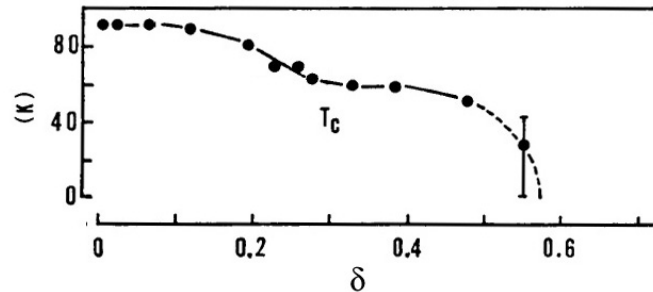


Figure IV.3 T_c versus oxygen contents in YBCO from E. Takayamamuromachi *et al.* [6].

Second, hole doping in the YBCO grains can be achieved also by the partial substitution of bivalent 2+ alkaline earth ions like Ca for the trivalent 3+ rare earth ions Y in YBCO; $Y_{1-x}Ca_xBa_2Cu_3O_{7-\delta}$. In this case, the substitution of Ca^{2+} introduces hole carriers in the to CuO_2 planes, independent of those produced by oxygen deficiency in the $CuO_{1-\delta}$ chain [10-12]. Excess holes provided by the substitution (Y^{3+}/Ca^{2+}) drive some Cu^{2+} in the CuO_2 plane to Cu^{3+} (or $Cu-O^+$). The hole concentration $[Cu-O]^+$ is the fraction of holes per Cu atom in the CuO_2 planes. This alkaline element substitution allows the YBCO system access into the over-doped regime. For example, oxygen-deficient $Y_{1-x}Ca_xBa_2Cu_3O_6$ ($\delta=1$) provides the ability to add holes in a hole-deficient crystal as x increases [10], while oxygenated $Y_{1-x}Ca_xBa_2Cu_3O_{7-\delta}$ with $\delta \sim 0.04$ enables hole-overdoping as x increases [10]. Figure IV.4 shows T_c values for $Y_{1-x}Ca_xBa_2Cu_3O_6$ as a function of x ($\delta=1$, round symbols), exhibiting the transition from the non-superconducting (hole-deficient) to the superconducting state as the density of hole increases. Figure IV.4 also includes T_c values for $Y_{1-x}Ca_xBa_2Cu_3O_{7-\delta}$ when

$\delta \sim 0.04$ (square symbols) as a function of x , providing a transition from optimal hole concentration to hole-excess (over-doping).

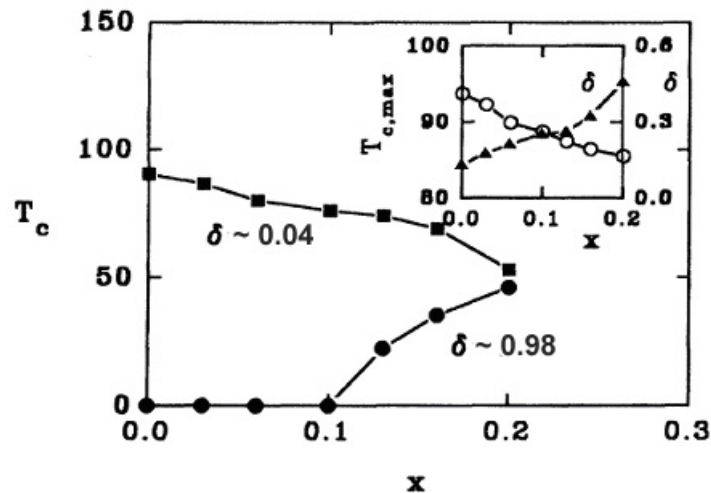


Figure IV.4 T_c values for $Y_{1-x}Ca_xBa_2Cu_3O_{7-\delta}$ plotted as a function of x for $\delta \sim 0.04$ (overdoped) and $\delta \sim 0.98$ (underdoped). Inset: $T_{c,max}$ and δ values for optimum doping versus x . Figure taken from Fig.1 of J.L. Tallon *et al.* (Ref. [10]).

Lastly, hole concentration compensation can occur when the cation ratio departs from the fixed 1:2:3. Some $(RE)Ba_2Cu_3O_{7-\delta}$ systems (RE is a rare earth ion) can form solid solutions in which the Ba site can interchange with rare earth ions, if the RE ions are large enough (e.g. La, Nd, Sm, or Eu). They can form single-phase $(RE)_{1+x}Ba_{2-x}Cu_3O_{7-\delta}$ in which the hole density decreases by partial substitution of trivalent $(RE)^{3+}$ for bivalent Ba^{2+} . As x increases and the hole density decreases, T_c decreases [13]. For example, $Nd_{1+x}Ba_{2-x}Cu_3O_{7-\delta}$ shows a monotonic decrease in T_c with x , except for the range 0 – 0.05 where T_c shows a

plateau, as seen in Figure IV.5 [13]. In the range around $x \sim 0$, the excess Nd^{3+} provides excess electrons, thus, inducing hole-deficiency in the system.

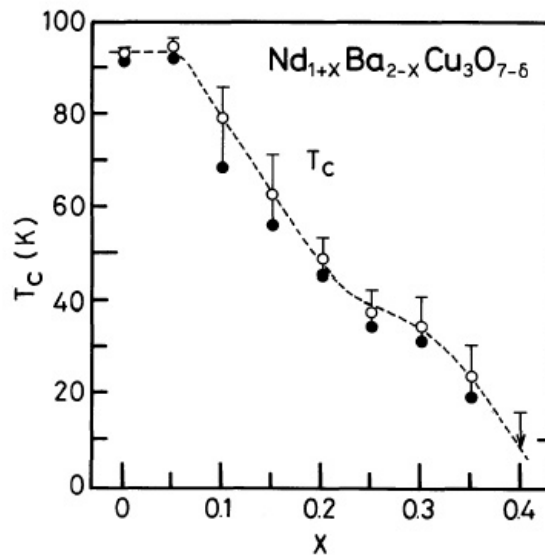


Figure IV.5 Excess Nd dependence (x) of T_c in $\text{Nd}_{1+x}\text{Ba}_{2-x}\text{Cu}_3\text{O}_{7-\delta}$ (K. Takita *et al.* Ref. [13]).

In summary, the charge carrier (hole) density in $\text{YBa}_2\text{Cu}_3\text{O}_{7-\delta}$ becomes smaller as the oxygen deficiency δ increases and becomes zero at $\delta > \sim 0.6$. Ca^{2+} substitution for Y^{3+} can induce excess hole carriers (over-doping), while excess RE ions in $(\text{RE})_{1+x}\text{Ba}_{2-x}\text{Cu}_3\text{O}_{7-\delta}$ compounds deplete the hole carrier density (under-doping) by substituting Ba^{2+} with electron-donating RE^{3+} ions.

In oxygen stoichiometric $\text{La}_{2-x}\text{Sr}_x\text{CuO}_4$, it is clearly found that there is an one-to-one correspondence between the Sr content x and the hole concentration in the CuO_2 plane, $[\text{Cu-O}]^+$ [14]. T_c appears to be maximized at $[\text{Cu-O}]^+ \sim 0.16$ and falls to zero on both the

underdoped and the overdoped sides at $[\text{Cu-O}]^+ \sim 0.05$ and ~ 0.27 respectively. The variation of T_c is conveniently represented by one curve [15],

$$T_c / T_{c,\text{max}} = 1 - 82.6 ([\text{Cu-O}]^+ - 0.16)^2$$

It is found that oxygen off-stoichiometric YBCO also follows this same relationship, as shown in Figure IV.6 [10], although with the difference that there is more than one way to modify the hole density in YBCO. Indeed, YBCO satisfies the universal relation between hole density and $T_c/T_{c,\text{max}}$, no matter if the hole density variation is induced by oxygen deficiency, partial Ca substitution, or excess RE substitution. Thus, it is necessary to maintain optimal hole concentration $[\text{Cu-O}]^+$ (~ 0.167) in the system to achieve maximum T_c .

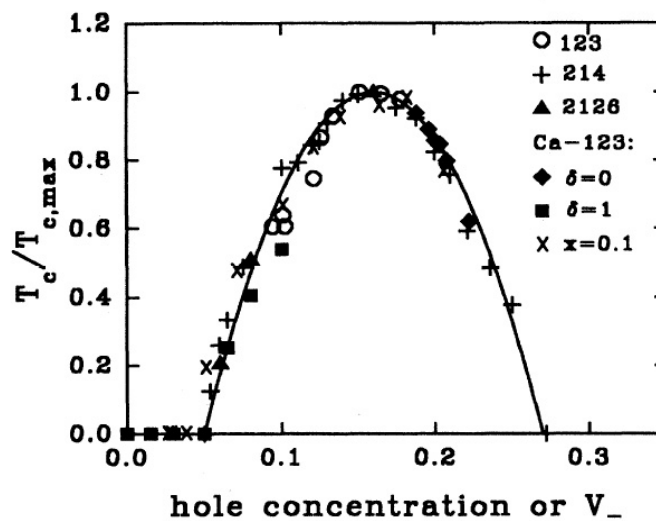


Figure IV.6 T_c normalized to $T_{c,\text{max}}$ plotted as a function of hole concentration, (i) from $\text{Y}_{1-x}\text{Ca}_x\text{Ba}_2\text{Cu}_3\text{O}_6$ (solid squares), (ii) from $\text{YBa}_2\text{Cu}_3\text{O}_{7-\delta}$ with different δ (open circles), (iii) from $\text{Y}_{1-x}\text{Ca}_x\text{Ba}_2\text{Cu}_3\text{O}_{7-\delta}$ with $\delta \sim 0.04$ and different x (solid diamonds), and (vi) from $\text{Y}_{1-x}\text{Ca}_x\text{Ba}_2\text{Cu}_3\text{O}_{7-\delta}$ with $x \sim 0.1$ and different δ (crosses). Data taken from Fig.2. of J.L. Tallon *et al.* (Ref. [10]).

IV.1.2 Charge carrier doping at YBCO grain boundaries

Low angle grain boundaries are composed of an array of alternating superconducting channels and non-superconducting (or under-doped) GB dislocation cores, as described in more detail in Chapter I and III. The non-stoichiometry and strain (lattice distortion) around GB dislocation cores reduce hole density and modify electronic structure within a few nm of the GB cores. Indeed, carrier-depletion layers were experimentally observed by electron energy loss spectroscopy (EELS) [16,17]. Therefore, it should be possible to enhance the GB transparency by hole-doping, either by Ca substitution [2], oxygen annealing [3], or by RE substitution, as discussed in section IV.1.1 on the doping state of YBCO grains. The beneficial effects on $J_{c,gb}$ of grain boundary of doping by partial substitution of Ca^{2+} for Y^{3+} in $\text{YBa}_2\text{Cu}_3\text{O}_{7-\delta}$ were first demonstrated by the Augsburg group, especially for 24° and 36° high angle grain boundaries [2,4]. An optimum replacement of Y by substitution of 30% Ca at 4.2 K (to make the composition $\text{Y}_{0.7}\text{Ca}_{0.3}\text{Ba}_2\text{Cu}_3\text{O}_{7-x}$) was determined for high angle grain boundaries (mainly 24° [001] tilt), as shown in Figure IV.7. Shortly afterwards, work in our group showed that $J_{c,gb}$ for 5° [001] tilt grain boundaries could be significantly improved by 30% Ca doping as well [3]. However, Ca doping is importunately accompanied by a substantial decrease in T_c due to over-doping of the YBCO grains, even though it improves the GB properties. Thus the improvement at higher temperatures where applications are most desirable is relative only, not absolute.

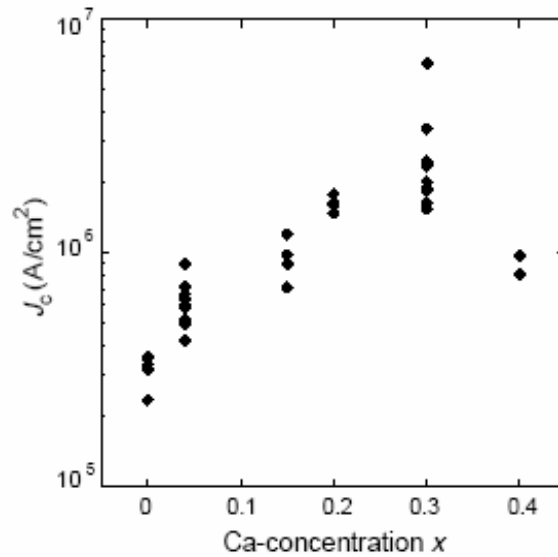


Figure IV.7 Dependence of J_c of symmetric 24° [001]-tilt grain boundaries in $Y_{1-x}Ca_xBa_2Cu_3O_{7-\delta}$ films on the Ca concentration x at 4.2 K (A. Schemehl, J. Mannhart, and *et al.* Ref. [2]). The 30% Ca doping exhibits the best $J_{c,gb}$ at 4.2 K.

There has been some effort to better understand how Ca-doping influences the intergrain $J_{c,gb}$ of $Y_{1-x}Ca_xBa_2Cu_3O_{7-\delta}$. Significant reduction of the excess charge at the grain boundary was indeed revealed by electron holography of 4° [001]-tilt pure and 30% Ca-doped YBCO bicrystals for which the negative GB potential was smaller (-1 V vs. -2.4 V) and decayed over a shorter length (0.8 nm vs. 1.7 nm) for the Ca-doped GB [18]. Klie *et al.* [19] reported the highly strained grain boundary regions contain excess oxygen vacancies, which reduce the hole concentration at the boundary. They claimed agreement between Z-contrast scanning transmission electron microscopy (STEM) images, electron energy loss spectra (EELS), and density functional theory (DFT) calculations, concluding that excess holes introduced by Ca^{2+} substitution for Y^{3+} do not very much improve GB properties. By DFT bond energy modeling (see the results in Fig. IV.8), they concluded that

Ca^{2+} ions can replace Y^{3+} in intra-grain $\text{Y}(\text{Ca})\text{BCO}$ much as foreseen, but that they also tend to replace large Ba^{2+} ions in the compressed regions of dislocation cores, and the smaller Cu^{2+} ions in the tensile regions of the dislocation cores. Thus, the Ca^{2+} substitutions relieve GB strain and suppress O vacancy formation. They suggested that dopants should be selected for their size, more than just for their valence, proposing Eu and Ag as good candidates. The interesting picture that emerges from these studies is that there are strong driving forces for segregation to $[001]$ tilt grain boundaries that may enable the amelioration of grain boundary properties without incurring the marked depression of T_c that occurs by Ca addition. If this indeed can be engineered, then grain boundary alloying becomes a much more attractive means of enhancing the transport current $J_{c,gb}$ across GBs. This speculation, also pursued independently in our laboratory, was the motivation for the present study in this chapter.

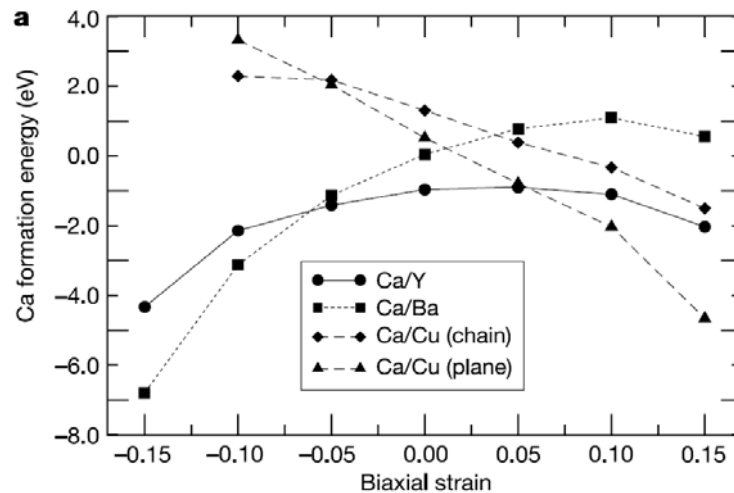


Figure IV.8 DFT calculations of the energy required to substitute Ca on different lattice sites in YBCO as a function of biaxial strain. It can be energetically favorable for Ca to replace Y, Ba, or Cu, depending on the local strain (R.F. Klie *et al.* Ref. [19]).

In fact, work on Ca-doped grain boundaries within our group proceeded in parallel with the above research work. X. Song *et al.* [5] investigated the lattice structure, electronic state and current transport of pure and Ca-doped GBs in low-angle YBCO bicrystals by combining measurements of the extended voltage-current characteristics on a matched pair of 30% Ca-doped and pure 7° [001]-tilt YBCO bicrystals with detailed atomic-scale microscopy of exactly the same grain boundaries. Most unexpectedly they found that Ca-doped grain boundaries had greatly expanded dislocation cores which narrowed the “undisturbed” channel between the dislocations. A very significant Ca segregation (50% enhancement) at the GB and a strong non-monotonic variation of Ca concentration along the GB plane and across the dislocation cores was observed. This segregation occurred on scales ~ 1 nm that matched the core-channel structure of the grain boundary. In spite of a clearly observed expansion of the dislocation cores normal to and parallel to the grain boundary and the shrinking of the channel, surprisingly $J_{c,gb}$ increased close to the critical current density in the grains. To explain this behavior, A. Gurevich [5] proposed a cation segregation model in which Cottrell atmospheres of Ca ions form under the combined strain and electric fields of the dislocations making up a low angle grain boundary. The predictions of this cation segregation model will be used to interpret the transport characteristics of each system investigated later. The model predicts a highly inhomogeneous Ca concentration $c(x,y)$ both along and across the grain boundary, as shown in Figure IV.9. The equilibrium concentration $c(x,y)$ of Ca in *the pressure field* $p(x,y)$ and the *screened electric potential* $\phi(\mathbf{r})$ produced by the GB dislocation is given by;

$$c = \frac{c_0}{c_0 + (1 - c_0) \exp[(p\Delta V + \phi\Delta Z) / k_B T]} \quad (\text{IV.1})$$

Here $\Delta V = V_{\text{Ca}} - V_{\text{Y}}$ and $\Delta Z = Z_{\text{Ca}} - Z_{\text{Y}}$ are the differences of ionic volume and charge of the Ca and substituted Y, and c_0 is the bulk concentration, $p(x,y) = p_0 \sin(2\pi y/d) / [\cosh(2\pi\rho/d) - \cos(2\pi y/d)]$, $d = b/2\sin(\theta/2)$, $p_0 = \mu \sin(\theta/2) / (1-\nu)$, $\rho = (r_0^2 + x^2)^{1/2}$, the cut-off radius $r_0 \sim b$ accounts for the plastically deformed dislocation core, μ is the shear modulus, ν is the Poisson ratio, and x and y are coordinates across and along the GB, respectively. The Ca concentration $c(x,y)$ plotted in Figure IV.9 exhibits peaks in tensile regions, followed by pronounced dips in compressed regions along the GB, and a non-monotonic dependence of $c(x)$ perpendicular to the GB. Equation IV.1 also shows that the periodic stress $p(y)$ tends to increase the average Ca concentration at the GB, $\langle c \rangle = \int^L c(x,y) dy / L$ where $L \gg d$. For $p_0 \Delta V / k_B T \ll 1$, $\phi = 0$, and $c_0 \ll 1$, then $\langle c(x,y) \rangle = c_0 \langle \exp[-\Delta V p(x,y) / k_B T] \rangle \sim c_0 (1 + \Delta V^2 \langle p^2 \rangle / 2 k_B^2 T^2) > c_0$, where $\langle p \rangle = 0$, and $\langle p^2 \rangle = 2p_0^2 / [\exp(4\pi\rho/d) - 1]$. Taking $\nu = 0.3$, $\mu = 40$ GPa, $\theta = 7^\circ$, $\Delta V = V_{\text{Ca}} - V_{\text{Y}} = 4p(r_{\text{Ca}}^3 - r_{\text{Y}}^3) / 3$, where r_{Ca} and r_{Y} are the ionic radii of Ca and Y, and $T = 300$ K, this estimates $p_0 \Delta V / k_B T_i \sim 0.85$. Thus, the GB dislocation strains favor segregation of Ca in order to partially offset the electrostatic barrier caused by the negative $\phi(x)$ of a hole-deficient GB. For $Z_{\text{Ca}} < Z_{\text{Y}}$, the competition between strain and electric-field effects causes minima in $c(x)$, as shown Figure VI.9. $\phi(x,y) = \phi_0 \sum_n K_0 (r_0^2 + x^2 + (y - nd)^2)^{1/2} / l_D / K_0 (r_0 / l_D)$, is a solution of the Thomas-

Fermi equation $\nabla^2\phi - \phi/l_D^2 = -4\pi q \sum_n f(x, y - dn)/\epsilon$ that describes the screened potential of charged dislocation cores spaced by d along the y axis. Here $\phi_0 = 2q/\epsilon$ is the amplitude of the electric potential produced by the line charge q per unit length of the core, $f(r)$ is a function that describes the radial distribution of charge density in a region of radius $\sim r_0 \ll d$, $\int f(x, y) dx dy = 1$, and $K_0(x)$ is a modified Bessel function. These detailed expressions for $p(x, y)$ and $\phi(r)$ were indicated in Ref. [5], and repeated here.

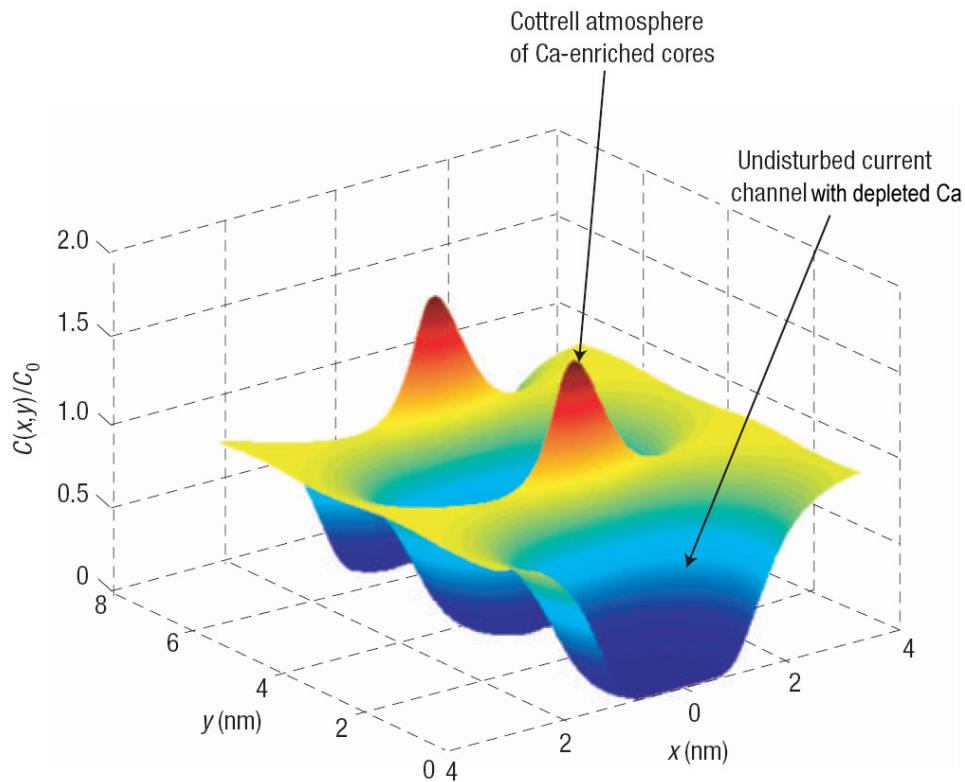


Figure IV.9 Ca distribution around the GB dislocations is calculated from the charge-strain model in X. Song *et al.* Ref. [5]. Surface plot of the distribution of Ca²⁺ solute ion near a periodic chain of edge dislocations in a 7° GB calculated from Eq. IV.1. The strong non-monotonic Ca segregation at the dislocation cores is expected, as is the depleted Ca ion with respect to the grains in the channel [5].

One of the principal virtues of the model is that it suggests new possibilities for manipulating the properties of doped GBs. Comparison of the model to the compositional measurements shows that the model indeed captures the measured Ca distribution, as shown in Fig. IV.10, including the very significant enhancement of Ca in the tensile parts of the dislocation core which produces the core expansion, followed by Ca depletion in the compressed parts, as well as a non-monotonic distribution of Ca perpendicular to the grain boundary because of the strong electrostatic barrier at the grain boundary. Indeed, the cation segregation model works very well, encouraging its further use for exploring ways of engineering doping of YBCO GBs.

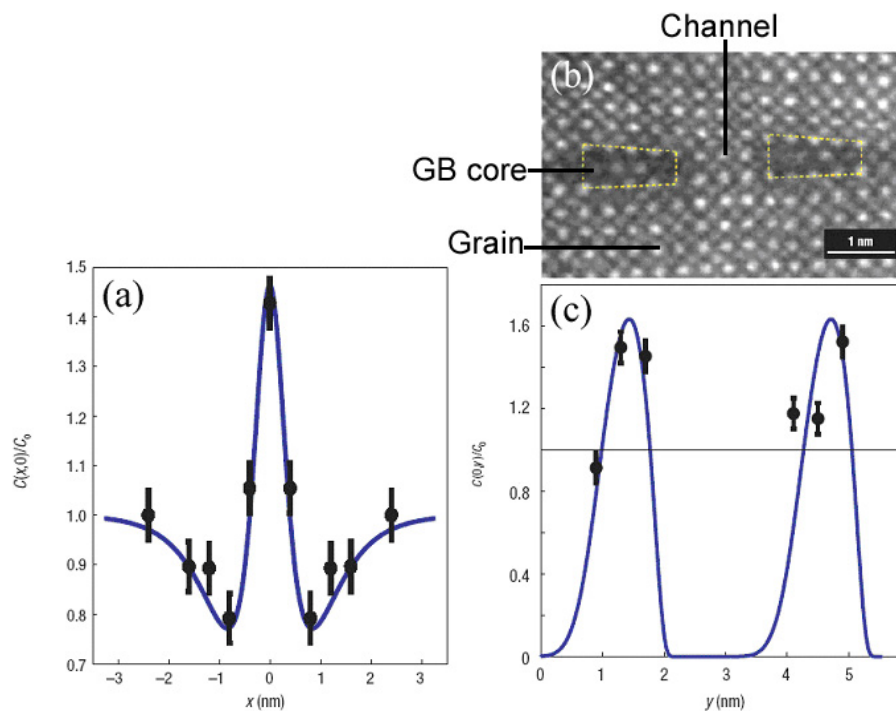


Figure IV.10. (a) Ca distribution across the GB (b) Expanded dislocation cores in the Ca-doped GB (CB core, channel, and grain are indicated), and (c) Ca distribution along GB (bottom). Solid lines show the model calculation (X. Song *et al.* ref [5]).

IV.2 Flux Flow Behavior at Grain Boundaries

Low angle grain boundaries in high temperature superconductors exhibit hybrid properties between Abrikosov and Josephson vortices (AJ vortices), whose length along the GB is smaller than the London penetration depth λ , but larger than the coherence length ξ [20-22]. The larger core of AJ vortices leads to weaker pinning by the dislocation cores in the GB and induces preferential flux-flow of the GB vortices, resulting in non-linear voltage-current characteristics and flux-flow resistivity (seen as linear region in the V-I characteristics) [3,23-25]. The signature characteristic of the GB flux flow is often an Ohmic onset of resistance at low currents, which transitions to non-Ohmic intra-grain flux flow at higher currents.

The core sizes of AJ vortices and the local grain boundary depairing current density can be deduced by measuring the flux flow resistance $R_F(H)$ of the GB in a bicrystal as a function of applied magnetic field [26]. The flux flow resistance for AJ vortices has the form

$$R_F(H) = \frac{R_n \sqrt{H}}{\sqrt{H + H_0}}, \quad H_0 = \frac{\phi_0}{4\pi^2 l^2}, \quad l = \frac{c\phi_0}{16\pi^2 \lambda^2 J_{d,gb}} \quad (\text{IV.2})$$

where ϕ_0 is the magnetic flux quantum, λ is the bulk London penetration depth, c is the speed of light. The AJ vortex core length along GB, l , is defined by the field H_0 at which the flux flow resistance $R_F(H)$ saturated. This saturation occurs at H_0 because H_0 is the field at which the vortex cores first overlap. Then, in fact, $J_{d,gb}$, the depairing current density of the GB, can be extracted from the l calculation [26].

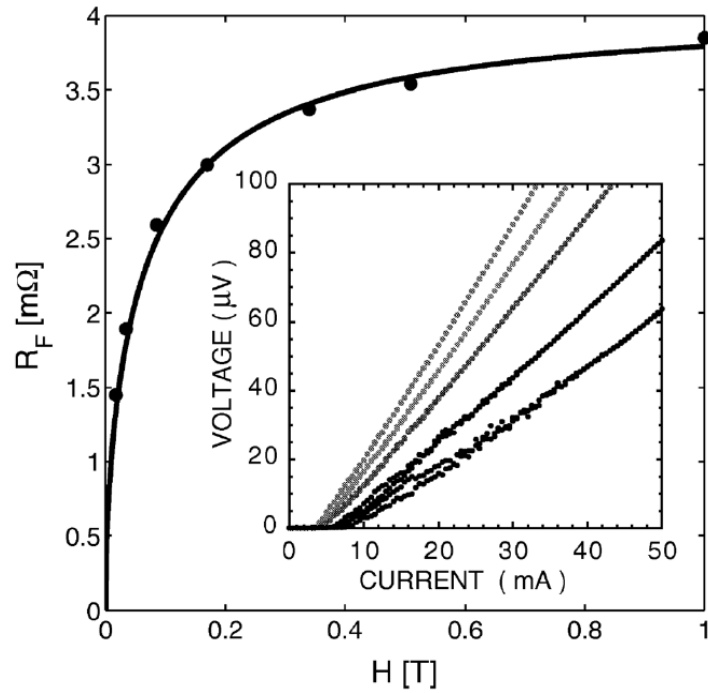


Figure IV.11 $R_F(H)$ data extracted from the slope of the $V(J,H)$ curves at 77 K for a 7° bicrystal. The solid curves are described by Eq. (IV.2) with $R = 4.05 \text{ m}\Omega$ and $H_0 = 0.14 \text{ T}$. The inset shows V - J curves for 0.17, 0.51, 0.85, 1.7 and 3.4 kOe (from bottom to top, respectively) [26].

Figure IV.11 shows data taken on a 7° [001]-tilt PLD-grown YBCO bicrystal grain boundary with curves fit to $R=4.05 \text{ m}\Omega$ and $H_0 = 0.14 \text{ T}$, from which $l = (\phi_0/H_0)^{1/2}/2\pi = 19 \text{ nm}$ at 77K [26]. Thus vortices on this 7° grain boundary are indeed AJ vortices with phase cores much larger than the intra-grain coherence length $\xi \sim 4 \text{ nm}$ but much smaller than $\lambda \sim 400 \text{ nm}$ [26].

IV.3 Ca-doping in low angle YBCO grain boundaries

The first experiment was made to investigate the influence on GB transparency of systematic changes in Ca content x using a set of $Y_{1-x}Ca_xBa_2Cu_3O_{7-\delta}$ bicrystal films. Judged by the number of earlier experimental studies on high angle grain boundaries [2], it was generally believed that 30% Ca is the optimum doping level for improvement of grain boundary transparency. However, the segregation model [5] predicts that the optimum concentration should depend on the misorientation angle. Therefore, lower levels of Ca substitution were explored for the lower angle ($6-9^\circ$) grain boundaries typically found in CCs.

$Y_{1-x}Ca_xBa_2Cu_3O_{7-\delta}$ ($x=0, 0.10, 0.15, \text{ and } 0.30$) films were deposited on single crystal $SrTiO_3$ (STO) substrates, and 7 or 9° symmetric bicrystal STO substrates by pulsed laser deposition (PLD). The bicrystal experiment is expensive since each 10×10 mm² substrate costs \sim \$600. However, it is much simpler to get a single grain boundary with a specific angle. Meaningful comparison of properties from one concentration to another requires an extensive substrate set with identical misorientation properties, a condition that can only be provided by bicrystal substrates cut from a single bicrystal. Substrate temperature was set at $800-810^\circ\text{C}$, while oxygen pressure was set at 200 mTorr during growth. 7000 pulses at 5 Hz were used to deposit ~ 500 nm thick films

(Figure IV.12). The films were post oxygen annealed at 475-500 °C for two hours in the indicated oxygen pressures in Table IV.1. The oxygen pressure was determined to achieve the highest T_c for each Ca content [27]. After T_c and $J_c(H,T)$ measurement, some samples were further oxygenated at 800 Torr to establish the fully oxygenated (i.e. overdoped) state, compared with the sample annealed for the highest T_c . Bridges were cut by 40 μm (width) \times 1000 μm (length) for all films for detailed transport measurement. Films were measured at the same reduced temperature t ($t=T_{\text{measurement}}/T_c$) of 0.85 for comparison, since the T_c varies according to Ca content and oxygen annealing condition.

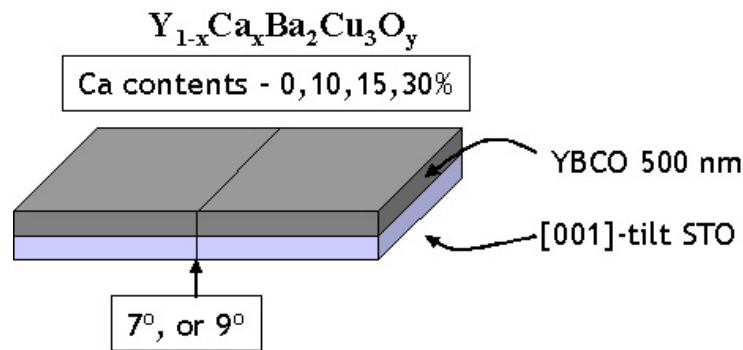


Figure IV.12 Illustration of the bicrystal experiment.

Table IV.1 Summary of T_c of each sample and its annealing condition for maximum T_c .

Ca contents	0%	10%	15%	30%
O₂ annealing condition	800 Torr	200 Torr	15 Torr	15 Torr
Intragrain	90.2K	80.1K	81.6K	84.0K
7° GB	87.6K	77.1K	81.1K	83.6K
9° GB	88.3K	79.3K	82.5K	84.6K

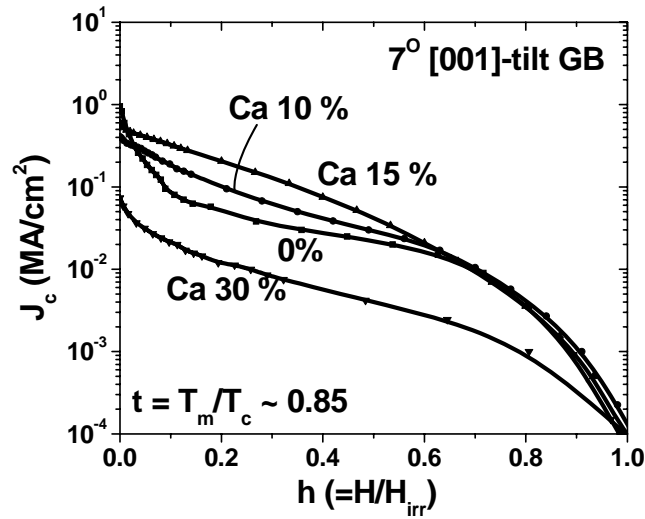


Figure IV.13 The reduced $J_c(h)$ of $Y_{1-x}Ca_xBa_2Cu_3O_{7-\delta}$ ($x=0, 0.10, 0.15,$ and 0.30) for 7° [001]-tilt grain boundary. The samples were annealed for the maximum T_c (see Table IV.1). The $J_c(h)$ was measured at the same reduced temperature of ~ 0.85 for comparison. 10% and 15% substitution shows increase in J_c in intermediate fields, while 30% Ca substitution exhibits substantial J_c reduction in the entire field range.

Figure IV.13 shows the reduced $J_c(h=H/H_{irr})$ of $Y_{1-x}Ca_xBa_2Cu_3O_{7-\delta}$ ($x=0, 0.10, 0.15,$ and 0.30) for 7° [001]-tilt grain boundary at the same reduced temperature $t = T_m/T_c$ of ~ 0.85 for the samples annealed for the maximum T_c (Table IV.1). The 30% Ca substitution exhibits no improvement of $J_{c,gb}$ over entire field range up to H_{irr} (it has even smaller $J_{c,gb}$ than that of the pure YBCO), while the 10% and 15% Ca substitutions show significant enhancements of $J_{c,gb}$ in intermediate fields. The data clearly indicate the improvement of grain boundary $J_{c,gb}$ at intermediate fields for an intermediate Ca doping, with 15% being the best. However, $J_{c,gb}$ was reduced at low fields for all Ca substitution, a point relevant to changes in intra-grain vortex pinning produced by Ca substitutions.

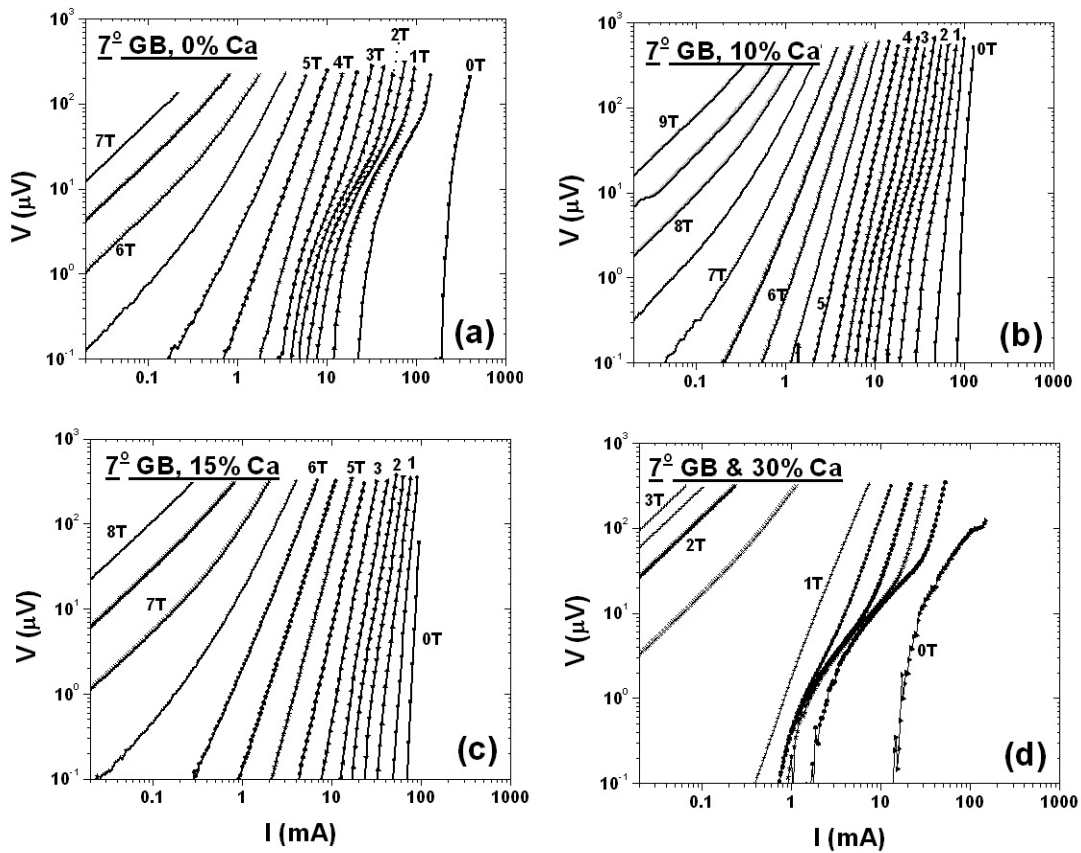


Figure IV.14 V-I curves of $Y_{1-x}Ca_xBa_2Cu_3O_{7-\delta}$ for x of (a) 0, (b) 0.10, (c) 0.15, and (d) 0.30 for 7° grain boundary. The films were annealed for the maximum T_c (see Table IV.1). (a) and (d) shows usual GB-signature which appears as a knee-shape of the curves (i.e. GB dissipation signature of flux flow behavior). However, the GB-signature significantly reduced for the 10 and 15% Ca-doped YBCO (b)(c).

Figure IV.14 shows the corresponding V-I characteristics for $J_c(h)$. The pure YBCO 7° grain boundary shows a typical grain boundary kink in the V-I characteristics. However, the grain boundary kink in the V-I characteristics becomes weaker at 10% Ca doping, and almost disappears at 15% Ca doping. This result agrees with the $J_c(h)$ results in Fig. IV.13,

which exhibit $J_{c,gb}$ improvement for 10% and 15% Ca-doping at intermediate fields. This loss/reduction of the grain boundary signature indicates that the critical current is no longer limited by grain boundaries, but becomes limited by intra-grain pinning. This interesting feature indicates the possibility of totally removing grain boundary limitation in coated conductors. By contrast, 30% doping of the 7° GB degrades the GB properties.

However, the low-field J_c reduction produced by added Ca remains a concern, and may be due to an intrinsic effect of Ca in YBCO. Figure IV.15 exhibits $J_c(H)$ in the intragrain region of Ca-doped YBCO. The J_c reduction is seen for 10% and 15% Ca-doped samples at fields less than 1T. Otherwise, the $J_c(H)$ curves overlap pretty well at fields greater than 1T (or a reduced field h of ~ 0.1) even though there is slight variation of the irreversibility field, while the 30% Ca doping exhibits a dramatic reduction in H_{irr} . Figure IV.16 shows two-axes XRD scans around [103] for Ca-doped YBCO grains. The Ca substitution significantly reduces the orthorhombicity of the YBCO lattice. (10% Ca shows the least orthorhombicity and also exhibits the smallest J_c at low fields.) Smaller orthorhombicity will reduce the twin density and very low angle GB dislocation density, and is likely cause of the reduced J_c at low fields. But as will be discussed further in Chapter V, native defects like dislocations and twins are not the strong pinning centers capable of optimizing pinning in YBCO. For this insulating precipitates like Y_2O_3 , $BaZrO_3$, or Y_2BaCuO_5 are optimum. Thus, lowering of the orthorhombicity does not invalidate Ca-doping as an approach to ameliorating the GB properties, since nanoparticle intra-grain pinning can be used to enhance pinning in the grain [28,29].

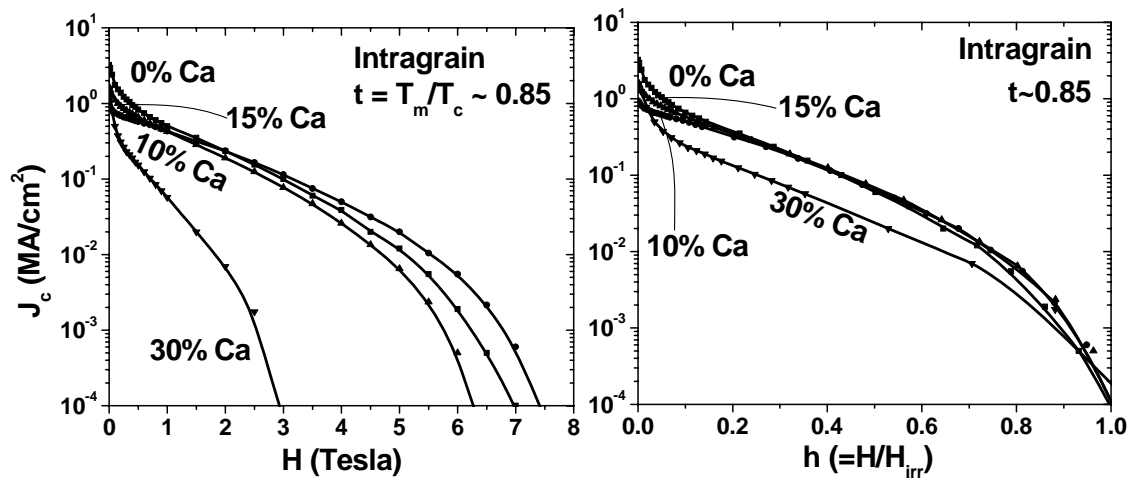


Figure IV.15 $J_c(H)$ (left) and reduced $J_c(h)$ (right) of grain of Ca-doped YBCO. Except for 30% Ca, the curves overlap pretty well at fields greater than 1T (or a reduced field h of ~ 0.1) even though there is slight variation of the irreversibility field. The 30% Ca doping exhibits a dramatic reduction in H_{irr} .

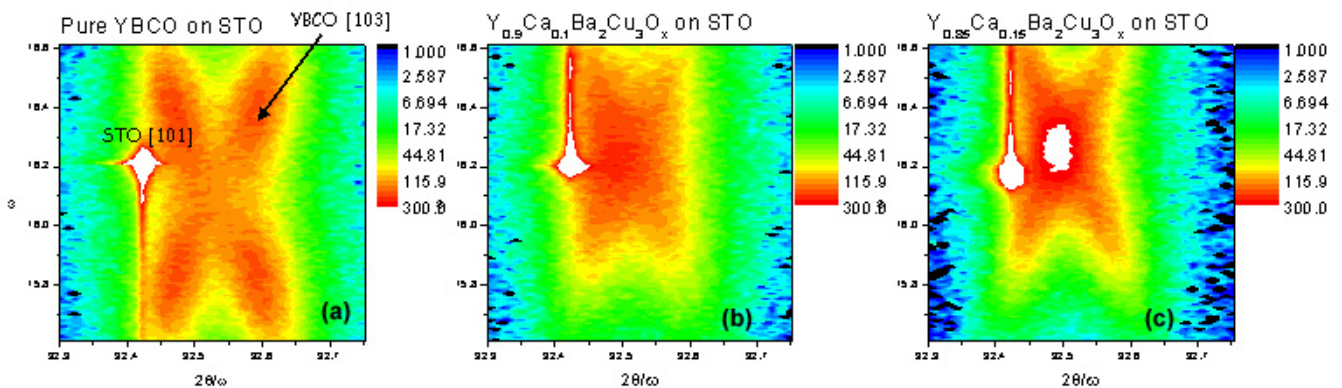


Figure IV.16 Two Axes Scans (ω - $\omega/2\theta$ scans) near [101] STO and [103] YBCO space for (a) pure YBCO, (b) 10% Ca-, and (c) 30% Ca-doped YBCO are shown. Pure YBCO indicates a distinctive orthorhombicity, while the orthorhombicity reduces as Ca added.

The enhancement of the $J_{c,gb}$ by 10% and 15% Ca-doping can be interpreted using the prediction from the cation segregation model. The Ca distributions near the grain boundary cores for each Ca content were calculated for 7° GBs from the cation segregation model, and the results are plotted in Figure IV.17. The same parameters used in the Ref. [5] were adapted for the calculations while only the Ca doping level is modified. Since the 15% Ca-doped GB exhibited no GB signature in V-I characteristics, the segregation occurring at 15% doping level (Fig. IV.17(b)) can be considered as optimum. The Ca concentration at the 15% Ca-doped GB core is around twice the doping level (i.e. $\sim 25 - 30\%$). For 10% Ca-doped GB, which exhibited a reduced GB signature, the segregation seems to be insufficient for optimum doping at the GB. The 30% doping may have induced too large segregation, resulting in overdoping at the GB core. The bottom illustrations in Figure IV.17 represent the expected vortex array near the GB cores. A round vortex corresponds to an Abrikosov vortex, while an ellipsoidal vortex corresponds to an Abrikosov-Josephson hybrid vortex. As shown in the $J_c(h)$ and V-I characteristics, the 15% Ca doped GB only shows behavior of Abrikosov vortices, leading us to conclude that the J_c across the GB is limited now only by intragrain pinning and not by the GB.

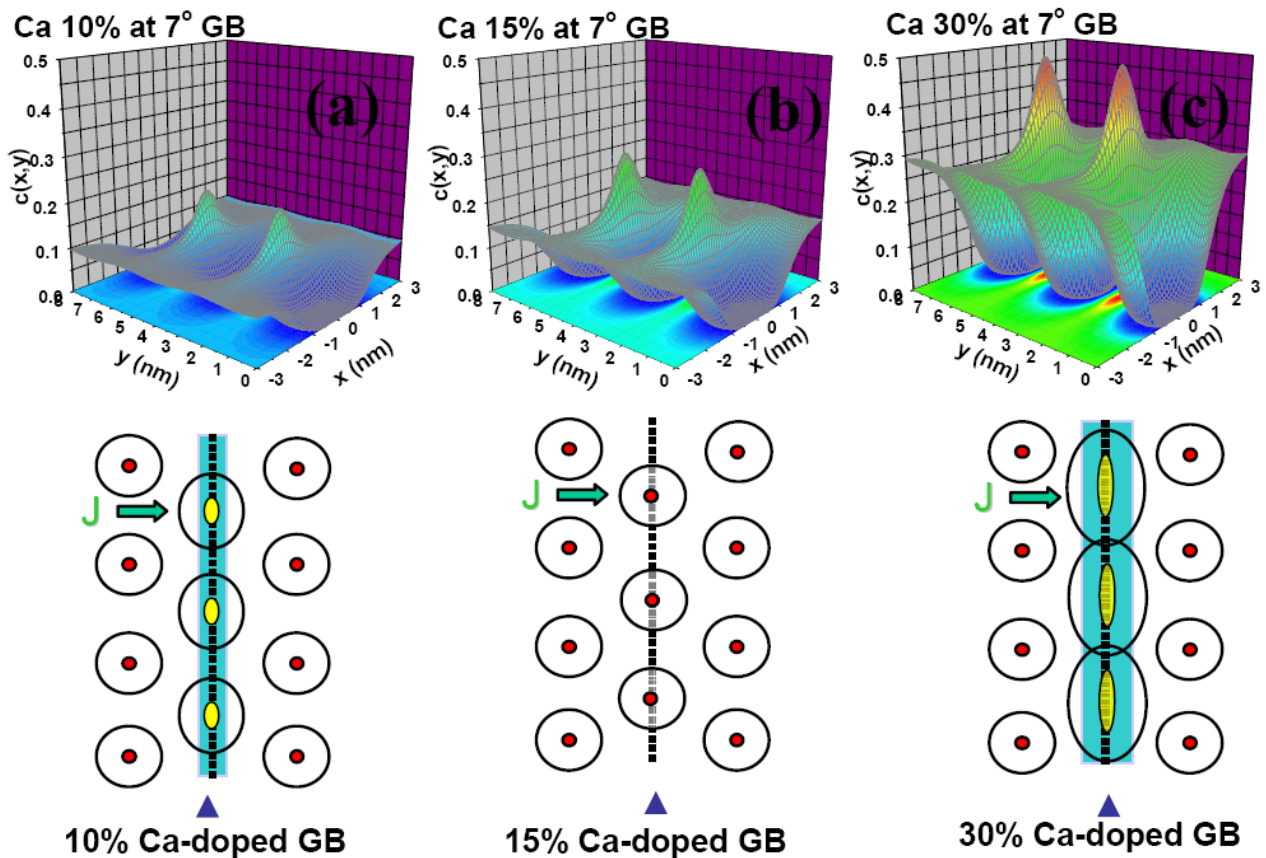


Figure IV.17 The calculated Ca distribution near the grain boundary cores from the cation segregation model of A. Gurevich [5] are shown for (a) 10%, (b) 15%, and (c) 30% Ca doped samples. The same parameters used in the ref [5] was adapted for the calculations while only the Ca doping level is modified. The bottom illustration represents the expected vortex array near and along the GB. The round vortices correspond to Abrikosov vortices, while the ellipsoidal vortices correspond to the Abrikosov-Josephson hybrid vortices.

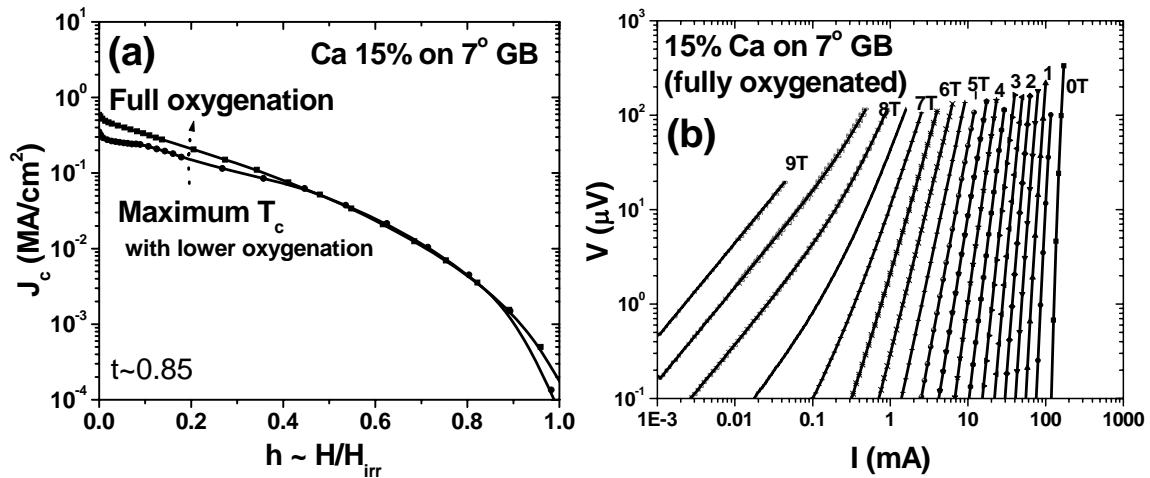


Figure IV.18 (a) Reduced $J_c(h)$ for 7° [001]-tilt GB for 15% for sample of two different oxygenation state (for maximum T_c and fully oxygenated). The sample was oxygenated in 15 Torr O_2 for maximum T_c or in 800 Torr O_2 for the fully oxygenated state. The magnitude of J_c further was enhanced by the full oxygenation. The magnitude of J_c was further enhanced by full oxygenation. (b) V-I curves across the 15% Ca-doped YBCO 7° GB for fully oxygenated state. No GB dissipation signature is observed. The detailed shape of these curves can be compared to Figure IV.14(c), which is the V-I curves across the 15% Ca-doped YBCO 7° GB maximum T_c state.

Figure IV.18(a) shows the reduced $J_c(h)$ for the 7° [001]-tilt GB, 15% Ca doped, fully oxygenated state (annealed at 800 Torr), comparing its properties with $J_c(h)$ in the maximum T_c state (annealed at 15 Torr). The magnitude of J_c was further enhanced by the full oxygenation. The V-I characteristics of the 15% Ca-doped sample (Fig. IV.18(b)) do not exhibit any GB-dissipation signature. Careful comparison to Figure IV.14(c) suggests that a very small GB signature was present at low fields in the highest T_c states. Thus oxygen changes back over doping indeed benefits the transparency of the GB by adding additional carriers.

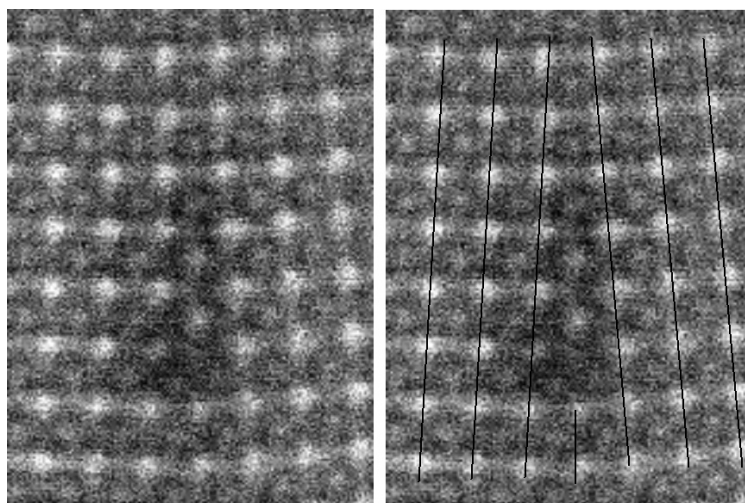


Figure IV.19 Z-contrast image of the 7° [001] tilt 15% Ca-doped YBCO grain boundary. Overlaid straight lines (right) imply that there is no lattice distortion. (images by Dr. Yan Xin, NHMFL)

Preliminary Z-contrast STEM analysis reveals the strain relief produced by Ca around the GBs explicitly. Figure IV.19 shows the Z-contrast image of the the 15% Ca-doped 7° GB, taken by Dr. Yan Xin. The bright columns represent Y/Ba/(Ca) columns, while the dark columns are Cu/O columns. In contrast to a pure YBCO GB, no lattice distortion around the GB dislocation was observed. The core expansion produced by Ca segregation at the core removes the lattice distortion. (Typically, there is large lattice distortion around GB cores in pure YBCO GB [5].) However, compositional mapping by electron energy loss spectroscopy on this grain boundary core structure has not yet made. Further analytical transmission electron microscopy to provide essential Ca distributions around GB cores is planned for this sample and some other samples studied here.

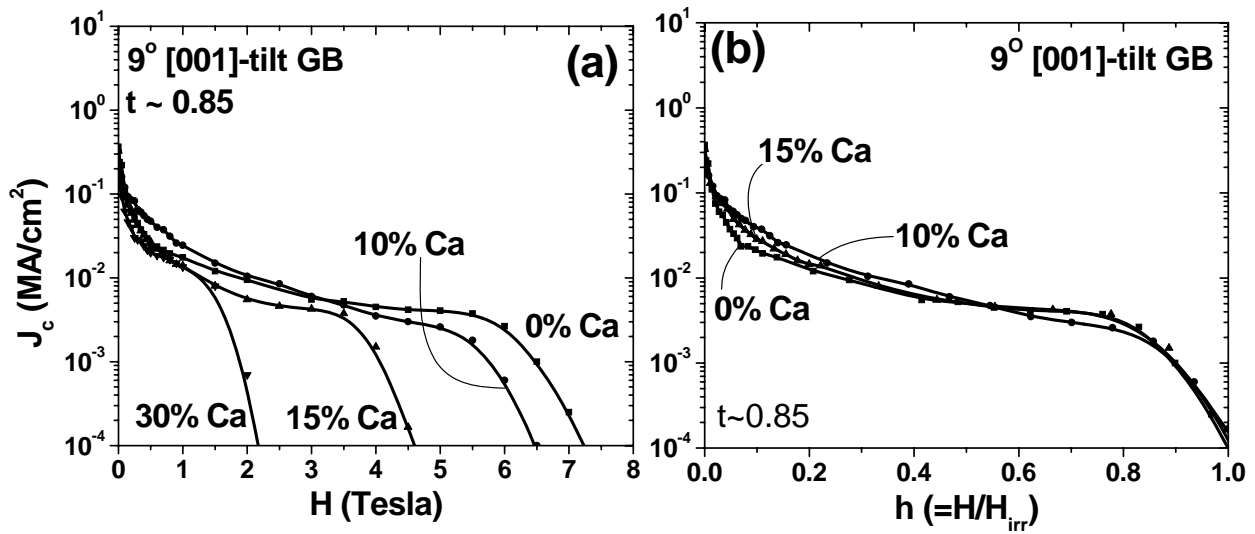


Figure IV.20 (a) $J_c(H)$ and (b) the reduced $J_c(h)$ of $Y_{1-x}Ca_xBa_2Cu_3O_{7-\delta}$ ($x=0, 0.10, 0.15,$ and 0.30) for 9° [001]-tilt grain boundary. The $J_c(h)$ is measured at the same reduced temperature of ~ 0.85 for comparison.

Figure IV.20 shows $J_c(H)$ and the reduced $J_c(h=H/H_{irr})$ of $Y_{1-x}Ca_xBa_2Cu_3O_{7-\delta}$ ($x=0, 0.10, 0.15,$ and 0.30) for 9° [001] tilt grain boundaries at a reduced temperature of ~ 0.85 . These samples were oxygen-annealed for maximum T_c . First of all, 30% Ca doping produces a dramatic reduction of irreversibility field H_{irr} from ~ 7 T of pure YBCO to ~ 2 T (Fig. IV.20(a)). The 10% Ca doping shows the best $J_c(h)$ behavior, although the different Ca levels actually are not very different. In the V-I curves for the 9° grain boundaries shown in Figure IV.21, no weakening of GB signature was observed with addition of Ca. There is thus a marked difference between 7° and 9° .

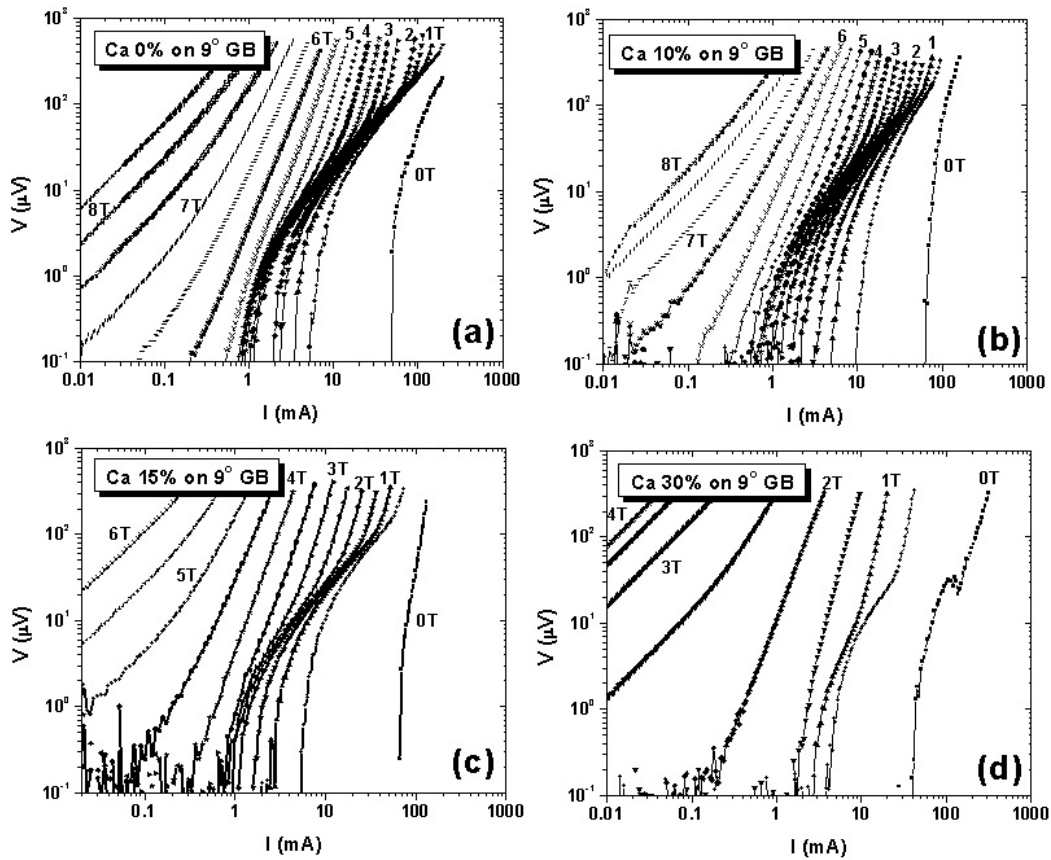


Figure IV.21 V-I curves of $Y_{1-x}Ca_xBa_2Cu_3O_{7-\delta}$ for x of (a) 0, (b) 0.10, (c) 0.15, and (d) 0.30 for 9° grain boundary. All V-I curves exhibit GB-dissipation signatures.

Because the GB dissipation signature was always present, it was possible to calculate the core size l of AJ vortices (along the GB) on these variously Ca-doped 9° grain boundaries. Figure IV.22 shows the linear V-I curves of a 9° GB for pure and Ca-doped YBCO, which exhibit clear flux flow behavior at low fields and at low voltage level. These flux flow resistances $R_F(H)$ [26] were calculated and plotted in Figure IV.23. For pure YBCO, the AJ vortex core size was calculated as 39 nm from equation (IV.2), which shows

that the AJ vortex size is much larger than $\xi \sim 4$ nm but much smaller than $\lambda \sim 400$ nm [26]. Indeed it was found that the Ca addition reduced the core sizes to 23, 27, and 32 nm for 10%, 15%, and 30% Ca, respectively, compared to that of pure YBCO 9° GB (see Table IV.2). Here, the AJ vortex core size for 10% Ca-doped YBCO on 9° GB was the smallest and indeed this GB showed the best $J_{c,gb}$. This proves that Ca-doping does reduce the core size of the AJ vortices, enhancing of $J_{d,gb}$, by providing stronger pinning of AJ vortices.

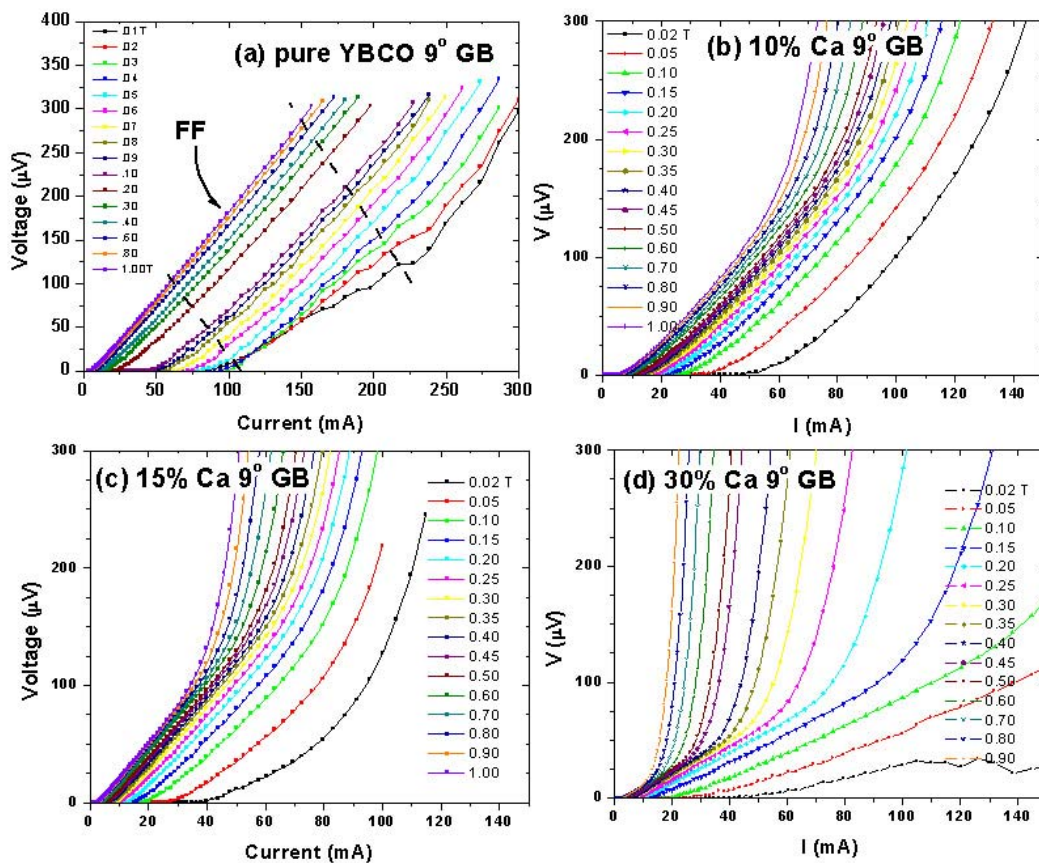


Figure IV.22 V-I curves (on linear axes) in linear-linear plot across a 9° grain boundary of (a) pure YBCO, (b) 10% Ca-doped YBCO, (c) 15% Ca-doped YBCO, and (d) 30% Ca-doped YBCO is shown.

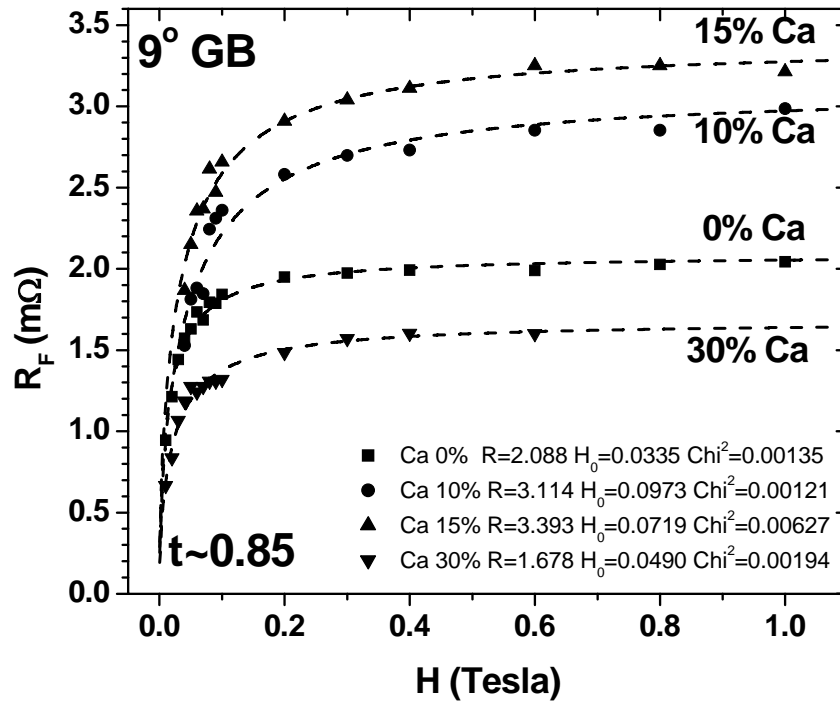


Figure IV.23 Summary of $R_F(H)$ for of $Y_{1-x}Ca_xBa_2Cu_3O_{7-\delta}$ for $x \sim 0, 0.10, 0.15,$ and 0.30 . The fitted R and H_0 values are indicated inside the figures.

Table IV.2 Calculated H_0 , l , and $J_{d,gb}$ values for each Ca-doped $[001]$ tilt 9° GB from $R_F(H)$ data.

	H_0	l	$J_{d,gb}$
0%	34 mT	39 nm	0.10 J_d
10%	97 mT	23 nm	0.17 J_d
15%	72 mT	27 nm	0.15 J_d
30%	49 mT	32 nm	0.13 J_d

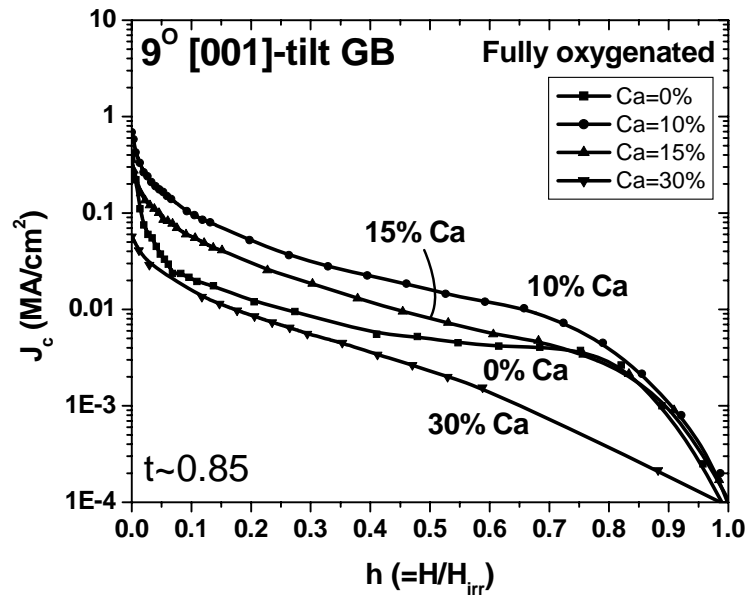


Figure IV.24 The reduced $J_c(h)$ of fully-oxygenated $Y_{1-x}Ca_xBa_2Cu_3O_{7-\delta}$ ($x=0, 0.10,$ and 0.30) for 9° [001]-tilt grain boundary. The $J_c(h)$ is measured at the same reduced temperature of ~ 0.85 for comparison. A strong contrast to the behavior at optimum T_c state (Fig. IV.20(b)) is observed.

The 9° samples were then fully oxygen-annealed for test of the influence of oxygen over-doping, and their $J_c(h)$ behavior is shown in Figure IV.24. The T_c was 88.3, 79.4, 71.9 and 64.6 K for 0%, 10%, 15%, and 30% Ca doping respectively. (T_c decreases as the doping level increases, since it further drives T_c down in the overdoping regime.) The 10% Ca exhibited the best properties over the entire field regime, even for low fields.

The section has reported on our the experiments on low angle GBs with different Ca content x ($Y_{1-x}Ca_xBa_2Cu_3O_{7-\delta}$), and demonstrated that Ca addition can strongly benefit the $J_{c,gb}$ at intermediate fields and high reduced temperature $T_m/T_c \sim 0.85$, which corresponds to 77K for pure YBCO. It was found that 15% Ca doping is most effective

for a 7° [001] tilt GB, completely eliminating the GB signature. For a 9° [001] tilt GB, 10% gave the best results, but actually with little significant improvement. The flux flow resistivity calculation was made for the 9° GB. It found that 10% Ca produced the highest grain boundary deparing current $J_{d,gb}$. Further oxygen annealing which drove the Ca-doped samples to lower T_c but higher carrier density produced a relative enhancement of $J_{c,gb}(H, t=0.85)$.

IV.4 Grain Boundary properties of $\text{Yb}_{0.9}\text{Ca}_{0.1}\text{Ba}_2\text{Cu}_3\text{O}_{7.8}$

Recently, some RE-123 ($[\text{RE}]\text{Ba}_2\text{Cu}_3\text{O}_{7.8}$) compounds (RE=Yb, Tm, Er, Ho, Y, Dy, Gd, Eu, Sm, and Nd, in order of ionic size, smaller to larger) have been recognized as attractive alternatives to YBCO. Among those various RE-123 compounds, the Yb-123 ($\text{YbBa}_2\text{Cu}_3\text{O}_{7.8}$) compound has been chosen in the following experiment to investigate the influence on Ca doping of the change of rare earth ion size. Since the Yb^{3+} ion is smaller than the Y^{3+} ion, stronger Ca segregation is anticipated. This section starts with a brief introduction to the RE-123 compounds and the effects produced by their variable the rare earth ion size, followed by the motivation and the experimental results.

The T_c of RE-123 compounds ranges from 90 to 95 K (Fig. IV.25), exhibiting a rough correlation with the radius of the rare earth ion – usually higher T_c for larger RE ions (Fig. IV. 25). Additionally, it is expected that the larger rare earth ions (Eu, Sm, and Nd) can behave in qualitatively different manner to YBCO since substitution of the rare earth ion on the Ba site is allowed.

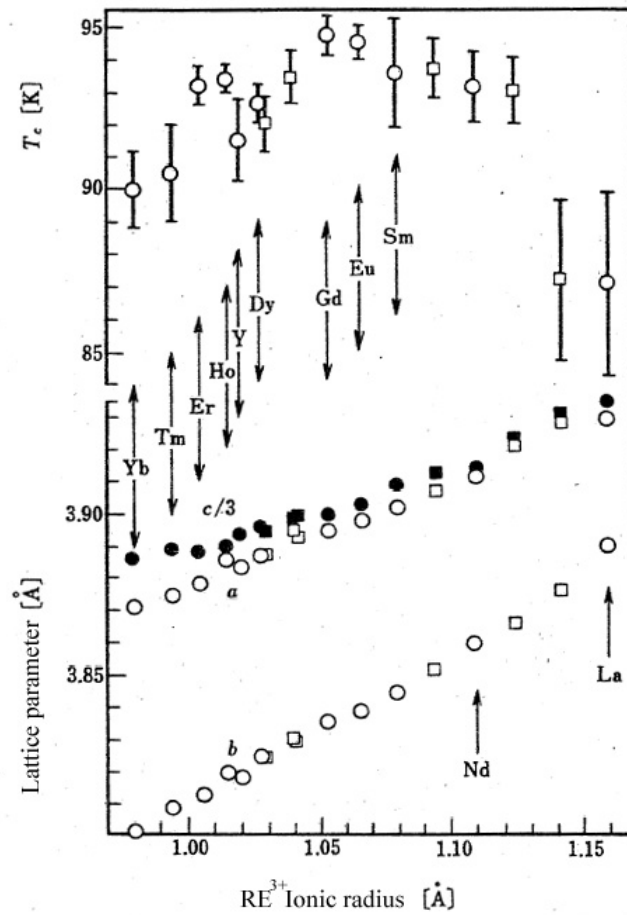


Figure IV.25 T_c and lattice parameter dependence on the ionic radii of RE ion.

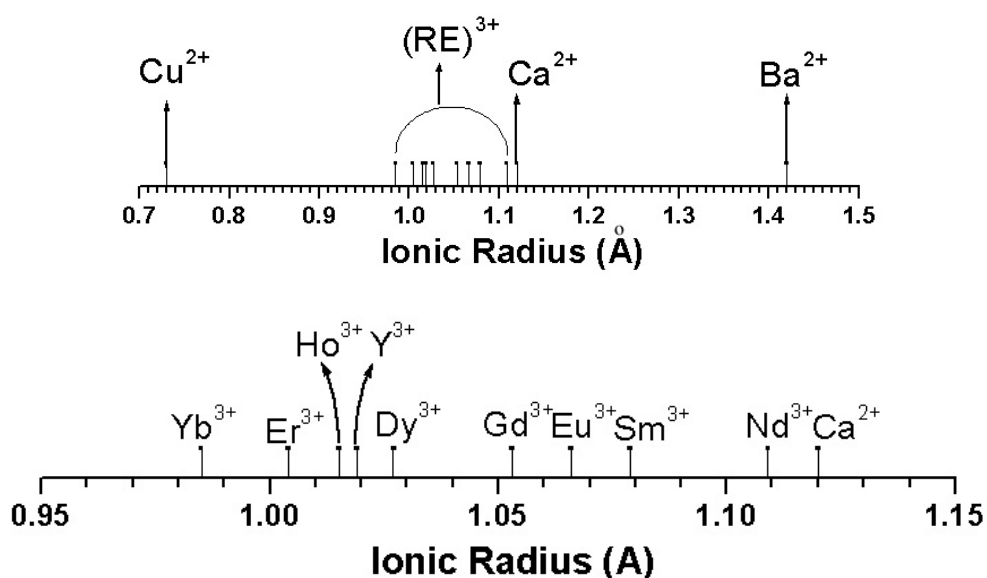
Table IV.3 Ionic size of rare earth ions for eightfold coordination (R.D. Shannon, Ref [30])

	Yb^{3+}	Er^{3+}	Ho^{3+}	Y^{3+}	Dy^{3+}	Gd^{3+}	Eu^{3+}	Sm^{3+}	Nd^{3+}
Ionic radii (Å)	0.985	1.004	1.015	1.019	1.027	1.053	1.066	1.079	1.109
Size difference against Y^{3+}	-3.3%	-1.5%	-0.4%	0.0%	+0.8%	+3.3%	+4.6%	+5.9%	+8.8%

Table IV.4 Ionic sizes of YBCO elements, including Ca^{2+} ion, for eightfold coordination

	Y^{3+}	Ba^{2+}	Cu^{2+}	Ca^{2+}
Ionic radii (Å)	1.019	1.42	0.73	1.12
Size difference against Y^{3+}	0.0%	+29.5%	-28.4%	+9.9%

In order to understand GB segregation behavior further, a study of Ca-doping effects in $\text{Yb}_{1-x}\text{Ca}_x\text{Ba}_2\text{Cu}_3\text{O}_{7-\delta}$ compounds was made. The ionic sizes of rare earth ions are indicated in Table IV.3, and the ionic radii Y, Ba, Cu, and Ca ions are shown in Table IV.4 for comparison. (In Figure IV.26, ionic radii of RE^{3+} are shown graphically as well, for easy comparison.) Yb^{3+} (0.985 Å) ion is one of the smallest RE ions.

**Figure IV.26** Ionic radii of RE^{3+} ions and elements in YBCO (R.D. Shannon, Ref [30]).

The straightforward idea underlying my experiment is that the $(\text{Yb})_{1-x}\text{Ca}_x\text{Ba}_2\text{Cu}_3\text{O}_{7-\delta}$ system allows variation of the strain effect on Ca segregation at the GB by changing the size of the RE^{3+} . To assess Ca-segregation effects in the Yb-123 compounds, the segregation model [5] (Eq. IV.1) was again used, assuming that the smaller RE ionic radius (Yb^{3+}) only modifies the pressure field effect, while the screened electric potential remains the same as in $\text{Y}_{0.7}\text{Ca}_{0.3}\text{Ba}_2\text{Cu}_3\text{O}_{7-\delta}$ [5]. For Ca-doped $\text{YbBa}_2\text{Cu}_3\text{O}_{7-\delta}$, where the size difference between Yb^{3+} and Ca^{2+} is $\sim 12\%$, it was computed a stronger Ca segregation effect at the GB core (see Figure IV.27) in YBCO, thus leading us to expect that a lower Yb doping would be more effective. The expected segregation profiles for 10% Ca-doped YBCO and 10% Ca-doped Yb-BCO are shown in Figure IV.27. Figure IV.27(c) shows the Ca distribution at a 7° [001] tilt GB of $[\text{Y}]_{0.85}\text{Ca}_{0.15}\text{Ba}_2\text{Cu}_3\text{O}_{7-\delta}$, which showed the best results (complete elimination of GB signature) in the Ca-doped study in YBCO. The Ca segregation level at the GB core for this 15% Ca-doped YBCO is $\sim 25\text{-}30\%$, similar to that of the 10% Ca-doped Yb-BCO.

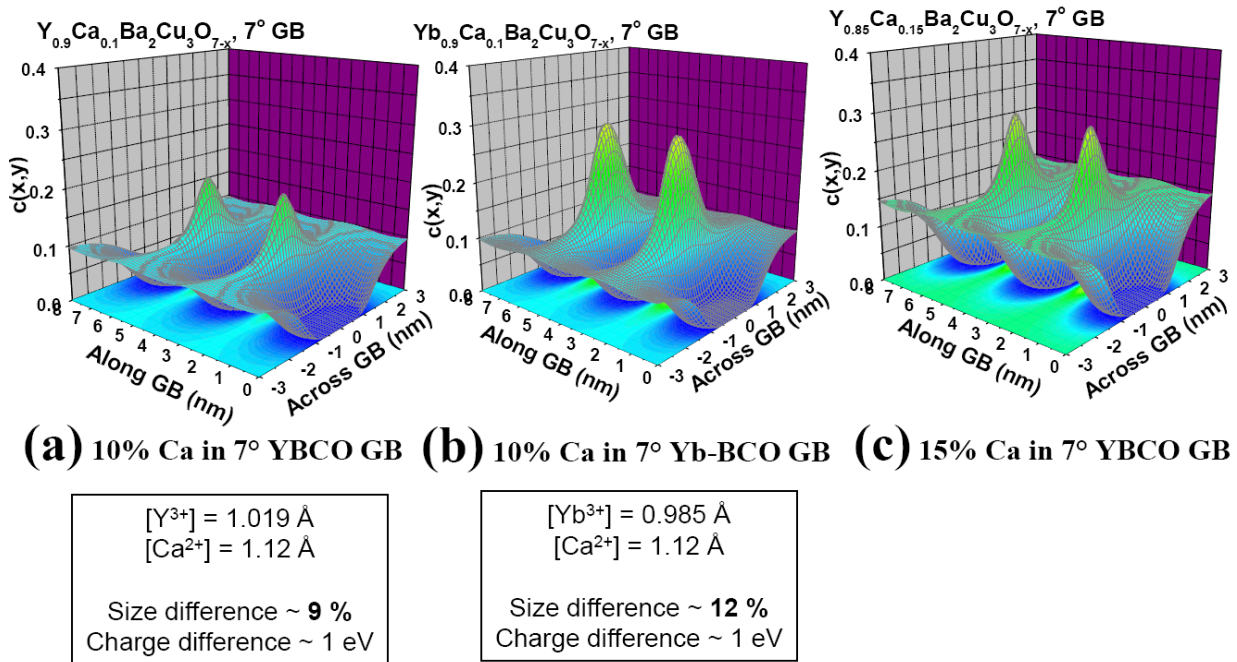


Figure IV.27 Surface contour plot of the concentration of Ca^{2+} solute ions near a periodic chain of GB dislocations in a 7° GB calculated from equation (IV.1) for (a) $[Yb]_{0.9}Ca_{0.1}Ba_2Cu_3O_{7-\delta}$, and (b) $[Y]_{0.9}Ca_{0.1}Ba_2Cu_3O_{7-\delta}$. Stronger segregation is anticipated for [Yb]BCO. (c) shows the results for $[Y]_{0.85}Ca_{0.15}Ba_2Cu_3O_{7-\delta}$, which showed the best results for $J_{c,gb}$ in the Ca-doping study in YBCO.

With these calculations as the guide, 10% Ca-doped $YbBa_2Cu_3O_{7-\delta}$ were grown on single crystal STO substrate, and 6° and 9° [001] tilt symmetric bicrystal STO by PLD. The 10% Ca doping level was chosen because it was believed that the Ca segregation level at the grain boundary core is similar to that of the 15% optimum Ca-doped YBCO that showed the best $J_{c,gb}$ improvement (~ 25 – 30 %, Figure IV.27). The substrate temperature was 800-810 °C, while the oxygen pressure was set at 200 mTorr during growth. 5000 pulses at 5 Hz were used to deposit ~ 300 nm thick films. The samples were post oxygen annealed in the oxygen pressure of 800 Torr at 475-500 °C in two hours

for full oxygenation. Current bridges $40\ \mu\text{m}$ (wide) \times $1000\ \mu\text{m}$ (long) were cut for all samples for detailed transport measurements. All samples were measured at the same reduced temperature t ($t=T_{\text{measure}}/T_c$) of 0.85 for comparison. The T_c was 69.9, 72.9, and 72.0 K, respectively for single crystal, 6° , and 9° samples.

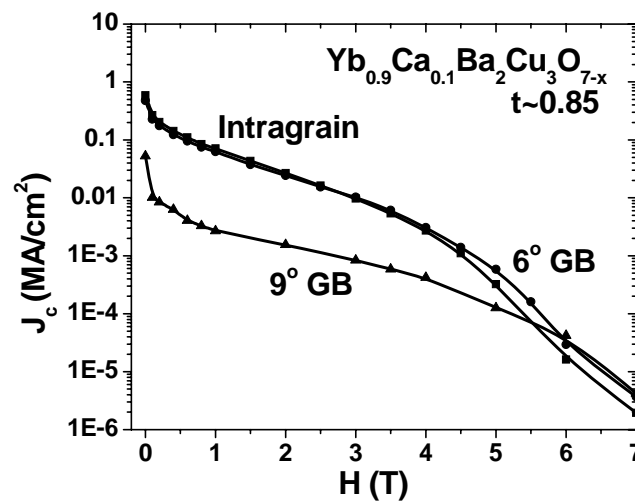


Figure IV.28 The $J_c(H)$ of $\text{Yb}_{0.9}\text{Ca}_{0.1}\text{Ba}_2\text{Cu}_3\text{O}_{7-\delta}$ for 0° , 6° and 9° GB.

Figure IV.28 shows the $J_c(H)$ of $\text{Yb}_{0.9}\text{Ca}_{0.1}\text{Ba}_2\text{Cu}_3\text{O}_{7-\delta}$ for 0° , 6° and 9° GB at the same reduced temperature $t \sim 0.85$. The $J_c(H)$ of 6° GB is almost identical with intragrain $J_c(H)$, implying that there is no GB limitation for 10% Ca-doped Yb-123. It is remarkable that 10% Ca doping of the 6° [Yb]BCO GB recovers the intra-grain J_c value. For the 9° GB, a large J_c reduction exists for 10% Ca doped sample over the entire field range. Figure IV.29 shows the corresponding V-I characteristics for intragrain (0°), 6° and 9° GB at $t \sim 0.85$. The 10% Ca-doped 6° GB showed no GB-signature.

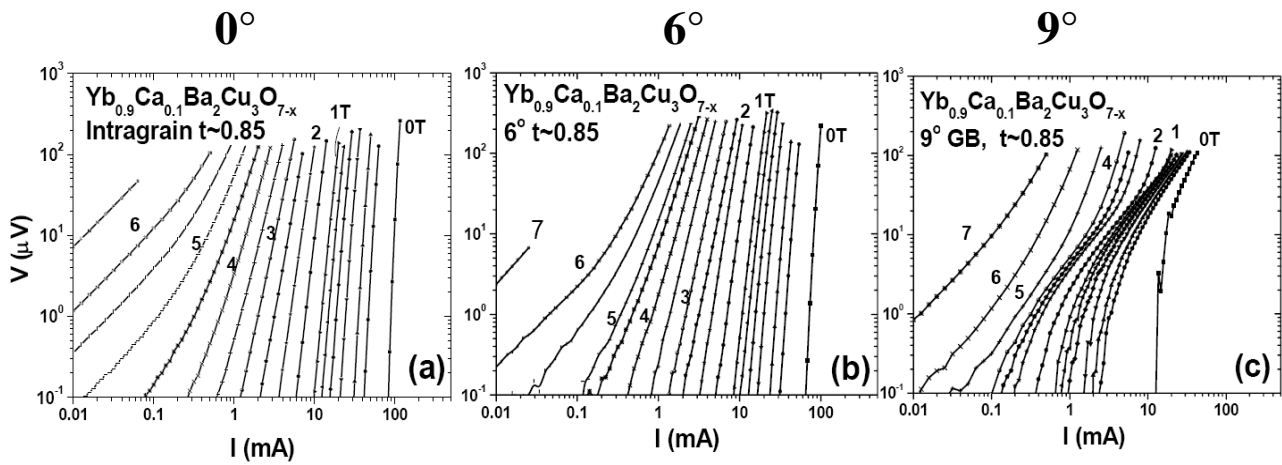


Figure IV.29 V-I characteristics of $\text{Yb}_{0.9}\text{Ca}_{0.1}\text{Ba}_2\text{Cu}_3\text{O}_{7-\delta}$ for (a) 0° , (b) 6° and (c) 9° GB.

The observed behavior produced by 10% Ca doping in Yb-123 for the 6° GB is the same as that produced by 15% Ca doping of YBCO (elimination of GB dissipation signature in V-I curves), but it is more interesting since the magnitude of intergrain $J_{c,gb}$ recovers the intragrain J_c values of Yb-123. Yb-123 GB induces stronger segregation than YBCO GB due to its higher strain potential with Ca^{2+} ion. From the predictions of the segregation model shown in Figure IV.27, it is shown that $\sim 25 - 30\%$ Ca at GB core is optimum for 15% Ca- YBCO and for 10% Ca Yb-BCO. Stronger segregation in the Yb-123 system thus makes smaller Ca doping effective. Further STEM/EELS analysis is planned on this 10% Ca-doped 6° GB Yb-123 sample to provide a better understanding of the behavior.

Even though these results demonstrate the possibility of complete elimination of the GB dissipation by Ca doping in both YBCO and Yb-123, rather significant T_c reduction is produced. This T_c reduction makes this a scientific, rather than a technological solution at

this stage. The following work proposes a possible dopant other than Ca, which would not significantly degrade the T_c of the grain.

IV.5 Grain Boundary properties of $Y_{0.9}Nd_{0.1}Ba_2Cu_3O_{7-\delta}$

IV.5.1 Background

In this section, my study of $Y_{1-x}Nd_xBa_2Cu_3O_{7-\delta}$ GB is reported. The doping of Nd^{3+} , an isovalent substitute for Y^{3+} , allows the study of cation segregation driven only by the pressure field. $Y_{1-x}Nd_xBa_2Cu_3O_{7-\delta}$ forms a solid solution when x ranges from 0.098 to 0.410 [31]. If we consider Nd^{3+} as a dopant, the pressure field effect is expected to drive Nd^{3+} to segregate at the GB without any electric potential effect. Doping by Nd^{3+} is also not expected to suppress T_c , if Nd^{3+} substitutes for Y^{3+} . (However, T_c could decrease if Nd^{3+} substitutes for Ba^{2+} (see Fig. IV.5)) The pressure field effect around the GB is expected to segregate Nd at GB cores since Nd^{3+} is much larger than Y^{3+} . Therefore, the larger Nd^{3+} ion will segregate to the tensile regions of GB dislocations, while being depleted in the compressed regions. The predicted Nd segregation profiles for 10% and 30 % Nd substitution are shown in Figure IV.30. The expected strong GB segregation of Nd^{3+} may be advantageous if only a small Nd doping can improve the carrier density around the GB cores.

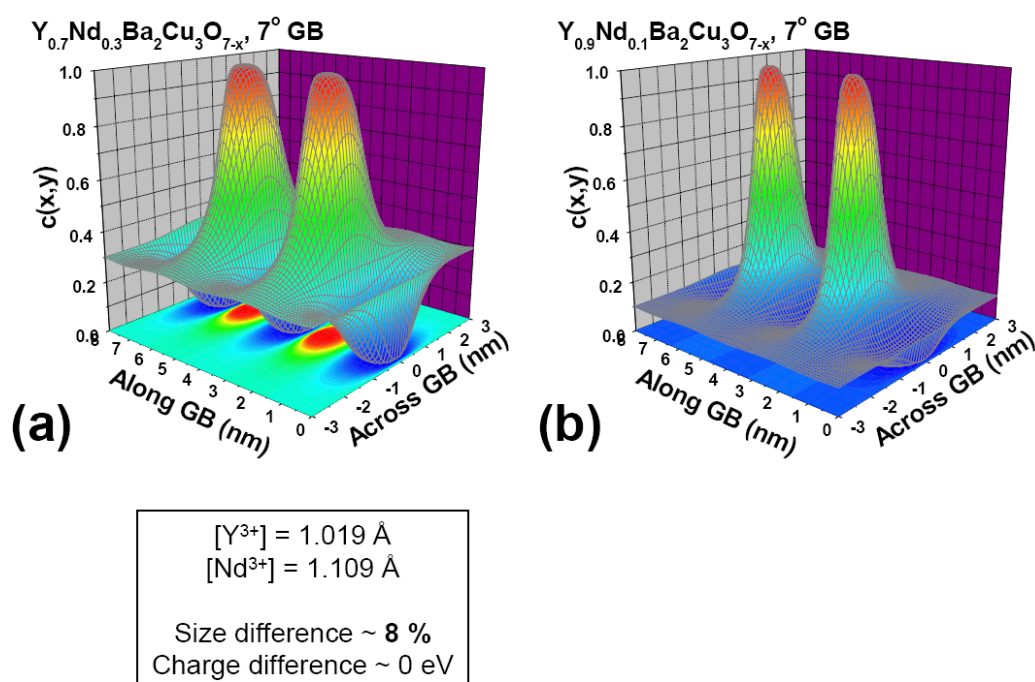


Figure IV.30 Surface plot of the concentration of Nd^{3+} solute ions near a periodic chain of edge dislocations in a 7° [001]-tilt GB calculated from equation (x) for (a) $Y_{0.7}Nd_{0.3}Ba_2Cu_3O_{7-\delta}$, (b) $Y_{0.9}Nd_{0.1}Ba_2Cu_3O_{7-\delta}$. Very strong segregation is expected in both cases.

10% Nd doped samples, $Y_{0.9}Nd_{0.1}Ba_2Cu_3O_{7-\delta}$, were chosen for the experiment. The $Y_{0.9}Nd_{0.1}Ba_2Cu_3O_{7-\delta}$ films were grown by PLD on single crystal STO, and 6° and 9° [001] tilt symmetric bicrystal STO substrates. The substrate temperature was set at $800\text{--}810^\circ\text{C}$ during growth. Varying oxygen pressures p_{O_2} of 300, 250, and 200 mTorr during growth produced the different T_c , and rather different GB transport characteristic. The film grown in 300 mTorr p_{O_2} showed T_c of $\sim 87\text{--}88\text{ K}$, the highest T_c among the films. The films grown in 250 mTorr or 200 mTorr exhibited rather lower T_c of $\sim 86\text{ K}$ and $\sim 85\text{ K}$

respectively. 5000 pulses at 5 Hz were used to deposit ~ 300 nm thick films. The samples were post-annealed in oxygen partial pressures of 800 Torr at 475-500 °C for two hours for full oxygenation. Bridges of 40 μm (width) \times 1000 μm (length) were cut for all samples for detailed transport measurement. All samples were measured at the same reduced temperature t ($t=T_{\text{measure}}/T_c$) of 0.85 for comparison. The samples grown at 250 mTorr were measured at some other temperatures including 77K and 65K.

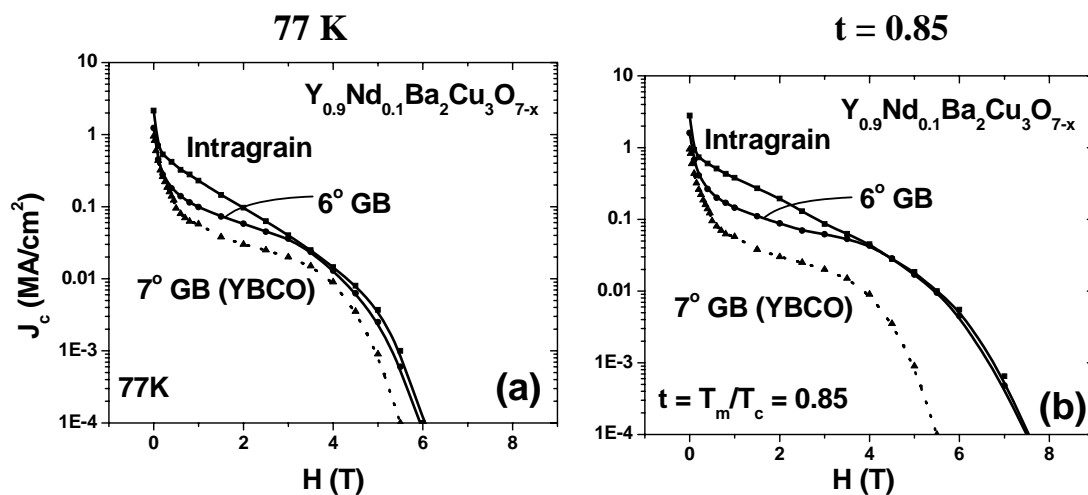


Figure IV.31 $J_c(H)$ of the intragrain and the 6° GB of $\text{Y}_{0.9}\text{Nd}_{0.1}\text{Ba}_2\text{Cu}_3\text{O}_{7-\delta}$ grown in p_{O_2} of 300 mTorr, (the $J_c(H)$ of the 7° GB of YBCO is shown as well for comparison) (a) at 77K and (b) at reduced temperature $t \sim 0.85$. The 6° GB shows reduced $J_{c,\text{gb}}$ in fields less than 3.5 – 4.0 T. The behavior is not very different from pure YBCO. No distinctive improvement of GB properties was observed. T_c were 88.0 and 87.2K for 0° and 6° $\text{Y}_{0.9}\text{Nd}_{0.1}\text{Ba}_2\text{Cu}_3\text{O}_{7-\delta}$ films.

IV.5.2 Growth of $Y_{0.9}Nd_{0.1}Ba_2Cu_3O_{7-\delta}$ at 300 mTorr

T_c were 88.0 and 87.2 K for 0° and 6° $Y_{0.9}Nd_{0.1}Ba_2Cu_3O_{7-\delta}$ films grown in p_{O_2} of 300 mTorr. The T_c is the highest among the samples grown in the various oxygen pressure conditions. Figure IV.31 shows the $J_c(H)$ of the samples at 77K and at a reduced temperature $t = T_m/T_c \sim 0.85$. In this case, the J_c across the 6° GB is reduced at magnetic fields less than 3 – 4 T compared to its intragrain J_c . The degree of reduction seems to be less than the J_c reduction in YBCO, if compared to the $J_c(H)$ of the 7° YBCO GB (Fig. IV.31(a)). Figure IV.32 exhibits the V-I characteristics of the 6° GB at 77K and at $t \sim 0.85$. Both show that the GB dissipation signature still exists.

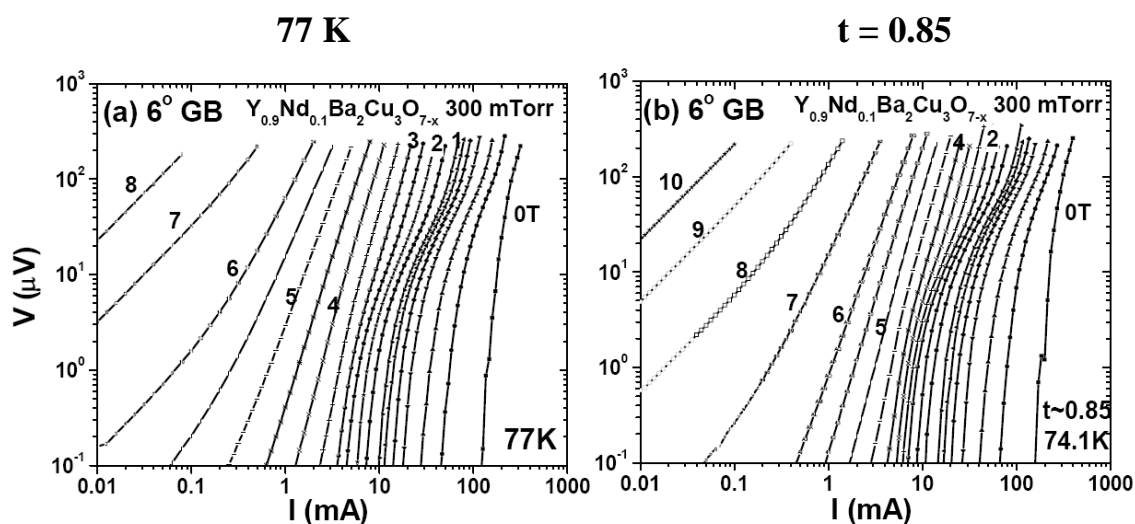


Figure IV.32 V-I characteristics of the 6° $Y_{0.9}Nd_{0.1}Ba_2Cu_3O_{7-\delta}$ film grown in 300 mTorr for GB (a) at 77K and (b) at $t \sim 0.85$.

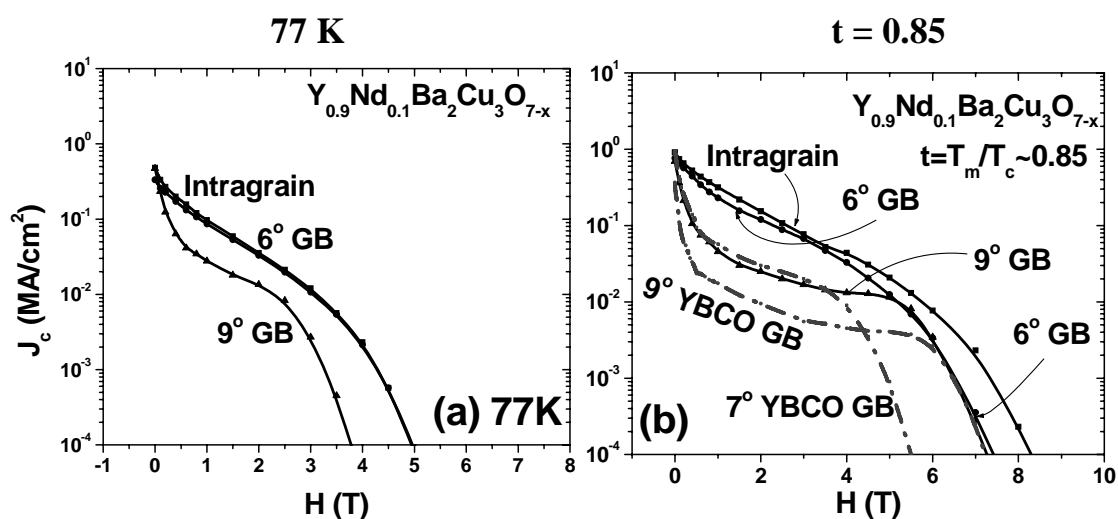


Figure IV.33 $J_c(H)$ of the intragrain, 6°, and 9° GB of $Y_{0.9}Nd_{0.1}Ba_2Cu_3O_{7-\delta}$ films grown in 250 mTorr (a) at 77K and (b) at $t \sim 0.85$. The $J_c(H)$ of the intragrain and 6° GB are almost identical. The $J_c(H)$ of 7° and 9° YBCO GB at $t \sim 0.85$ was plotted for comparison. T_c values grown in 250 mTorr were 85.8, 86.5 and 84.5 K for 0°, 6° and 9° samples, respectively.

IV.5.3 Growth of $Y_{0.9}Nd_{0.1}Ba_2Cu_3O_{7-\delta}$ at 250 mTorr

T_c values grown in 250 mTorr were 85.8, 86.5 and 84.5 K for 0°, 6° and 9° films, respectively. In this case, in spite of 1 – 2 K lower T_c , the complete loss of GB signature and the J_c recovery was observed which is very promising. Figure IV.33 shows the $J_c(H)$ of the samples at 77K and $t \sim 0.85$. The $J_c(H)$ of the intragrain and the 6° GB are almost identical at 77K, while the 9° GB shows a reduction of J_c across the GB. The $J_c(H)$ of 7° and 9° YBCO GB at $t \sim 0.85$ was plotted for comparison in Fig. IV.33(b). The 6° $Y_{0.9}Nd_{0.1}Ba_2Cu_3O_{7-\delta}$ GB shows a large J_c improvement over the entire field range compared to that of a 7° pure YBCO GB. This implies the great potential of the Nd doping influence on low angle grain boundary. In addition, the 9° $Y_{0.9}Nd_{0.1}Ba_2Cu_3O_{7-\delta}$ GB also indicates an improved J_c , compared to the 9° pure YBCO GB. It is even more promising that the Nd

doping exhibits quite positive effect both on 6° and 9° GB, without large T_c reduction. (T_c is ~ 85 -86 K, which may be yet acceptable.)

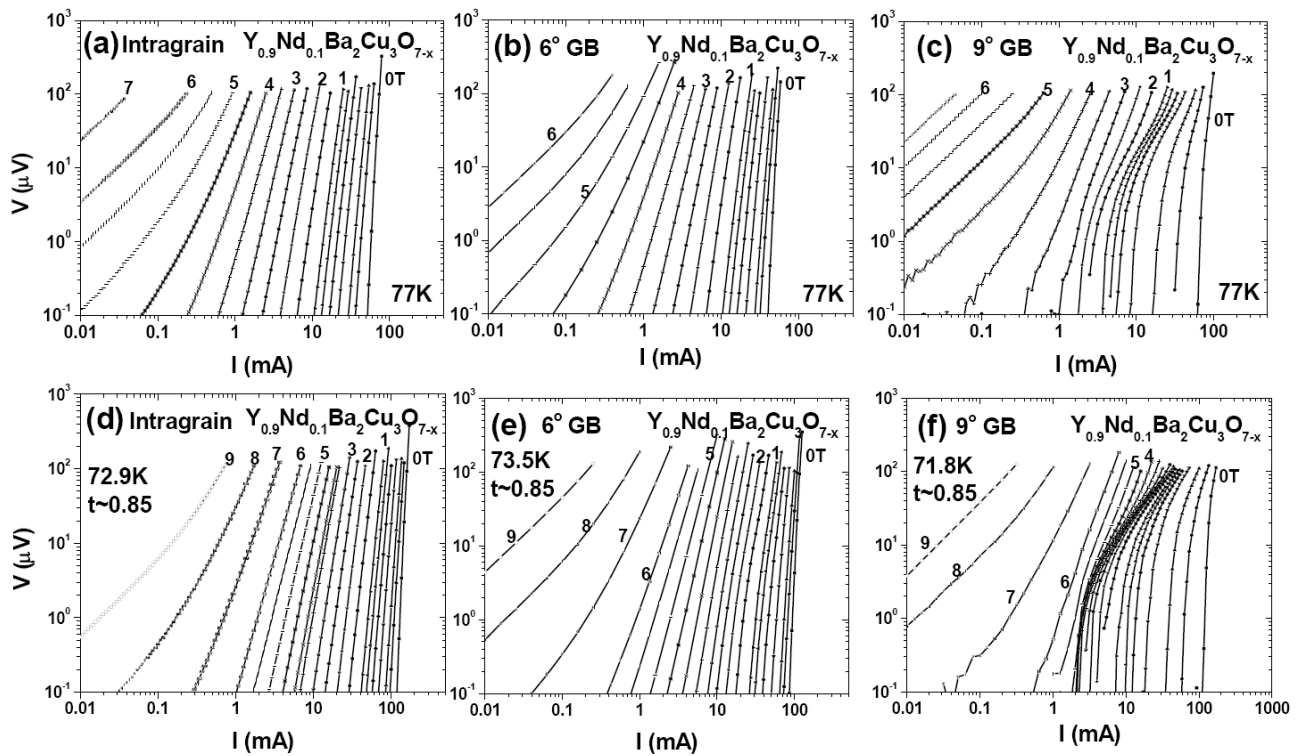


Figure IV.34 V-I characteristics of $Y_{0.9}Nd_{0.1}Ba_2Cu_3O_{7-\delta}$ grown at 250 mTorr for (a) 0°, (b) 6° and (c) 9° GB at 77K, and for (d) 0°, (e) 6° and (f) 9° GB at $t \sim 0.85$. No large GB dissipation signature is seen for the 6° GBs. There is indeed no large difference between the intragrain and 6° GB V-I curves.

Figure IV.34 exhibits the V-I characteristics of $Y_{0.9}Nd_{0.1}Ba_2Cu_3O_{7-\delta}$ samples grown at 250 mTorr. Complete loss of GB signature by the 10% Nd doped YBCO for 6° GB at 77K is shown. However, there is a small GB dissipation signature on testing the 6° $Y_{0.9}Nd_{0.1}Ba_2Cu_3O_{7-\delta}$ GB at the lower temperature of 73.5K, which is $t \sim 0.85$ (Fig. IV.34(e)).

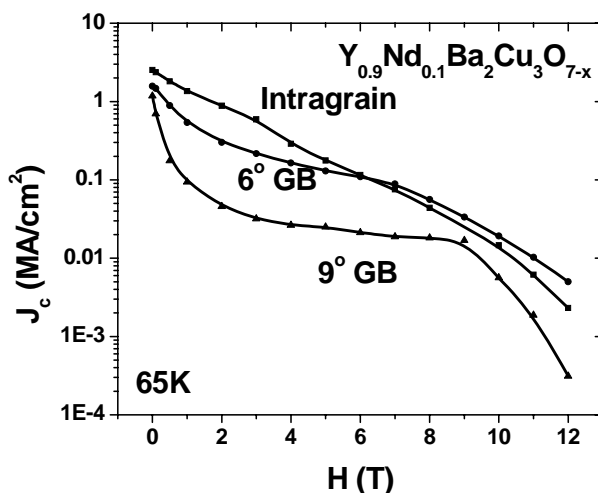


Figure IV.35 $J_c(H)$ of the intragrain, 6°, and 9° GB of $Y_{0.9}Nd_{0.1}Ba_2Cu_3O_{7-\delta}$ samples grown at 250 mTorr at 65 K. The $J_c(H)$ of the 6° GB shows the reduction at lower field. This is reasonable, since the GB effect becomes larger as temperature decreases.

Figure IV.35 shows the $J_c(H)$ of the $Y_{0.9}Nd_{0.1}Ba_2Cu_3O_{7-\delta}$ films for 0°, 6°, and 9° GB at 65 K. The $J_c(H)$ of the 6° GB exhibited lower J_c at the fields less than 6 T compared to the intragrain J_c . Thus we return to a behavior clearly observed in low field magneto-optic MO studies [32], where the GB blocking effect increases as the temperature is lowered. This behavior of the GB dissipation becoming larger as temperature decreases was discussed in Chapter III.1. Even though the complete loss of GB signature was observed at 77 K, the GB dissipation signature recurs at temperatures less than 65 K. The 9° GB shows large reduction of J_c up to ~ 9 T. The occurrence of GB signature at 6° GB at 65K is more explicitly shown in Figure IV.36(b).

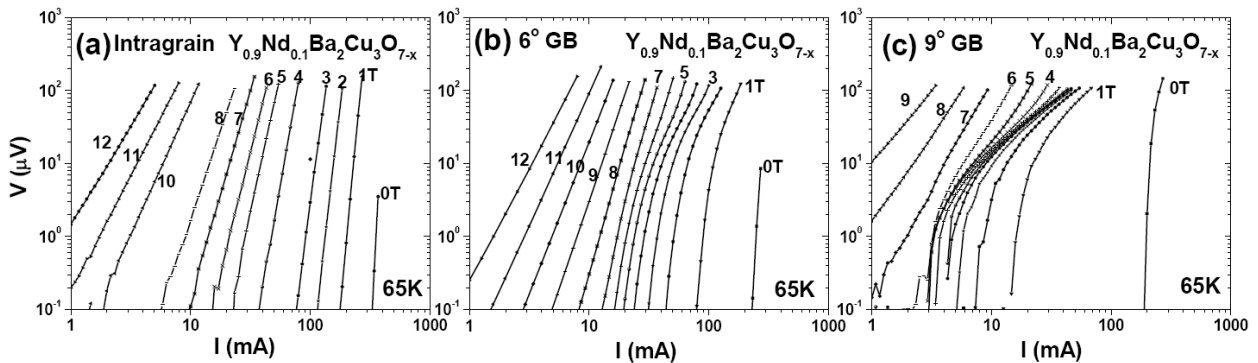


Figure IV.36 V-I characteristics of $\text{Yb}_{0.9}\text{Ca}_{0.1}\text{Ba}_2\text{Cu}_3\text{O}_{7-\delta}$ grown at 250 mTorr for (a) 0° , (b) 6° and (c) 9° GB at 65K. The V-I curves of the 6° GB showed GB signature at 65K.

IV.5.4 Growth of $\text{Y}_{0.9}\text{Nd}_{0.1}\text{Ba}_2\text{Cu}_3\text{O}_{7-\delta}$ at 200 mTorr

Lastly, a $\text{Y}_{0.9}\text{Nd}_{0.1}\text{Ba}_2\text{Cu}_3\text{O}_{7-\delta}$ sample set was grown in an oxygen pressure of 200 mTorr. The T_c of the samples were 85.5, 84.2 and 83.5 K for 0° , 6° and 9° samples, respectively. The complete loss of GB dissipation signature was observed in the 6° GB too. Figure IV.37(a) shows the $J_c(H)$ of the $\text{Y}_{0.9}\text{Nd}_{0.1}\text{Ba}_2\text{Cu}_3\text{O}_{7-\delta}$ samples for the intragrain and the 6° GB at $t \sim 0.85$, with $J_c(H)$ plot of the 7° YBCO GB for comparison. The $J_c(H)$ of the intragrain and 6° GB shows rather similar behavior. Even though comparison is made between 6° and 7° GBs, the great enhancement of GB transport $J_{c,gb}$ is shown explicitly for this 10% Nd doped YBCO. Figure IV.37(b) exhibits the $J_c(H)$ of the $\text{Y}_{0.9}\text{Nd}_{0.1}\text{Ba}_2\text{Cu}_3\text{O}_{7-\delta}$ film for the 9° GB at $t \sim 0.85$, with $J_c(H)$ of the 9° YBCO GB for comparison. The $J_{c,gb}$ across the 9° GB is greatly improved by 2 – 5 times. The complete loss of GB signature is shown in Figure IV.38(b) for the 6° $\text{Y}_{0.9}\text{Nd}_{0.1}\text{Ba}_2\text{Cu}_3\text{O}_{7-\delta}$ GB. Even though there is a large grain boundary signature in the 9° $\text{Y}_{0.9}\text{Nd}_{0.1}\text{Ba}_2\text{Cu}_3\text{O}_{7-\delta}$ GB, it can be concluded that the GB dissipation is much less than that of YBCO, judged by the J_c improvement shown in Fig. IV.37(b).

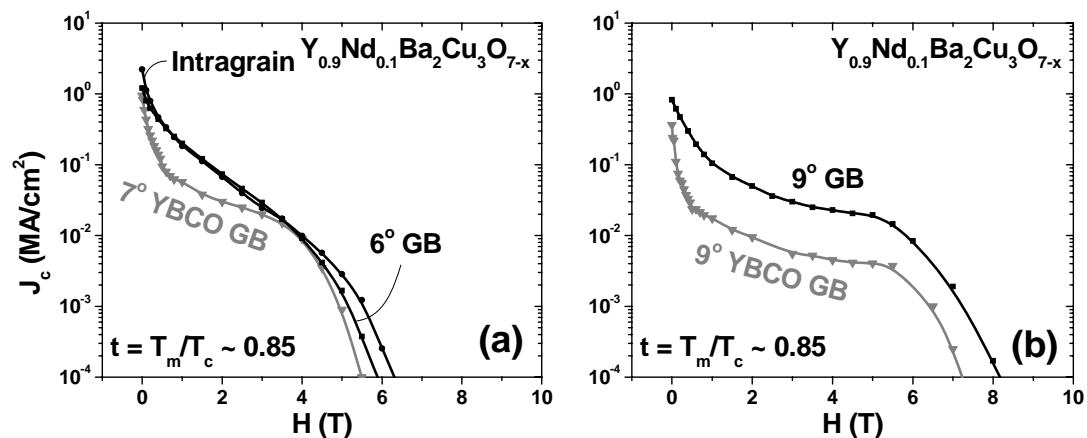


Figure IV.37 (a) $J_c(H)$ of the intragrain and 6° GB of $Y_{0.9}Nd_{0.1}Ba_2Cu_3O_{7-\delta}$ films grown at 200 mTorr at $t \sim 0.85$. The $J_c(H)$ of 7° YBCO GB was shown for comparison. Clear enhancement of J_c is shown at low field. (b) $J_c(H)$ of the 9° GB of $Y_{0.9}Nd_{0.1}Ba_2Cu_3O_{7-\delta}$ films grown at 200 mTorr at $t \sim 0.85$. The $J_c(H)$ of the 9° YBCO GB is shown for comparison.

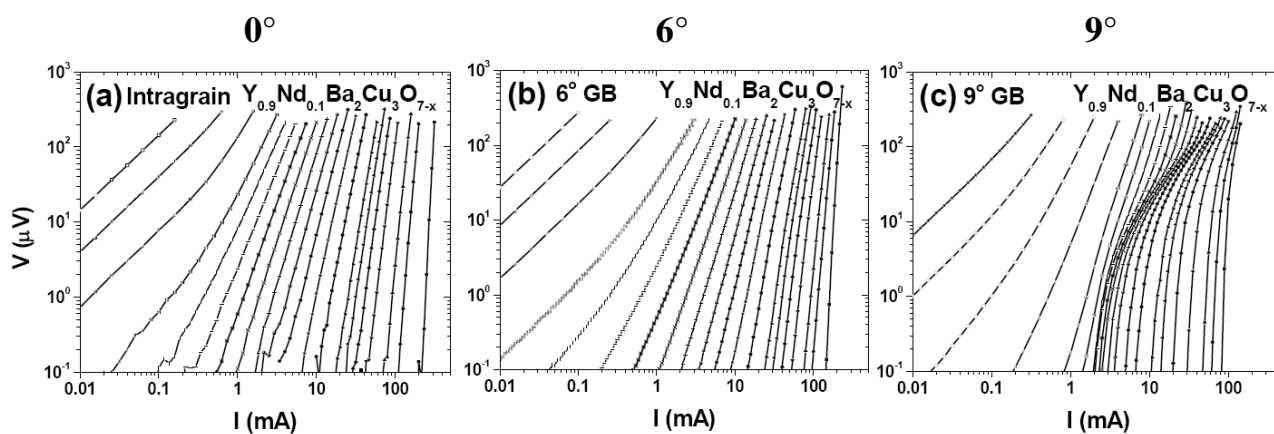


Figure IV.38 $V-I$ characteristics of $Y_{0.9}Ca_{0.1}Ba_2Cu_3O_{7-\delta}$ films grown at 200 mTorr for (a) 0° , (b) 6° and (c) 9° GB at $t \sim 0.85$. The $V-I$ curves of the 6° GB showed no GB signature.

IV.5.5 Nd doping effect on YBCO

The results on the investigation of $Y_{0.9}Nd_{0.1}Ba_2Cu_3O_{7-\delta}$ GBs were given in this section IV.5. The size difference between Y^{3+} and Nd^{3+} was expected to allow segregation of Nd^{3+} at the GB core and reduction of lattice distortion, which would reduce the strain at the GB and might produce fewer oxygen vacancies, thus leading to enhanced carrier density and superconducting properties. In addition, we believed that Nd^{3+} doping would not suppress T_c strongly, if substituting for Y^{3+} . Thus, Nd^{3+} doping in YBCO was proposed to improve $J_{c,gb}$ properties without large T_c reduction. We found that the $Y_{0.9}Nd_{0.1}Ba_2Cu_3O_{7-\delta}$ compound exhibited different T_c and different transport characteristics according to its growth oxygen pressure. Even though the highest T_c of ~ 88 K was obtained at oxygen pressure of 300 mTorr, no explicit disappearance of grain boundary dissipation was observed. However, the other two sample sets grown at 250 and 200 mTorr showed the complete elimination of GB dissipation at V-I characteristics, and total recovery of $J_{c,gb}$ up to its intragrain J_c values at a reduced temperature $t \sim 0.85$, even though the T_c of the samples was a little degraded to 84 – 86 K (Yet, these values are much better than the 69-80 K of Ca-doped YBCO). Even though no loss of GB dissipation signature was seen for the 9° GB for these samples, the $J_{c,gb}$ improvement by 2 – 5 times was seen too. It is remarkable that $J_{c,gb}$ of the 6° GB recovered the intragrain J_c value, while the 9° GB showed a modest $J_{c,gb}$ enhancement compared to the pure YBCO 9° GB with only 5 – 6 K T_c reduction. Since real coated conductors made by RABiTS techniques include low angle GBs which range up to $\sim 8^\circ$, Nd/Y substitutions could benefit applications by enhancing the global

J_c , if the Nd doping can be incorporated with preferred coated conductor YBCO growth techniques.

The $J_{c,gb}$ improvement and the possibility of eliminating GB dissipation in the Nd-doped YBCO system is important scientifically. The feasibility of adopting trivalent cation doping in YBCO with lower T_c reduction than by the bivalent Ca^{2+} was shown. The Nd doping in YBCO was successfully tested, and demonstrated the value of searching other and perhaps better elements, such as the large rare earth ions, Gd^{3+} , Eu^{3+} , Sm^{3+} or some other trivalent ion substituting for Y^{3+} . This study has already provided a better understanding of the cation segregation effects around the GB core, and its influence on the transport properties. However, intended compositional mapping by electron energy loss spectroscopy on this grain boundary core structure will add essential Nd segregation profile around GB cores, thus providing the complete understanding on this segregation phenomenon. Indeed, the dopant Nd showed new possibility for manipulating the properties of other cation doped GB using dopants other than Ca.

IV.6 Summary

The single most important obstacle standing in the way of conductor design flexibility of the HTS materials is the degraded superconducting properties of grain boundaries, since misorientations of more than a few degrees stands in the way of the desire for high J_c and minimum current blocking. The essential issue of grain boundaries in pure YBCO is that they are under-doped with respect to the grains due to the local GB strain

produced by the distorted GB lattice structure. The under-doped nature of the GB can be fixed by *over-doping* or *strain relief*, which can be achieved by a combination of partial Ca substitution, or other cation substitution. To understand these phenomena, three complementary sample sets were investigated, including the $Y_{1-x}Ca_xBa_2Cu_3O_{7-\delta}$ films with various Ca contents, the $Yb_{0.9}Ca_{0.1}Ba_2Cu_3O_{7-\delta}$ system, and the $Y_{0.9}Nd_{0.1}Ba_2Cu_3O_{7-\delta}$ system. The approach was to combine segregation modeling of the alloyed grain boundary with $J_c(H)$ data taken on films of quasi-ideal, single grain boundaries produced by thin film growth methods. The improved $J_{c,gb}$, weaker superconductivity depression, and weaker (or no) grain boundary dissipation signature were seen at the boundaries of the Ca-doped YBCO, the Ca-doped Yb-BCO, and the Nd-doped YBCO. These results are reasonably explained by the expected enhanced carrier density at GB dislocation cores induced by the cation segregation to the GB cores that was anticipated from the cation segregation model. Based on the electromagnetic results, the viability of both Ca- and cation- (Nd) doping approach has been established.

First, it was shown that the Ca additions in YBCO can strongly benefit the current density of low angle GBs in intermediate field. 15% Ca doping was found to be the most effective at enhancing GB transparency for a 7° GB in YBCO, while the 10% Ca exhibited the best properties for a 9° GB. The Abrikosov-Josephson vortex core size was deduced for the 9° GBs of Ca-doped films, and a reduction of core size was calculated for Ca-doped GB with respect to YBCO GB. The smallest core size occurred at 10% Ca-doping. The $J_c(h)$ behavior of the 10% Ca-doping on 9° GB exhibited the better transport properties, agreeing with the core size calculation. The voltage-current characteristics exhibited little or no sign

of GB dissipation in intermediate fields, which suggests the possibility of removing grain boundary effects in CC and, very desirably, achieving single-crystal-like properties. The lattice structure observed by Z-contrast imaging for the 15% Ca-doped 7° GB film, found that the lattice distortion, which reduces the oxygen content around GB cores, was greatly reduced or disappeared. Further STEM/EELS work to measure the local hole content is planned.

(Yb)Ba₂Cu₃O_{7-δ} was predicted to achieve the optimum Ca-doping state at lower Ca-doping with additional advantage of smaller T_c reduction. The 10% Ca-doped Yb-123 system (Yb_{0.9}Ca_{0.1}Ba₂Cu₃O_{7-δ}) was investigated and it was found that the 6° GB showed the complete elimination of GB dissipation signature. In this case, J_{c,gb} across 6° Yb_{0.9}Ca_{0.1}Ba₂Cu₃O_{7-δ} film recovers the intragrain J_c of Yb-123. Despite the advantages observed in this system, Ca doping still reduces T_c of the grains significantly for both YBCO and Yb-BCO. This T_c reduction makes this a scientific rather than a technological solution at this stage.

To attempt to remedy the T_c depression effects of Ca, Nd doping in YBCO system was investigated. The Y_{0.9}Nd_{0.1}Ba₂Cu₃O_{7-δ} system allowed strong segregation of Nd³⁺ at the GB cores, reducing the strain/lattice distortion around the GB cores and, we believe, the oxygen vacancy concentration. The sample sets grown at 250 and 200 mTorr showed the complete elimination of GB dissipation signature at V-I characteristics, and full recovery of J_{c,gb} up to its intragrain J_c across a 6° GB without significant T_c reduction (T_c of the samples was a little lower at around 84 – 86 K.) The viability of adopting Nd doping was

demonstrated suggesting a need to search for other better elements as well, like larger rare earth ion, Gd^{3+} , Eu^{3+} , Sm^{3+} or some other trivalent ion that can substitute for Y^{3+} .

The transport measurements showed that the enhanced grain boundary critical current densities $J_{c,gb}$ of Ca-doped YBCO/YbBCO and Nd-doped YBCO bicrystals were achieved. The cause is inhomogeneous Ca/Nd segregation, as expected from the cation segregation model. Not yet checked is the expectation that cation segregation increases the carrier density at the GB, which is significantly depleted at pure YBCO GBs due to lattice distortion and charging effects. But we did demonstrate a complete elimination of the GB dissipation signature in V-I characteristics of 6° GBs, well beyond the 2-3° Dimos limit for pure YBCO GBs and showed that total recovery of $J_{c,gb}$ up to its intragrain J_c can be achieved. These studies have provided the better understanding of the cation segregation effect around the GB core, and its influence on the transport properties. This issue is of great interest for superconductors and more broadly for many types of complex oxides in which grain boundaries exert a major influence on their properties. The work will be completed by state-of-the-art analytical electron microscopy to determine the segregant composition profiles and local electronic state by Dr. Yan Xin. The largest drawback of the grain boundary enhancement by Ca-doping, large T_c reduction, was renounced by a newly proposed cation substitution, that of Nd. The results suggest significant new opportunity for nanoscale cation segregation engineering in GBs.

References

- [1] A. Gurevich & E. A. Pashitskii, *Phys Rev B* **57**, 13878 (1998).
- [2] A. Schmehl, B. Goetz, R. R. Schulz, C. W. Schneider, H. Bielefeldt, H. Hilgenkamp & J. Mannhart, *Europhys Lett* **47**, 110 (1999).
- [3] G. A. Daniels, A. Gurevich & D. C. Larbalestier, *Appl Phys Lett* **77**, 3251 (2000).
- [4] G. Hammerl, A. Schmehl, R. R. Schulz, B. Goetz, H. Bielefeldt, C. W. Schneider, H. Hilgenkamp & J. Mannhart, *Nature* **407**, 162 (2000).
- [5] X. Song, G. A. Daniels, D. M. Feldmann, A. Gurevich & D. C. Larbalestier, *Nature Materials* **4**, 470 (2005).
- [6] E. Takayamamuromachi, Y. Uchida, M. Ishii, T. Tanaka & K. Kato, *Jpn J Appl Phys* **26**, L1156 (1987).
- [7] P. Lee, in *Engineering Superconductivity*, Wiley-Interscience 2001
- [8] J. L. Tallon, *Physica C* **168**, 85 (1990).
- [9] Y. Tokura, J. B. Torrance, T. C. Huang & A. I. Nazzal, *Phys Rev B* **38**, 7156 (1988).
- [10] J. L. Tallon, C. Bernhard, H. Shaked, R. L. Hitterman & J. D. Jorgensen, *Phys Rev B* **51**, 12911 (1995).
- [11] C. Bernhard & J. L. Tallon, *Phys Rev B* **54**, 10201 (1996).
- [12] M. Merz, N. Nucker, P. Schweiss, S. Schuppler, C. T. Chen, V. Chakarian, J. Freeland, Y. U. Idzerda, M. Klaser, G. Muller-Vogt & T. Wolf, *Phys Rev Lett* **80**, 5192 (1998).
- [13] K. Takita, H. Akinaga, H. Katoh, H. Asano & K. Masuda, *Jpn J Appl Phys* **27**, L67 (1988).
- [14] M. W. Shafer, T. Penney & B. L. Olson, *Phys Rev B* **36**, 4047 (1987).
- [15] M. R. Presland, J. L. Tallon, R. G. Buckley, R. S. Liu & N. E. Flower, *Physica C* **176**, 95 (1991).
- [16] S. E. Babcock & J. L. Vargas, *Annu Rev Mater Sci* **25**, 193 (1995).

- [17] N. D. Browning, M. F. Chisholm, S. J. Pennycook, D. P. Norton & D. H. Lowndes, *Physica C* **212**, 185 (1993).
- [18] M. A. Schofield, M. Beleggia, Y. M. Zhu, K. Guth & C. Jooss, *Phys Rev Lett* **92**, (2004).
- [19] R. F. Klie, J. P. Buban, M. Varela, A. Franceschetti, C. Jooss, Y. Zhu, N. D. Browning, S. T. Pantelides & S. J. Pennycook, *Nature* **435**, 475 (2005).
- [20] A. Gurevich, *Phys Rev B* **46**, 3187 (1992).
- [21] A. Gurevich, *Phys Rev B* **48**, 12857 (1993).
- [22] A. Gurevich, *Phys Rev B* **65**, 214531 (2002).
- [23] A. Diaz, L. Mechin, P. Berghuis & J. E. Evetts, *Phys Rev B* **58**, R2960 (1998).
- [24] A. Diaz, L. Mechin, P. Berghuis & J. E. Evetts, *Phys Rev Lett* **80**, 3855 (1998).
- [25] D. T. Verebelyi, D. K. Christen, R. Feenstra, C. Cantoni, A. Goyal, D. F. Lee, M. Paranthaman, P. N. Arendt, R. F. DePaula, J. R. Groves & C. Prouteau, *Appl Phys Lett* **76**, 1755 (2000).
- [26] A. Gurevich, M. S. Rzchowski, G. Daniels, S. Patnaik, B. M. Hinaus, F. Carillo, F. Tafuri & D. C. Larbalestier, *Phys Rev Lett* **88**, (2002).
- [27] A. K. S. Kumar, T. Itoh, M. Kawasaki & H. Koinuma, *Physica C* **349**, 83 (2001).
- [28] J. L. Macmanus-Driscoll, S. R. Foltyn, Q. X. Jia, H. Wang, A. Serquis, L. Civale, B. Maierov, M. E. Hawley, M. P. Maley & D. E. Peterson, *Nature Materials* **3**, 439 (2004).
- [29] T. Haugan, P. N. Barnes, R. Wheeler, F. Meisenkothen & M. Sumption, *Nature* **430**, 867 (2004).
- [30] R. D. Shannon, *Acta Crystallogr A* **32**, 751 (1976).
- [31] X. Yao, E. Goodilin, Y. Yamada, H. Sato & Y. Shiohara, *Appl Supercond* **6**, 175 (1998).
- [32] A. A. Polyanskii, A. Gurevich, A. E. Pashitski, N. F. Heinig, R. D. Redwing, J. E. Nordman & D. C. Larbalestier, *Phys Rev B* **53**, 8687 (1996).

Chapter V. Sequential ion milling studies of the critical current density in films and coated conductors of YBCO with varying vortex pinning microstructure

V.1 Introduction

An obvious route to high I_c of Coated conductors (CC) is to increase the thickness t of the $\text{YBa}_2\text{Cu}_3\text{O}_{7-x}$ (YBCO) layer, but significant reduction of the critical current density J_c with increasing t has often been observed [1-8] (see chapter I.2.2 and Figure I.6). Whether this reduction is due to fundamental vortex physics or thickness-dependent material microstructure is very often unclear.

The decline of J_c with increasing t for many PLD films [1-8] usually exhibits an inverse-square-root-like dependence $J_c(t) \propto t^{-1/2}$ which levels off above a critical thickness $t_c \sim 1 - 2 \mu\text{m}$ [1-8]. Such a thickness dependence is suggestive of the transition from the two dimensional (2D) collective pinning of rigid vortex lines in films thinner than the longitudinal pinning correlation length l_c to the three dimensional (3D) pinning of deformable vortices at $t > t_c$ (fundamental vortex physics) [9]. It was recently pointed out [10] that t_c can indeed approach a few μm if the 2D collective pinning model incorporates a multi-scale pinning potential appropriate for the strong-pinning second phase precipitates, pores, and correlated defects found in CCs. Strong-pinning defects have a pin interaction range, r_p much greater than the coherence length ξ and produce large plastic deformations of vortices, rather than the small elastic deformations produced by weak, point pins. Thus, this multi-scale pinning model predicts a crossover thickness t_c as large as $\sim 1-2 \mu\text{m}$, in

agreement with the observed $J_c(t)$ dependence of many PLD films [1-7] and qualitatively consistent with many recent studies of the angular dependence of J_c in CCs, which also reveal much evidence for correlated pinning along the c -axis in PLD films [11]. This model also predicts that the magnitudes of J_c and t_c can be very dependent on the specific pinning microstructure and thus on the film growth process.

There are also many reports of microstructures varying across YBCO films, which can also cause a thickness-dependent $J_c(t)$. For example, PLD films often show some microstructural degradation, including loss of epitaxy, reduction of texture (broadening of in-plane texture), and a -axis grain growth as thickness increases beyond $\sim 1 \mu\text{m}$. Liquid is now recognized to be present in many growth modes, even for *in situ* PLD or electron-beam processes [12], as well as for *ex situ* methods involving fluorine-based precursors [12-14]. A strong effect of liquid was observed in an earlier thickness dependent study of J_c in $2 - 3 \mu\text{m}$ thick films grown by the electron-beam BaF_2 deposition route [15] when the *ex situ* conversion conditions produce significant liquid phase [16]. Study of $J_c(t)$ by milling the films to progressively smaller t showed depressed J_c values ($\sim 0.8\text{-}1.2 \text{ MA/cm}^2$) which were also rather independent of t . Electron microscopy showed a very *inhomogeneous* microstructure that changed markedly about half way through the film thickness, permitting the independence of J_c on t to be ascribed to a bimodal, non-uniform distribution of pinning sites that happened to produce a higher J_c in the upper layer [15]. Microstructural effects are also apparent in another recent study by Emergo *et al.* [7] of up-to-3- μm -thick PLD-deposited YBCO on various miscut SrTiO_3 substrates, where different YBCO defect microstructures occur according to the degree of miscut. Although all films showed J_c

falling off with increasing t approximately as $\sim t^{-1/2}$, there was both a diversity of $J_c(t)$ behavior and a wide range of J_c which varied from 0.6-1.4 MA/cm² (77K,0T). In addition, Foltyn *et al.* [17], who studied single-crystal pure YBCO films grown by pulsed laser deposition (PLD) without any added second phase, found that the thickness dependence of the average J_c can result from a decrease of the local J_c , out to a thickness of $\sim 0.65 \mu\text{m}$, followed by a thickness-independent J_c . They ascribed the high J_c at the interface at the CeO₂ cap layer to a 20 nm thick caging array of interface dislocations which strongly enhance local vortex pinning.

In summary, given the increasing variety of experimental evidence for strongly varying $J_c(t)$ behavior and materials-related effects, the relative contributions of physics- and materials-related effects in different types of YBCO films require better understanding of the current-carrying capability of coated conductors. To achieve this goal the thickness dependence of J_c was studied in a few rather different types of YBCO film, including thin ($\sim 300 - 400 \text{ nm}$) PLD YBCO films without any pins added, $\sim 1 \mu\text{m}$ thick PLD YBCO films containing a high density insulating nanoparticle pins, and MOD YBCO films with rather complex microstructure. Different sample sets exhibited a variety of $J_c(t)$ behavior which we have to correlate their microstructure and the nature of vortex pinning occurring in the samples.

V.2 Sample sets

First, three relatively thin YBCO films grown by PLD were studied. One sample was grown directly on single crystal substrates, which provide an almost ideal model

system for investigating the relationship between 2D collective pinning vortex physics and film thickness by minimizing any materials-related issue. Second, an YBCO film with Y211 nanoprecipitates on a SrTiO₃ single crystal substrate made by PLD was investigated. The addition of insulating nanoparticles strongly enhances vortex pinning, and thus should yield a difference J_c thickness dependence compared to the pure PLD films. It will be shown that such precipitates do indeed take YBCO into the very desirable strong 3D pinning regime. The last sample set was three MOD YBCO samples grown on Ni5at.%W RABiTS provided by American Superconductor Corporation. These MOD samples exhibit a rather complex microstructure, including a large amount of porosity, planar stacking faults, and second phase precipitates, which we find consistent with their rather complex J_c thickness dependence.

V.3 Thickness dependence of J_c in PLD YBCO thin films

This section provides a detailed study of $J_c(t)$ of relatively thin PLD-grown YBCO films carefully made on single crystal substrates, which can provide an ideal model system to study vortex physics and film thickness. The thickness dependence of I_c , J_c , T_c , the room temperature resistivity ρ_{300K} , resistivity curve $\rho(T)$, the bulk flux pinning force curve $F_p(H)$, and the microstructures was measured for these PLD films, providing evidence of vortex pinning physics controlling the thickness dependence of J_c . These relatively thin *in situ* PLD-grown films on single crystal substrates with the least materials-related effects showed very clear evidence of 2D collective pinning affected by thermal fluctuations, which a refined collective pinning theory [18] predicts.

V.3.1 Experiments

One sample was grown directly on a single crystal SrTiO₃ (STO) substrate with no miscut, while the two other samples were grown on 2° miscut (La_{0.30}Sr_{0.70})(Al_{0.65}Ta_{0.35})O₃ (LSAT) substrates, while the growth was monitored by high pressure reflection energy electron diffraction (RHEED). The growth temperature for these samples was ~ 850 °C, which is higher than usual YBCO growth conditions. Indeed, the miscut substrates and the high growth temperature induce step flow growth mode [19], which results in best microstructure and surface morphology of thin films. These films were grown in Prof. Chang-Beom Eom's group by Dr. Kyoungjin Choi and Dr. Junghoon Choi.

Bridge 90 μm wide and 1000 μm long was patterned on the YBCO film on STO (CHOI23-1) and bridges 95 μm wide and 500 μm long were patterned on the 2° miscut (La_{0.30}Sr_{0.70})(Al_{0.65}Ta_{0.35})O₃ (LSAT) substrates (CBE401+/CBE415||) by Nd-YAG (Nd-doped yttrium aluminum garnet) laser ablation. The bridge was directed so that current flowed perpendicular to the miscut direction for CBE401+, while the bridge on CBE415|| was cut to make current flow parallel to the miscut direction. Each link was thinned with 500eV Ar ions impinging at 45° while the sample was cooled to ~ 230 K to avoid ion damage. For these PLD films, the YBCO etch rate was calibrated to be 10 nm/min by measuring the thickness of each milled sample with a Tencor profilometer. The voltage-current $V-I$ characteristics were measured at 77 K and at other various temperatures after each milling step with a four-point configuration for magnetic fields up to the irreversibility field applied perpendicular to the film surface. Angular dependent J_c measurements $J_c(\phi)$

were often performed as well after each milling. J_c values were determined at 1 $\mu\text{V}/\text{cm}$ electric field criterion. Resistivity as a function of temperature, $\rho(T)$, was measured during sample cooldown and T_c was defined as the onset of zero resistance ($\sim 1\%$ of normal state resistance).

Table. V.1 The key properties of the three PLD samples at full thickness.

	Substrate	Miscut direction	Original t (nm)	T_c (K)	$J_c(0T,77K)$ (MA/cm ²)	$I_c^*(0T,77K)$ (A/cm-width)
CHOI23-1	Single crystal STO	N/A	280	87	2.8	79
CBE401+	Single crystal 2° miscut LSAT	current+miscut	285	91	3.9	112
CBE415	Single crystal 2° miscut LSAT	current miscut	390	90	2.3	89

V.3.2 Results

The key properties of the three samples at their full thickness are shown in Table V.1. CHOI23-1 on single crystal SrTiO₃ substrate had full thickness of 280 nm, T_c of 87 K, $J_c(0T,77K)$ of 2.8 MA/cm², and $I_c^*(0T,77K)$ of 79 A/cm-width. CBE401+ on 2° miscut LSAT substrate had 285 nm, 91K, 3.9 MA/cm², and 112 A/cm-width, while CBE415|| on the same LSAT substrate had 390 nm, 90K, 2.3 MA/cm², and 89 A/cm-width. As mentioned earlier, the bridge on CBE401+ was patterned to make the current flow perpendicular to the substrate miscut direction, and CBE415|| the current flows parallel to the miscut direction.

Figure V.1(a) shows typical $J_c(H)$ plots at 77 K when the field was applied perpendicular to the film surface. The observed J_c at self-field (2.3 – 3.9 MA/cm²) and the irreversibility fields H_{irr} (5.8 – 7.8 T @ 100 A/cm²) suggest the films are of good quality. The slightly lower H_{irr} of CHOI23-1 is due to its lower T_c of 87 K, which we ascribe to its oxygen-underdoped nature which will be addressed below. Figure V.1(b) presents bulk flux pinning force curves $F_p(H) = \mu_0 H \times J_c(H)$ for the three samples. The maximum pinning forces $F_{p,max}$ are ~ 2.0 GN/m³ for CHOI23-1 and ~ 2.6 GN/m³ for CBE401+/CBE415||, which are rather low compared with the strong pinning samples of 4-8 GN/m³ obtained by PLD growth at lower temperatures

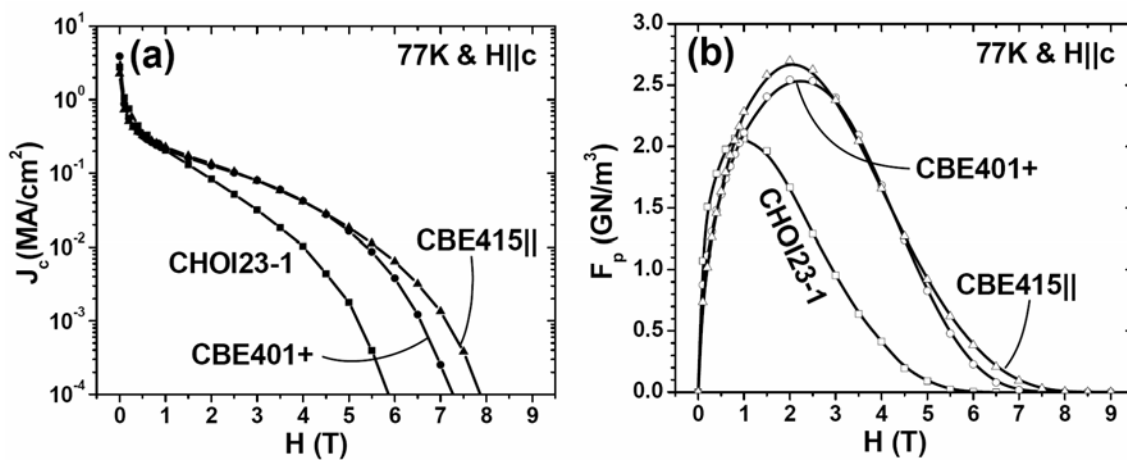


Figure V.1 (a) The critical current density vs. applied field $J_c(H)$ for the three samples at 77K when the field is applied perpendicular to the film surface. CHOI23-1 exhibits a slightly lower irreversibility field H_{irr} due to its underdoped lower T_c value, while the other two samples show rather typical $H_{irr} \sim 7 - 8$ Tesla. These are the typical shapes of $J_c(H)$. (b) The bulk flux pinning force plot $F_p(H)$, where bulk flux pinning force $F_p = \mu_0 H \times J_c$, for the three sample at 77K. CBE401+ and CBE415|| exhibit rather similar behavior.

The room temperature resistivity ρ_{300K} , the critical temperature T_c , and the resistivity curve $\rho(T)$ shape at various thicknesses for each sample are shown in Figure V.2. The room temperature resistivity value of CHOI23-1 and CBE401+ are very low of 200 – 250 $\mu\Omega$ cm, comparable to the very dense and good quality YBCO films [20], suggesting the films is in very dense and good quality. The ρ_{300K} value of CBE415|| is rather higher ~ 360 $\mu\Omega$ cm, since it contains a component of c-axis current path that results from current flow across miscut steps. Indeed, the positive intercepts of the extrapolation of the linear regions of $\rho(T)$ (dashed line in Fig. V.2(i)) of CBE415|| are due to this c-axis component. Nevertheless, the three samples show uniform ρ_{300K} through thickness. The T_c values of CHOI23-1 are somewhat low as 87 K due to the slight oxygen-underdoping, as judged from its $\rho(T)$ curve, which has a positive intercept when extrapolating the linear $\rho(T)$ portion [21] (Figure V.2(c)). For CBE401+ and CBE415||, the T_c values of 91 K and 90 K are high, respectively. For CBE401+, the zero temperature intercept of the $\rho(T)$ extrapolation shows optimal oxygen doping of the YBCO film [21]. The T_c values of these three samples are relatively constant through thickness. It should be noted that the $\rho(T)$ curve shapes also remain the same through thickness for each sample, strongly suggesting no change in the oxygenation state of each film during the milling process.

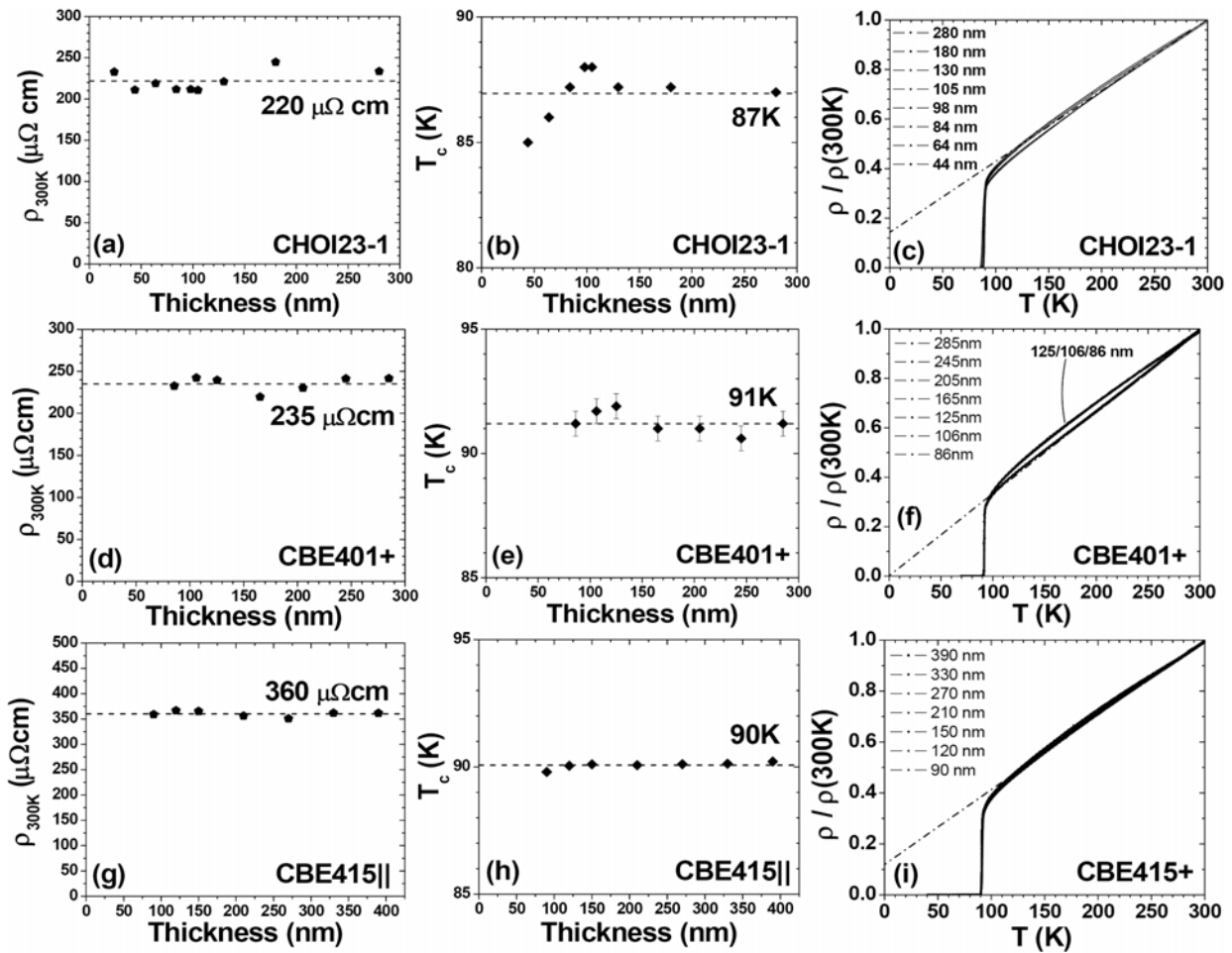


Figure V.2 (a)(d)(g) The room temperature resistivity ρ_{300K} vs. thickness (b)(e)(h) T_c vs. thickness (c)(f)(i) The normalized resistivity curve $\rho(T)$ as a function of thickness for (a)(b)(c) CHOI23-1, (d)(e)(f) CBE401+, and (g)(h)(i) CBE415||.

Figure V.3 shows the critical current per unit width I_c^* vs. the measured thickness at various fields and temperatures. The common behavior observed in the three is *the square root dependence of $I_c^*(t)$ with the non-zero intercept t^* of the extrapolation of the square-root dependence $t^{0.5}$* . Indeed, this square root dependence in $I_c^*(t)$ suggests 2D collective pinning, and was observed for all three samples at all temperatures and fields studied. Another very interesting behavior is that the non-zero intercept values t^* increases as

temperature and field increase, as summarized in Table V.2. At smaller thickness less than t^* , $I_c^*(t)$ shows a rather linear relationship, while this feature does not appear in the plots for CBE401+, since the sample blew up after testing at 86 nm thickness.

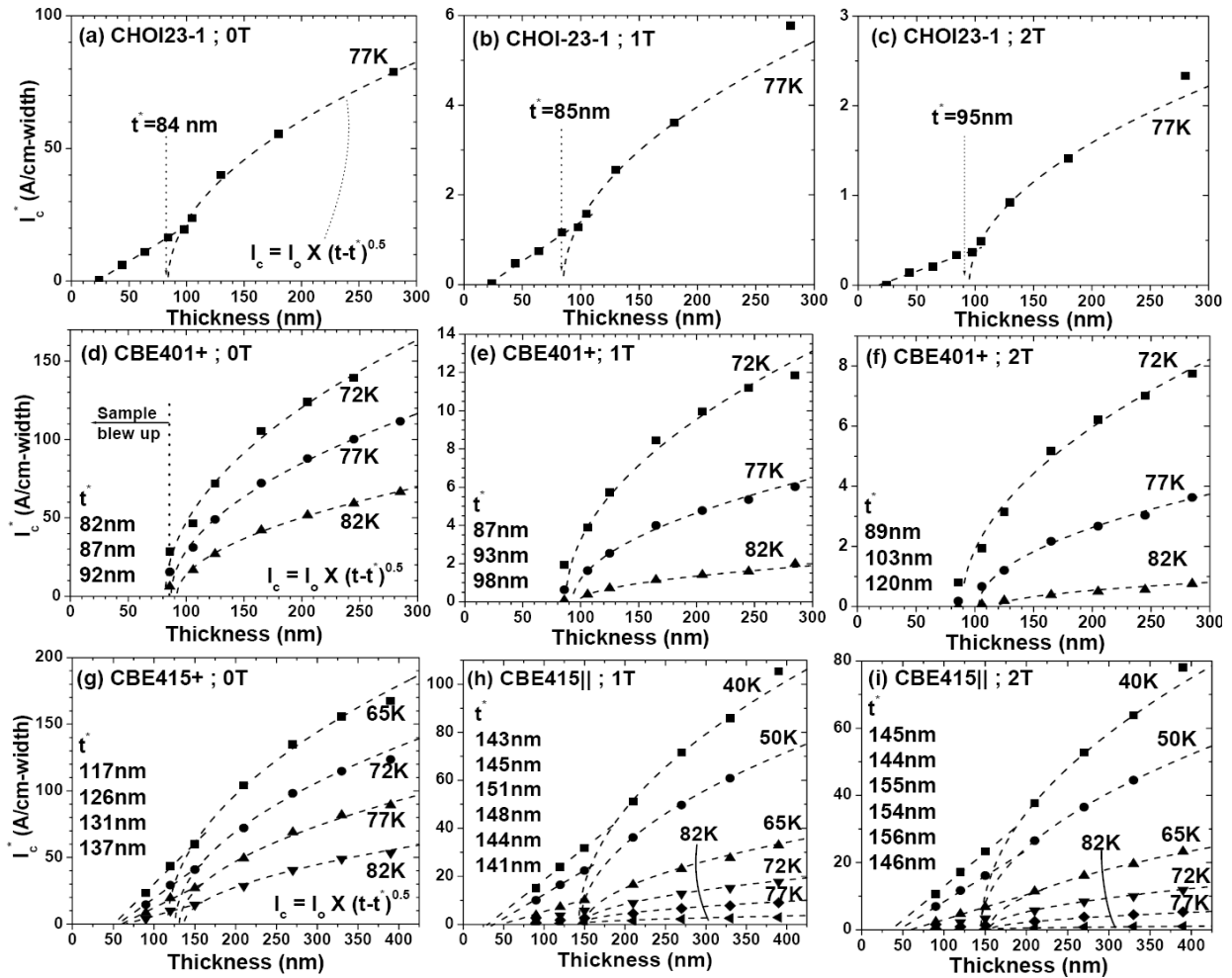


Figure V.3 The critical current per unit width I_c^* vs. the measured thickness for the three samples at some different temperatures and fields. All show two common behaviors – square root dependence of $I_c^*(t)$ and non-zero intercepts t^* of zero I_c . CHOI23-1 and CBE415+ exhibit linear $I_c^*(t)$ in the very thin regime. For CBE401+, the sample blew up below 86 nm.

Table V.2 The non-zero intercept t^* values shown in Fig. V.3 for the three samples at various temperatures and fields. The t^* values change systematically – they increase as temperature and field increases.

	CHOI23-1	CBE401+			CBE401					
t^* (nm)	72K	72K	77K	82K	40K	50K	65K	72K	77K	82K
0T	84	82	87	92			117	126	131	137
1T	85	87	93	98	143	145	151	148	144	141
2T	95	89	103	120	145	144	155	154	156	146
3T	100	99	116		148	148	158	162	163	
4T	110	112	121		149	142	166	171	169	
5T		118			163	152	173	177	173	

Figure V.4 shows $J_c(t)$ for CBE401+ at a few different temperatures and magnetic fields. Each $J_c(t)$ shows a maximum value at a certain thickness, which is due to the non-zero intercepts in $I_c^*(t)$ in Fig. V.3. For example, at 0 T and 77 K, J_c shows its maximum of 4.3 MA/cm² at 160 nm thickness. As the field and temperature increases, the peak moves toward high field regime. At high temperature and high field (e.g. 2T/82K or 4T/77K), J_c only decreases as thickness decreases within the observed thickness regime.

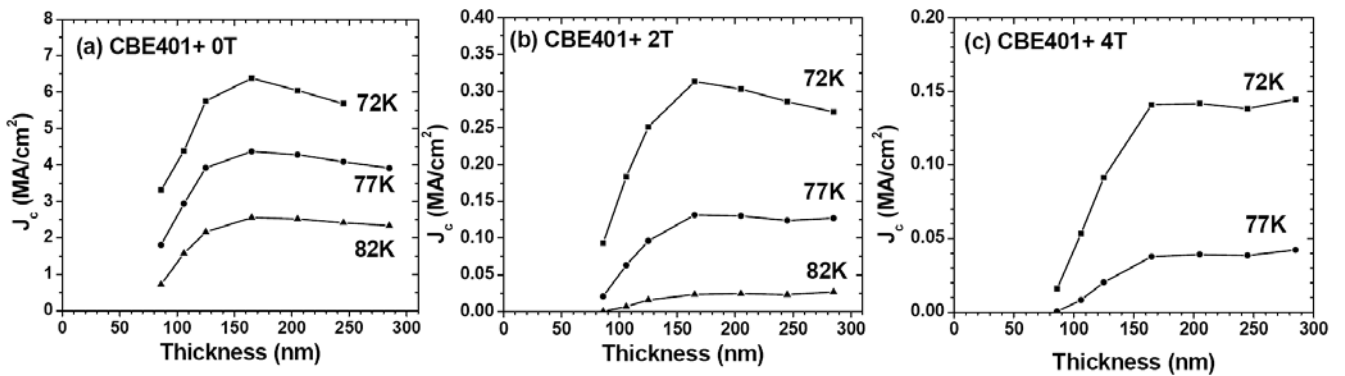


Figure V.4 The critical current density vs. the thickness $J_c(t)$ for CBE401+ at (a) 0, (b) 2, and (c) 4 T. The $J_c(t)$ exhibit a maximum at a certain thickness due to the non-zero intercepts observed in Fig. V.3. However, J_c at high field (4T; Fig. V.4(c)) increases as thickness increases in the measured thickness regime.

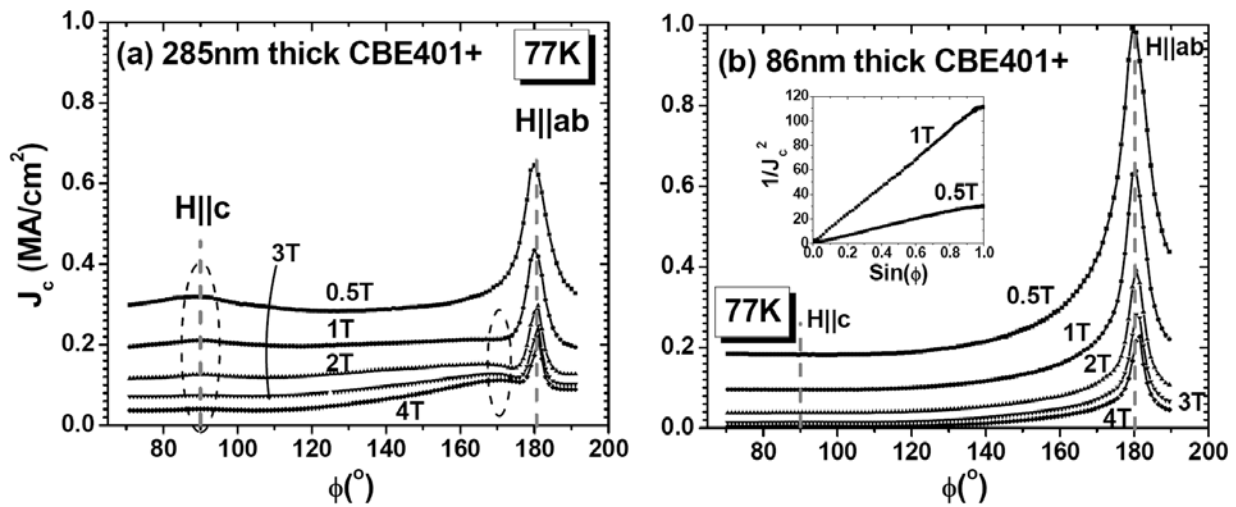


Figure V.5 Angular dependent J_c measurement results $J_c(\phi)$ of CBE401+ sample for various fields at (a) its full thickness 285 nm, and (b) at its minimum thickness 86 nm. In the 285 nm thick film, the correlated pinning peaks are clearly seen. The correlated peaks at around 90° (H||c) are very typical for PLD, which has a columnar grain structures. The humps around 170° are believed due to the substrate miscut. However, those all disappear in very thin 86 nm thick film, suggesting no correlated pinning takes account here. Note that the 86 nm is less than t^* values of this sample at these fields (87, 93, 103, and 116 nm for 0, 1, 2, 3, and 4T). The inset shows $1/J_c^2$ vs. $\sin(\phi)$ at 0.5 and 1T. The linear relationship may be associated only with surface pinning – not with any correlated pinning.

The angular J_c dependence of CBE401+ (285nm) at full thickness at various fields is shown in Figure V.5(a). The data exhibit relatively strong c-axis peaks and correlated pinning peaks around 170° . The strong c-axis peaks are very typical for PLD-grown YBCO films with columnar microstructures [11], while the correlated pinning peaks around 170° are due to correlated pins caused by the miscut substrate (note that they are absent around 190° which is symmetric position against H||ab of 180°). However, in contrast, the angular

J_c dependence of (milled) 86nm-thick CBE401+ shown in Figure V.5(b) exhibits neither c-axis peaks nor correlated pinning peaks. It is worth recalling here that the 86 nm-thick film is in the regime where the $I_c^*(t)$ dependence is beyond that controlled by the square-root behavior (Table V.2; the non-zero intercept t^* of CBE401+ was 87, 93, 103, and 116 nm for 0, 1, 2, 3, and 4 T, respectively). The inset of Figure V.5(b) shows $1/J_c^2$ vs. $\sin(\phi)$ for 0.5 and 1 T of 86 nm-thick film. It is interesting that the plots exhibit a linear relationship. This behavior is consistent with surface pinning, which is to be expected in this domain where the film thickness (86 nm) is much less than the London penetration depth $\lambda_L \sim 400$ nm at 77K. Figure V.6 shows the gradual disappearance of the correlated pinning peaks as the film being thinned more explicitly for CBE401+. It is much clearer that the c-axis correlated peak becomes weaker as thinned, while it completely disappears at the 86 nm thick film.

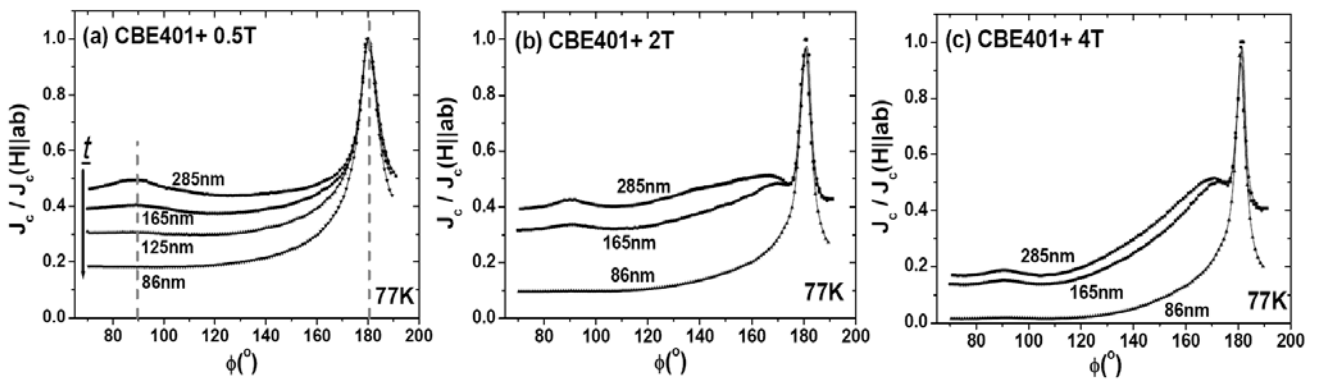


Figure V.6 Angular dependent $J_c(\phi)$ of the CBE401+ sample at (a) 0.5, (b) 2, and (c) 4 T at different thicknesses. At 0.5 T, the c-axis correlated pinning peak progressively disappears as the film is thinned – it is gone completely at 86 thickness. (b)(c) show disappearance of c-axis correlated pinning peaks and miscut-correlated pinning peaks as well at 86 thickness.

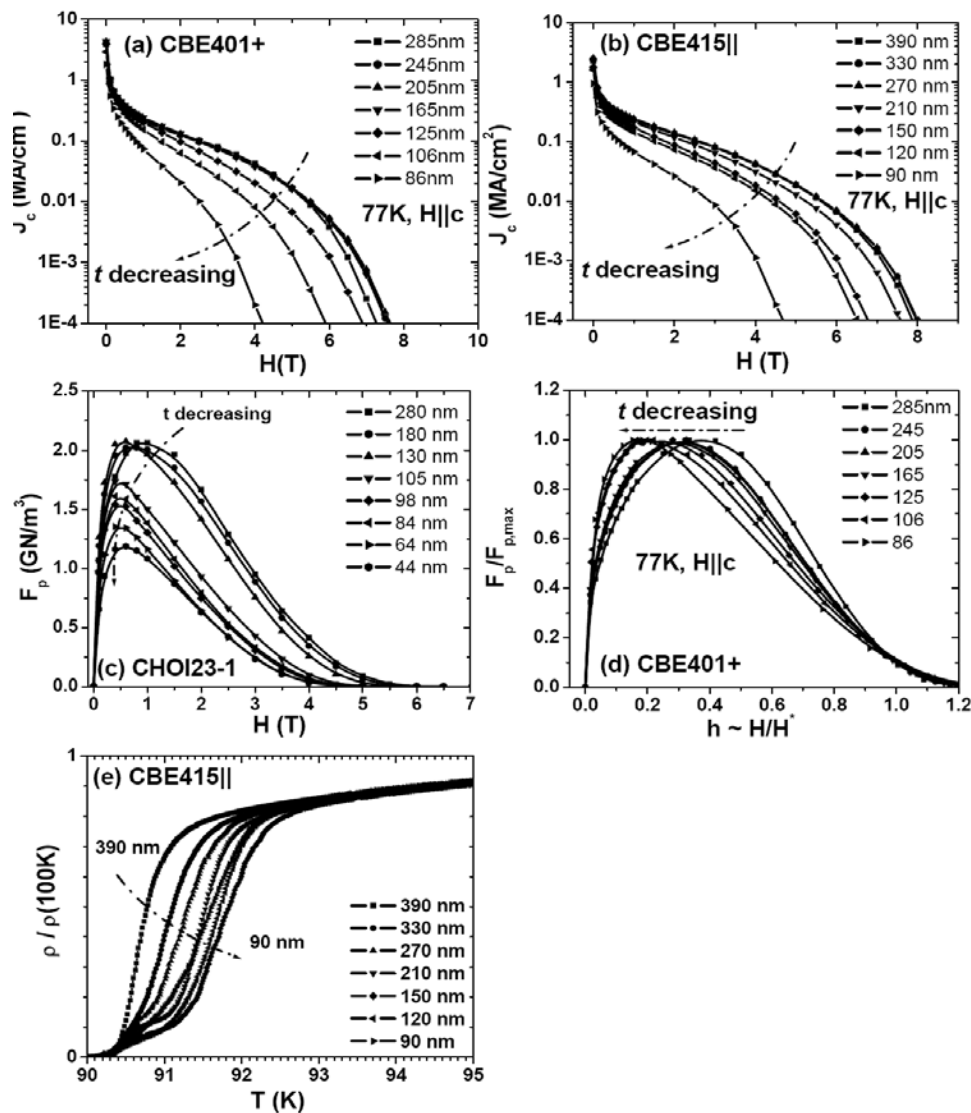


Figure V.7 (a)(b) The critical current density vs. applied field $J_c(H)$ plots for various thicknesses of (a) CBE401+ and (b) CBE415||. A few thicker films show similar $J_c(H)$, but the irreversibility field decreases progressively as the film was thinned. (c) The bulk flux pinning force plots for various thicknesses of CHOI23-1. The maximum pinning force $F_{p,max}$ decreases and the maximum peak position moves toward lower field as the film was thinned. (d) The normalized flux pinning force plots for various thicknesses of CBE401+. The position of $F_{p,max}$ moves towards the low field regime as the film is thinned. (e) The normalized resistivity plots for various thicknesses of CBE415||. The superconducting transition width becomes broader as the film being thinned.

Figure V.7 shows many additional evidences of changes in the superconducting properties as the films are thinned. First of all, the irreversibility field H_{irr} dramatically decreases, especially below ~ 150 nm thickness as shown in Figs. V.7(a) and (b) for CBE401+ and CBE415||, respectively. Figs. V.7(c) and (d) indicate that the shape of flux pinning force curves also changes. The maximum pinning force $F_{p,max}$ decreases and the position of $F_{p,max}$ moves toward low fields as the film thickness decreases for CHOI23-1, as shown in Fig. V.7(c). The normalized flux pinning force curves of CBE410+ at various thicknesses is shown in Fig. V.7(d), showing that the maximum peak position moves toward low fields too. In addition, the broadening of the T_c transition as the film is thinned is seen and shown in Fig. V.7(e) for CBE415||.

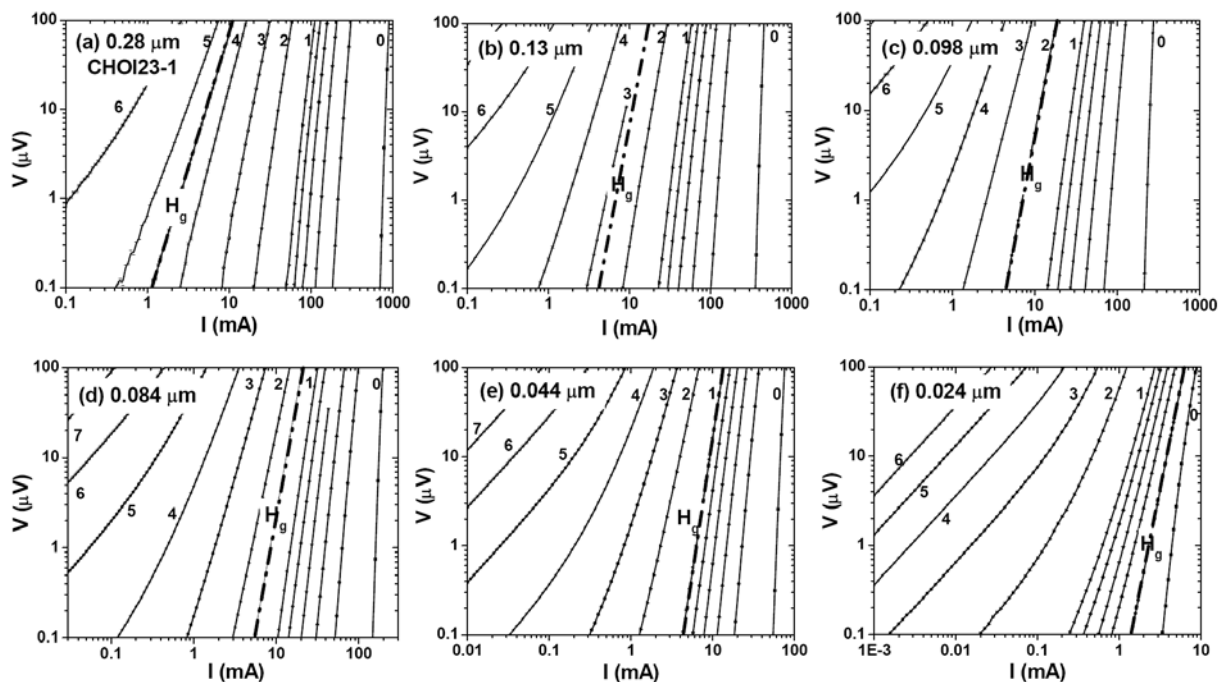


Figure V.8 The voltage-current V - I characteristics for CHOI23-1 for various thicknesses. The glass transition field H_g decreases as the thickness decreases.

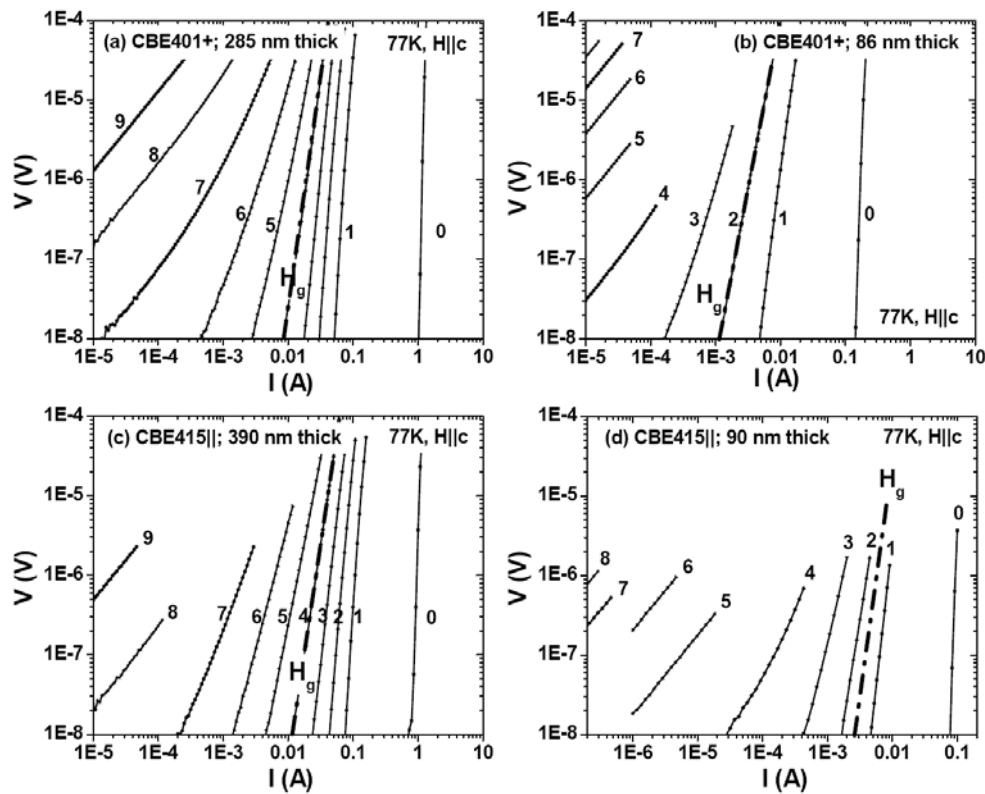


Figure V.9 The voltage-current V - I characteristics for (a)(b) CBE401+ and (c)(d) CBE415|| at (a)(c) their full thickness and (b)(d) their smallest thickness. The glass transition field H_g decreases as thickness decreases.

The change in superconducting properties is explicitly indicated by change in the voltage-current V - I characteristics. The V - I characteristics of CHOI23-1 at various thicknesses are shown in Figure V.8. Each plot shows a thick dashed line indicating the glass transition irreversibility field H_g where the curvature of the V - I characteristics in the log-log plot changes sign. For the original thickness, CHOI23-1 (0.28 μm) had H_g of ~ 4 T, which became progressively smaller as the film was thinned. For 0.044- μm -thick films, the H_g is merely 1 T. It becomes even smaller ~ 0.2 T for the thinnest 0.024- μm -thick films.

Figure V.9 indicates this change in the V-I characteristics for CBE401+ and CBE415|| at their full thickness and the smallest thickness. It is also clear for these two samples that H_g decreases from ~ 4 T to less than ~ 2 T as the film is thinned.

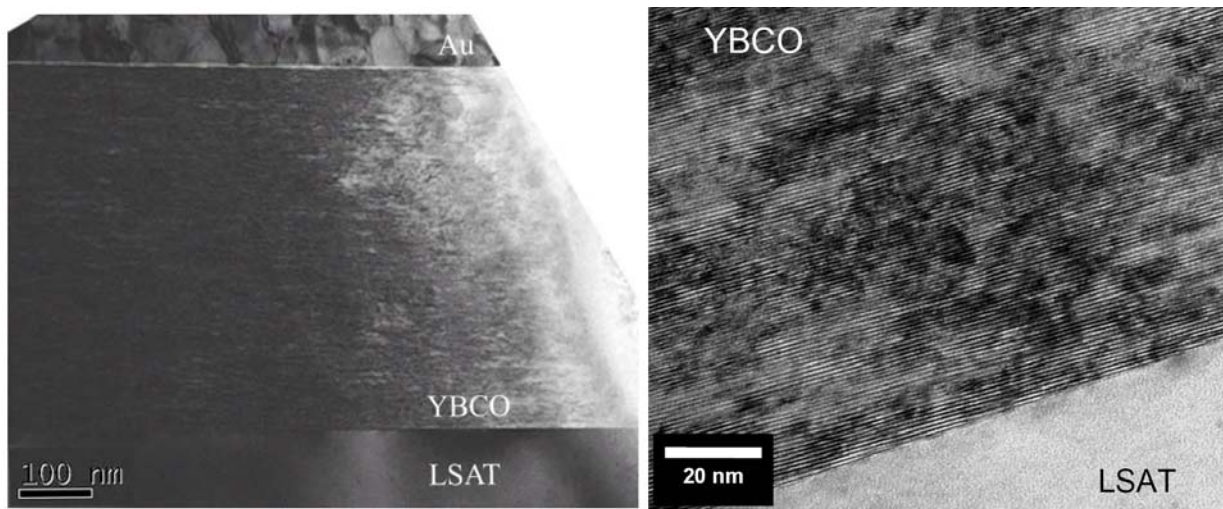


Figure V.10 (a) Low magnification TEM image of a sister sample grown at the same condition on the 2° miscut LSAT substrate. The micro-structure of the YBCO seems uniform through the thickness. (b) High resolution TEM image near the interface. Strain contrast is seen due to the stacking faults and dislocation parallel to the a-b plane. There are no threading dislocations or continuous anti-phase boundary going perpendicular through the film. Strain contrast generated by the short-length stacking faults introduced by the miscut steps (TEM images were provided by Dr. Fumitake Kametami).

Figure V.10 shows the cross-sectional transmission electron microscopy (TEM) images of the sister sample grown at the same condition on the 2° miscut LSAT substrate. The images were taken by Dr. Fumitake Kametani. Fig. V.10(a) indicates that the microstructure is indeed quite uniform through the thickness. Fig. V.10(b) shows high

resolution TEM images near the interface region. Much strain contrast is seen due to the stacking faults and dislocations parallel to the ab-plane. There are no threading dislocations or continuous anti-phase boundary going perpendicular to the film plane, which is usually seen in PLD films. This is probably due to the step flow growth mode resulting from the high growth temperature of 850 °C and the miscut substrate. From the closer investigation, it was found that all stacking faults have short length in the ab-plane. However, no distinctive evidence of the source of the correlated pinning seen at $\sim 170^\circ$ (Figs. V.5 and V.6) in the $J_c(\phi)$ plots is found in these TEM images.

V.3.3 Discussion

Relatively thin PLD films on single crystal substrates exhibited high through-thickness uniformity in their normal state properties and oxygenation state, while cross-sectional TEM investigations confirmed their good microstructural uniformity through thickness, as well as the absence of major pinning features including precipitates, threading dislocations, and anti-phase boundaries. These properties mean that we can exclude variable through-thickness microstructure as the source of the thickness dependence of J_c , which makes this work valid for tests of vortex physics dimensionality. The main result of our present work is that the films showed two distinctive behaviors in the $I_c^*(t)$; (i) *the square root dependent behavior $I_c^* \sim t^{0.5}$* and (ii) *the systematic changes of the non-zero intercept t^* with field and temperature*. The observed square root dependence of $I_c^*(t)$ is a strong evidence of 2D collective pinning. The non-zero intercept t^* is believed to be due to increase of thermal fluctuation effect at small thickness. The increase of t^* value with field

and temperature shown in Table V.2 is a solid support for this thermal fluctuation effect, since thermal fluctuation depinning is expected to become larger as field and temperature increases.

In addition, angular J_c measurements at different thicknesses clearly show that correlated pinning disappears as the thermal fluctuations depin more effectively at small thickness. There were additional evidences of the thermal fluctuation, such as the decrease of H_{irr} and H_g , the change in the shape of $F_p(H)$, and the broadening of T_c transition width at small thickness. We conclude that the single crystal PLD films with no distinctive pinning structures and uniform through-thickness microstructure demonstrate weak 2D collective pinning behavior accompanied by strong thermal fluctuation depinning at small thicknesses.

Many previous $J_c(t)$ data sets in the literature [1,4,7,15,22] were obtained from films with some degree of through-thickness microstructural variation, thus making difficult to deconvolute the relative contributions of physics- and materials-related effects on the J_c -thickness-dependence. In this work, the TEM observation provided a direct evidence of uniform microstructure with no distinctive pinning centers, while the three films exhibited uniform ρ_{300K} and T_c , and oxygenation state, suggesting that the films have very uniform normal-state and superconducting-state properties through thickness. Pinning in these PLD films may be provided only by dense but comparatively weak defects, such as clusters of oxygen vacancies or cation disorder, which are mostly undetected by TEM. Thus, the present samples are valid for examination of the physics of vortex dimensionality without materials-related effect.

All samples clearly indicated $I_c^* \sim t^{1/2}$ (corresponding to $J_c \sim t^{-1/2}$) in any temperature and field measured up to the full thickness of 0.3-0.4 μm , as shown in Fig. V.3, which is the unambiguous evidence of 2D collective pinning. The 2D collective pinning behavior results in J_c reduction at large thickness. However, the non-zero intercept t^* of the extrapolation of the square root dependence portion is believed due to thermal fluctuation depinning. Thermal fluctuation effect is expected to grow larger at small thickness since the activation energy of thermally activated vortex motion decreases as film thickness decreases. The t^* values change systematically, since the thermal fluctuations become larger as field and temperature increases (Thus, thermal fluctuation especially reduces J_c at small thickness and high field/temperature). Indeed, large thermal fluctuation effects at small thickness are well emphasized in the $J_c(\phi)$ results which show loss of c-axis peaks and correlated pinning peaks at smallest thicknesses, as shown in Figs. V.5 and V.6. When the thermal vibrations become large enough, the destruction of the Abrikosov vortex lattice occurs (thermal fluctuation depinning), causing extra voltage dissipations. This causes rounding of the depinning transition which controls the V-I characteristics around I_c . Thus, reductions of H_{irr} , H_g , I_c , and J_c are all expected. There were other multiple evidences of the thermal fluctuations presented in Fig. 7, such as the decrease of the irreversibility field H_{irr} , the change in the shape of bulk flux pinning force curves $F_p(H)$, and the broadening of the T_c transition width at small thickness. Thermal fluctuations are shown in the V-I curves, of Figs. V.8 and V.9, which clearly exhibit the extra dissipation and the reduction of H_g at small thickness.

The large thermal fluctuation effects, which appear at $t < \sim 100$ nm, and the 2D collective pinning behavior suggests the pinning structures in these PLD films are weak. The major defect structure found is short stacking faults, and there were no threading dislocations or continuous anti-phase boundaries. The 2D collective pinning is estimated using the theory for a rigid vortex line in a thin film where the bending distortions of the vortex are negligible [9,10]. If such pins are distributed randomly with mean density $n_i = 1/d^3$ and each pin exerts a pinning force f_p with interaction radius r_p , the net pinning force on the vortex line equals $F_p = f_p N^{1/2}$ where $N = \pi r_p^2/d^3$ is the total number of pins in a cylinder of radius r_p and height t . Here the factor $N^{1/2}$ reflects the fact that a vortex adjusts its position to find a local minimum in the random potential produced by statistical fluctuations of all the defects. Balancing F_p against the total Lorentz force, $F_L = \phi_0 t J_c$, we obtain

$$J_c \cong \frac{\pi^{1/2} f_p r_p}{\phi_0 d^{3/2} t^{1/2}} \quad (\text{V.1})$$

Eq. V.1, which gives the inverse square root dependence $J_c \propto t^{-1/2}$ (thus, $I_c \propto t^{-1/2}$) observed for the films (when the thermal fluctuation effect ignored), can be used to estimate the mean pin spacing d , which would provide self-field values of $J_c \sim 2.3\text{-}3.9$ MA/cm² in $\sim 300\text{-}400$ nm thick PLD films at 77 K. Taking $\xi = 4$ nm, $t = 300\text{-}400$ nm, $J_d = 40$ MA/cm², and assuming core pinning for which $f_p \sim \phi_0 \xi J_d$ and $r_p \sim \xi$, we estimate the mean spacing $d \sim \xi (J_d/J_c)^{2/3} (\xi/t)^{1/3} \sim 6\text{-}8$ nm, qualitatively consistent with earlier estimates of the pin separation d by Hylton and Beasley [23].

V.4 Thickness dependence of J_c in YBCO film containing a high density of insulating, vortex-pinning nano-precipitates

The motivation of the second part of my study is to investigate how the changes in pinning microstructure affect the J_c thickness dependence. The hypothesis was my expectation that the addition of insulating nanoparticles should yield a thickness-independent J_c , since they would provide strong vortex pinning that should enable each vortex segment to be pinned independently. In this section, it is shown that such precipitates do indeed take YBCO into this very desirable strong 3D pinning regime, in which the longitudinal pinning correlation length is much shorter than the film thickness, and the local J_c is then independent of t . In principle, this permits a high and a thickness-independent J_c in thick films, provided that thickness degradation of the current-carrying cross-section and the second-phase pinning structure is avoided.

V.4.1 Experiments

The sample was provided by Dr. Tim Haugan, Air Force Research Laboratory at our request, in order to make an explicit test of the above hypothesis. The Y211 was introduced by alternate deposition of layers of Y211 (~0.8 nm) and YBCO (~16.5 nm) [24]. The Y211 particles grow with orientation $(010)_{211} // (001)_{Y123}$. The Y211 to Y123 lattice mismatch is -7% to +4% for the ab-plane and about +18% with respect to the c-axis [24]. These mismatches cause localized strain fields around the nanoparticles, particularly extending in the c-axis direction [24]. At our lab, a 50 μm wide \times 400 μm long bridge for transport I_c measurements was cut by Nd-YAG (Yttrium Aluminum Garnet) laser ablation.

This bridge was then sequentially thinned with 500eV Ar ions impinging at 45° while the sample was cooled to ~230 K. After each milling step, J_c was measured with a four-probe configuration at 77 K for magnetic fields up to 10 T applied perpendicular to the film surface. The J_c values were determined at the 1 $\mu\text{V}/\text{cm}$ electric field criterion. The thickness of the YBCO was originally 1.0 μm , and the thickness of each thinned sample was measured with a Tencor profilometer. Cross-section TEM/HREM imaging was performed in a Philips CM200UT by Dr. Fumitake Kametani.

V.4.2 Results

This Y211-dispersed-YBCO sample exhibited a full-thickness $J_c(0\text{T},77\text{K})$ of 3.4 MA/cm^2 , a critical temperature T_c of 90.0 K defined at the onset of resistance, and an irreversibility field $H_{\text{irr}}(77\text{K})$ of 8.8 T measured at $J_c=100\text{A}/\text{cm}^2$. The maximum pinning force $F_{p,\text{max}} \sim 8.8 \text{ GN}/\text{m}^3$ was 2-4 times higher than typical PLD films, even though the self-field J_c was no larger than conventional precipitate-free PLD YBCO. Figure V.11 shows the $J_c(t)$ data plotted both as a function of the average residual thickness and as a histogram of the incremental $J_{c,\text{incr}}$ deduced from the incremental change in I_c and t of each milling step. The critical current per unit width I_c^* exhibits a linear dependence on t , which extrapolates to a non-zero value of I_c at zero thickness. Such a linear dependence is inconsistent with the 2D-3D collective pinning scenario. The data unambiguously show a rather uniform local J_c in the bulk of the film, although there is a thin, higher J_c layer near the substrate. The average $J_c(d) = J_{c0}(1 + d_0/d)$ thus increases as the film thickness decreases because of the very high J_c (7.1 MA/cm^2 , 60 nm thick) layer at the interface. The pinning nanostructure in this highly-defected interface layer will be addressed below.

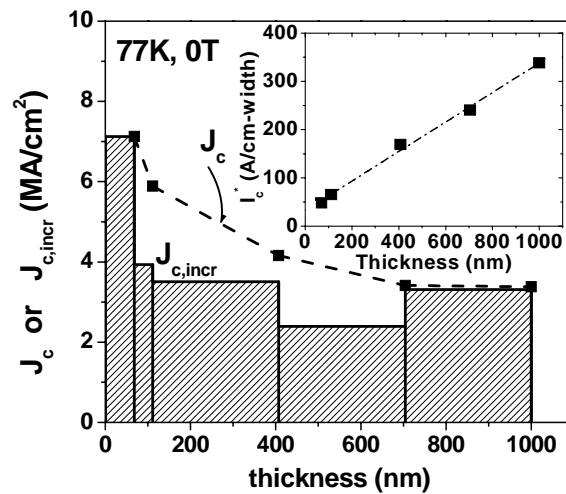


Figure V.11 $J_c(t)$ data as a function of the residual thickness. The histogram shows the incremental $J_{c,incr}$ deduced from each milling step, while the inset shows a linear thickness dependence of the critical current per unit width I_c^* (0T, 77K).

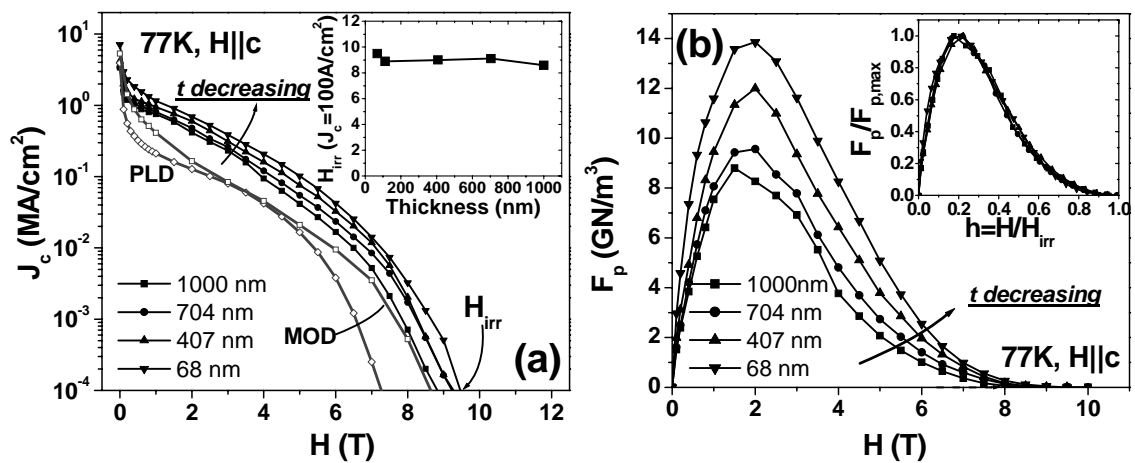


Figure V.12 (a) $J_c(H)$ at 77K for different thicknesses. In addition, $J_c(H)$ curves for a 280 nm YBCO film grown by PLD on a single crystal LSAT substrate and for a 1 μm YBCO film made by MOD on a single YSZ crystal are shown for comparison. Inset shows the irreversibility field H_{irr} , determined at $J_c=100\text{MA}/\text{cm}^2$, as a function of thickness. (b) Bulk pinning force plot $F_p(H)$ for different thicknesses. Inset shows that the normalized pinning force curves $F_p(H)/F_{p,max} = f(H/H_{irr})$ which do not change shape at all as thickness changes.

Magnetic field dependences of $J_c(H, 77K)$ for different thicknesses are shown in Figure V.12(a). The overall shape of the $J_c(H)$ curves is rather insensitive to t , although the magnitude does increase at small t due to the high J_c interface layer. For comparison, the $J_c(H)$ curves for a 280 nm YBCO film grown by PLD on a single crystal $(La_{0.30}Sr_{0.70})(Al_{0.65}Ta_{0.35})O_3$ (LSAT) substrate [25] and for $\sim 1 \mu m$ YBCO film grown by MOD on a single crystal yttrium-stabilized zirconia (YSZ) [26] are also shown. Neither the PLD nor MOD film had deliberately added second phase particles, although the MOD films do have a complex pinning microstructure that contains pores, stacking faults and Y_2O_3 particles. The strong vortex pinning of the present sample results in much higher J_c values at all fields above a few tenths of a Tesla, although the self-field J_c values of all 3 samples vary only from 3.4 to 5.3 A/cm². The inset of Fig. V.12(a) shows the irreversibility fields H_{irr} , determined at $J_c=100A/cm^2$. They are significantly higher than for the MOD (8.6 T) and PLD (7.2 T) films and are essentially independent of t , except in the high J_c interface layer, where H_{irr} rises from 8.8 to 9.5 T. The thickness-dependent bulk flux pinning force curves are shown in Figure V.12(b). The magnitude of the $F_{p,max}$ increases as t decreases because of the contribution of the strong-pinning interface layer. But even at full thickness, $F_{p,max} \sim 8.8 GN/m^3$ is 4 times higher than 2.2 GN/m³ of the previous studied thin PLD sample without pinning defects grown on LSAT (see Figure V.1(b)), and twice higher than the 4.1 GN/m³ of the 1 μm MOD sample (whose details will be shown in the following section V.5), while at the thinnest layer measured, $F_{p,max}$ reaches 13.8 GN/m³. However, the inset of Fig. V.12(b) shows that the normalized pinning forces $F_p/F_{p,max}$ plotted against the

reduced fields H/H_{irr} are essentially independent of t , consistent with our conclusion that the pinning mechanisms are independent of t .

Figure V.13 shows cross-sectional TEM images which reveal a high density of Y211 precipitates, which tend to cluster on stacking faults. Their separation is much smaller (5-10nm) within the 60 nm interface layer than through the rest of the film (~30nm). Within each thickness slice, the Y211 precipitates are rather randomly distributed in the YBCO matrix. Although the typical sizes of the Y211 precipitates are ~ 4 - 8 nm, the effective size including strain field is ~ 10 nm and almost spherical in shape, while their average spacing is ~30 nm along the c -axis, and ~10 nm in the ab -plane. Their volume fraction, nominally ~ 5 %, increases to ~ 10 vol.% when the strained regions surrounding the Y211 are included. It is especially clear from Fig. V.13(b) that Y211 precipitates tangle with the stacking faults and their associated partial dislocations near the interface. The YBCO matrix in this interface layer shows much evidence for stacking faults and partial dislocations cut into short segments by the Y211 precipitates. Fig. V.13(b) also indicates that there are several threading dislocations running normal to the interface, which are cut into short segments by the stacking faults, making a dense 3D defect network near the interface, a structure which is consistent with the almost twice stronger pinning near the interface.

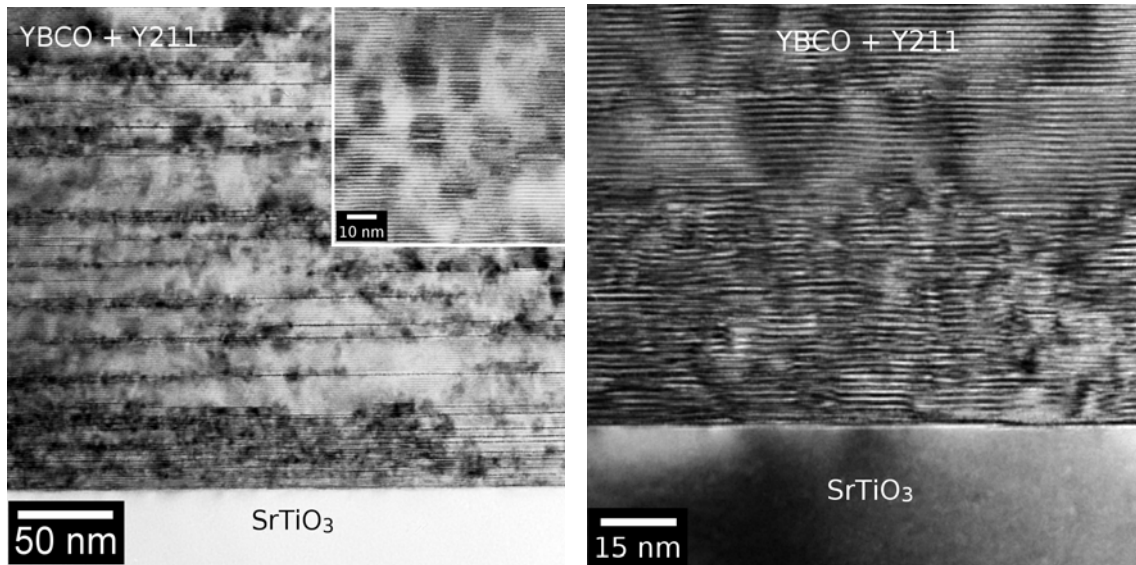


Figure V.13. (a) Cross-sectional TEM view shows a high density of randomly distributed nanosize (4-8 nm) Y211 precipitates, spaced by ~ 30 nm along the c-axis and ~ 10 nm in the ab plane. Horizontal black lines indicate stacking faults whose density significantly increases near the interface. (b) Close up view of the ~ 60 nm thick layer near the interface where the YBCO matrix is highly distorted because of tangled stacking faults with Y211 precipitates and threading dislocations, producing high strain fields and lattice buckling. (TEM images by Dr. F. Kametani.)

V.4.3 Discussion

The present experiment was motivated by the idea that the Y211 nanoprecipitates would provide strong 3D pinning so that vortices are chopped into separate, individually pinned segments. This condition is indeed fulfilled, as indicated by the linear $I_c^*(t)$ behavior which implies a thickness-independent incremental J_c , and by the very high $F_{p,max}$ of ~ 8.8 GN/m³ evaluated over the whole film thickness. In contrast to YBCO films without evident precipitates which show clear characteristics of collective pinning such as a

declining H_{irr} at small t and thickness-dependent $F_p(H)$ curves [25], our films had H_{irr} and $F_p(H)$ properties independent of film thickness except in the thin 60 nm interface layer, where the defect density is much higher and $F_{p,max}$ reached 13.8 GN/m^3 . The $J_{c,incr}$ variation of $2.4 - 3.5 \text{ MA/cm}^2$ in the bulk of the film is likely due to a combination of fluctuations in Y211 density and uncertainties in the exact thickness of the removed layer in each case (Fig. V.12).

To check if our J_c values are roughly consistent with the observed precipitate density, we estimated the maximum J_c which would be determined by depinning of elliptical vortex segments whose ends are fixed by neighboring nanoprecipitates with mean spacing d . J_c can then be estimated from [27]

$$J_c = \frac{\phi_0}{2\pi\mu_0\lambda_a\lambda_c d} \ln \frac{d}{\xi_c} \quad (\text{V.2})$$

Here, ϕ_0 is the flux quantum, μ_0 is the magnetic permeability, λ_a and λ_c are the London penetration depths in the ab -plane and along the c -axis, respectively, and ξ_c is the coherence length along the c -axis. If we take $\lambda_a = 0.4 \text{ }\mu\text{m}$, $\lambda_c = 2 \text{ }\mu\text{m}$, and $\xi_c = 1 \text{ nm}$ at 77 K with the observed average mean Y211 separation d of $\sim 30 \text{ nm}$, Eq. V.2 gives $J_c \sim 3.7 \text{ MA/cm}^2$, in agreement with the observed incremental J_c values away from the interface area. According to Eq. V.2, the observed J_c variation of $2.4 - 3.5 \text{ MA/cm}^2$ seen in Fig. V.11 corresponds to a variation in the mean precipitate separation from 50 to 35 nm , respectively.

The interface layer exhibits even stronger pinning and has a stacking fault density significantly higher than in the main part of the film. Moreover, the stacking faults have correlated partial dislocations tangled with the Y211 precipitates and the threading

dislocations emanating from the interface, producing strong strain fields, all of which can strongly enhance the pinning force. According to Eq. V.2, the measured self-field J_c value of 7.1 MA/cm^2 implies a mean pin separation $\sim 10 \text{ nm}$, consistent with Fig. V.13b. This strong pinning behavior with very high $F_{p,\text{max}}$ of 13.8 GN/m^3 reaches about two thirds of the present champion RE-123 PLD films made with the artificial pinning center distributions [28-30]. We thus conclude that the variation of $F_{p,\text{max}}$ with thickness (Fig. V.12(b)) in our films is caused by the almost bimodal vortex-pinning defect density distribution (Fig. V.13(b)).

The production of uniform, dense arrays of nanoprecipitates is a natural route to a uniform through-thickness, vortex-pinning microstructure with very high J_c . The significant potential of nanoscale pinning engineering is well illustrated both by the results of this work and by the previous spectacular high J_c values for the Sm-doped artificial pinning center structures [28,29]. Analysis of real coated conductors shows also that current-blocking defects that reduce the current-carrying cross-section must also be avoided [31-33]. In the present case around 5 vol.% of insulating Y-211 particles of $\sim 4 - 8 \text{ nm}$, with separations of 10-30 nm produce strong 3D pinning indeed.

V.5 Thickness dependence of J_c in MOD YBCO coated conductors

In this section, similar depth profiling experiments is reported which reveal the thickness dependence of I_c , J_c , T_c , the room temperature resistivity ρ_{300K} , resistivity curve $\rho(T)$, the bulk flux pinning force curve $F_p(H)$, and the microstructures of three *ex situ*

MOD YBCO films made on Ni-W rolling-assisted biaxially textured substrates (RABiTS) made at American Superconductor Corporation – real coated conductors. The $J_c(t)$ of these samples shows only a weak quasi-linear thickness dependence, while the strong pinning sample just described in section V.4, no change of the shape of $F_p(H)$, $J_c(H)$, and H_{irr} with thickness is seen. It is found that the weak degradation of J_c is due to the reduction of effective current carrying cross-section, which is caused by porosity enhancement as thickness increases. If the through-thickness variation of current-carrying cross-section caused by varying porosity is taken into account, the local incremental J_c shows thickness independence over a substantial part of the film thickness. For MOD films it appears in general that inherently strong vortex pinning leads to an essentially thickness-independent flux pinning J_c that is partially degraded by current-blocking porosity that builds up in the thicker portions of the film.

V.5.1 Experiment

YBCO bridges $\sim 300 \mu\text{m}$ wide and $\sim 500 \mu\text{m}$ long were cut by Nd-YAG (yttrium aluminum garnet) laser ablation so as to restrict I_c to $< 10 \text{ A}$ at full YBCO thickness. Each link was thinned with 500 eV Ar ions impinging at 45° while the sample was cooled to $\sim 230 \text{ K}$ to avoid ion damage. The YBCO etch rate was calibrated to be $\sim 12 \text{ nm/min}$ by measuring the thickness of each milled sample with a Tencor profilometer. There is an inherent uncertainty in the true YBCO thickness in MOD coated conductors arising from a rough top surface of the YBCO and the tendency of the profilometer to measure the maximum height of the YBCO. After each milling step, the $V-I$ characteristics were

measured with a four-point configuration at 77 K for magnetic fields up to the irreversibility field applied perpendicular to the film surface. To prevent excessive heating at currents higher than 100 mA, a square current pulse of 50 ms duration with a 30 ms voltage read window was used. J_c values were determined at a 1 $\mu\text{V}/\text{cm}$ electric field criterion. Resistivity as a function of temperature, $\rho(T)$, was measured during sample cool down and T_c was defined as the onset of zero resistance ($\sim 1\%$ of normal state resistance). X-ray diffraction measurements were made to determine the global texture of the YBCO layers. In-plane texture was determined by the FWHM of the in-plane, off-axis (ϕ) scan of the (103) YBCO peak, while the out-of-plane texture was measured from the rocking curve of the (005) YBCO peak.

V.5.2 Results

The key properties of the three samples at full thickness are shown in Table V.3. The highest $I_c^* = 313 \text{ A}/\text{cm}$ -width at $J_c(0\text{T}, 77\text{K}) = 2.5 \text{ MA}/\text{cm}^2$ was obtained in the 1.3 μm thick film (CC315), while the better textured 1.0 μm thick film (CC270) had $I_c^* = 272 \text{ A}/\text{cm}$ and the highest J_c value of $2.8 \text{ MA}/\text{cm}^2$. I_c^* of the less textured thinner film was somewhat lower; $128 \text{ A}/\text{cm}$ and $J_c = 1.2 \text{ MA}/\text{cm}^2$ due to its more misoriented grain boundary network and slightly different YBCO growth conditions [26]. The less textured sample (CC130) had in-plane full-width-half maximum (FWHM) ($\Delta\phi$) and out-of-plane FWHM ($\Delta\omega$) of 6.5° and 6.6° , as compared to values of $\sim 5.4^\circ$ and $\sim 3.7^\circ$ for the two higher J_c CCs.

Table V.3 Key properties of the three coated conductor samples

	CC130	CC270	CC315
Full thickness	1.1 μm	1.0 μm	1.3 μm
$\Delta\phi$ (YBCO)	6.5°	5.5°	5.4°
$\Delta\omega$ (YBCO)	6.6°	3.8°	3.7°
$J_c(77\text{K}, \text{self-field})$	1.2 MA/cm ²	2.8 MA/cm ²	2.5 MA/cm ²
$I_c^*(77\text{K}, \text{self-field})$ per cm width	128 A/cm	272 A/cm	313 A/cm
T_c	88.7 K	91.3 K	92.9 K

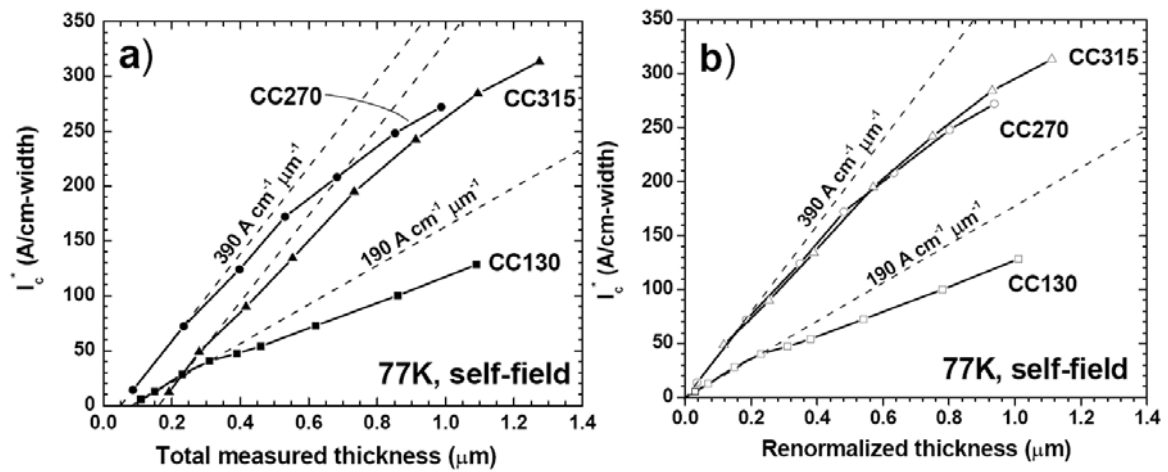


Figure V.14 (a) The critical current per unit width at I_c^* (77K, self-field) vs. the measured thickness for three different coated conductors. I_c^* goes to zero at non-zero thicknesses of 80, 50, and 150 nm, respectively. I_c^* initially increases linearly with a slope of $390 \text{ A cm}^{-1} \mu\text{m}^{-1}$ for CC315 and CC270 and $190 \text{ A cm}^{-1} \mu\text{m}^{-1}$ for CC130, with the slope becoming smaller at larger thickness. (b) I_c^* (77K, self-field) vs. the renormalized thickness, which subtracts the non-zero intercepts. CC315 and CC270, which have similar texture properties, now show excellent agreement.

Figure V.14(a) shows critical current per unit width I_c^* (77K, self-field) as a function of thickness t . The three data sets show smoothly increasing $I_c^*(t)$ curves with increasing t . For the two better textured samples (CC270/CC315), I_c^* increases linearly up to $\sim 0.2 \mu\text{m}$ at

a steep slope of $390 \text{ Acm}^{-1}\mu\text{m}^{-1}$, while I_c^* increases less steeply at $190 \text{ Acm}^{-1}\mu\text{m}^{-1}$ for the worse textured sample (CC130). The slopes decline with increasing t to less than $\sim 160\text{-}180 \text{ Acm}^{-1}\mu\text{m}^{-1}$ for CC270/CC315 and $\sim 120 \text{ Acm}^{-1}\mu\text{m}^{-1}$ for CC130 near the film surface. However, all three curves yield zero current at non-zero thicknesses of 80, 50, and 150 nm, respectively. Figure V.14(b) plots I_c^* as a function of the thickness renormalized by subtracting the non-zero intercepts at which I_c^* in Fig. V.14(a) vanishes. Such renormalization of t is applied throughout this section. It corrects for uncertain effects due to the influence of the rough top surface and porosity, as discussed later. CC315 and CC270, which have essentially identical texture, show nice overlap in the renormalized plot of Fig. V.14(b).

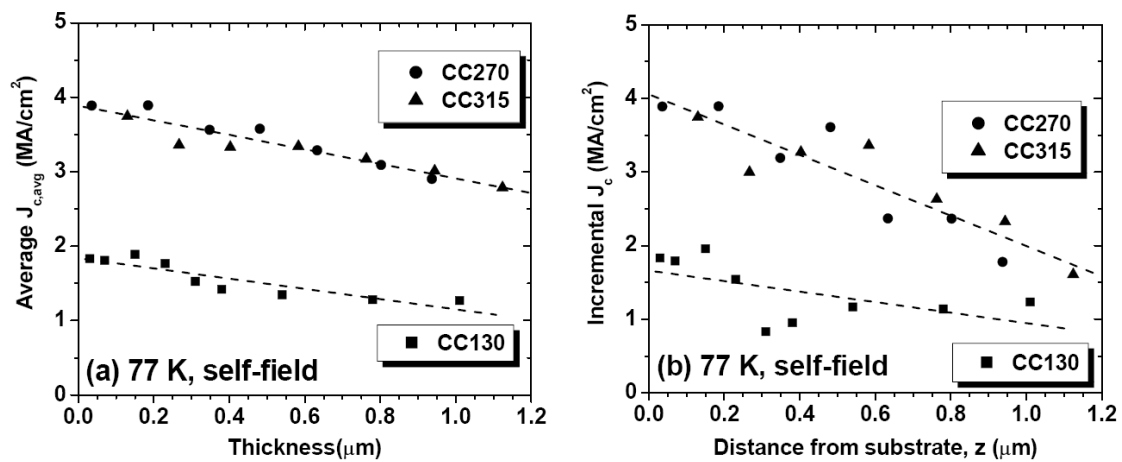


Figure V.15 (a) The average $J_c(77\text{K},\text{self-field})$ vs. thickness after renormalizing the thickness to subtract off the non-zero intercept in Figure V.14(a). $J_c(t)$ shows rather slow reduction with increasing thickness. CC315 and CC270 exhibit very high J_c of $\sim 4 \text{ MA/cm}^2$ at small thickness, while showing $\sim 3 \text{ MA/cm}^2$ at full thicknesses. The CC130 shows about half these J_c values due to its worse texture. (b) Incremental J_c data shows rather steep linear decrease to $\sim 1.6\text{-}1.7 \text{ MA/cm}^2$ near top surface for the better textured samples.

Figure V.15(a) shows the average (i.e. using I_c averaged over the full residual thickness of the YBCO) $J_{c,avg}(77K, \text{self-field})$ as a function of t . It is striking that the two better textured samples reach a high J_c value of $\sim 4.0 \text{ MA/cm}^2$ near the bottom of the film and show a gradual and rather linear decrease to $\sim 2.7 \text{ MA/cm}^2$ with increasing t . The less-textured sample, CC130, shows J_c decreasing from $\sim 1.8 \text{ MA/cm}^2$ to $\sim 1.2 \text{ MA/cm}^2$ with increasing t . The incremental J_c data are shown in Figure V.15(b) as a function of distance from substrate. The two better textured samples exhibit a J_c value of $\sim 4.0 \text{ MA/cm}^2$ near the bottom and show a rather greater decline to $\sim 1.6 \text{ MA/cm}^2$ at full thickness than do the average values. The CC130 shows more scattered data, but the tendency is the same with the better samples. When the incremental J_c is plotted as in Fig. V.15(b), there is somewhat more scatter but the trends remain the same.

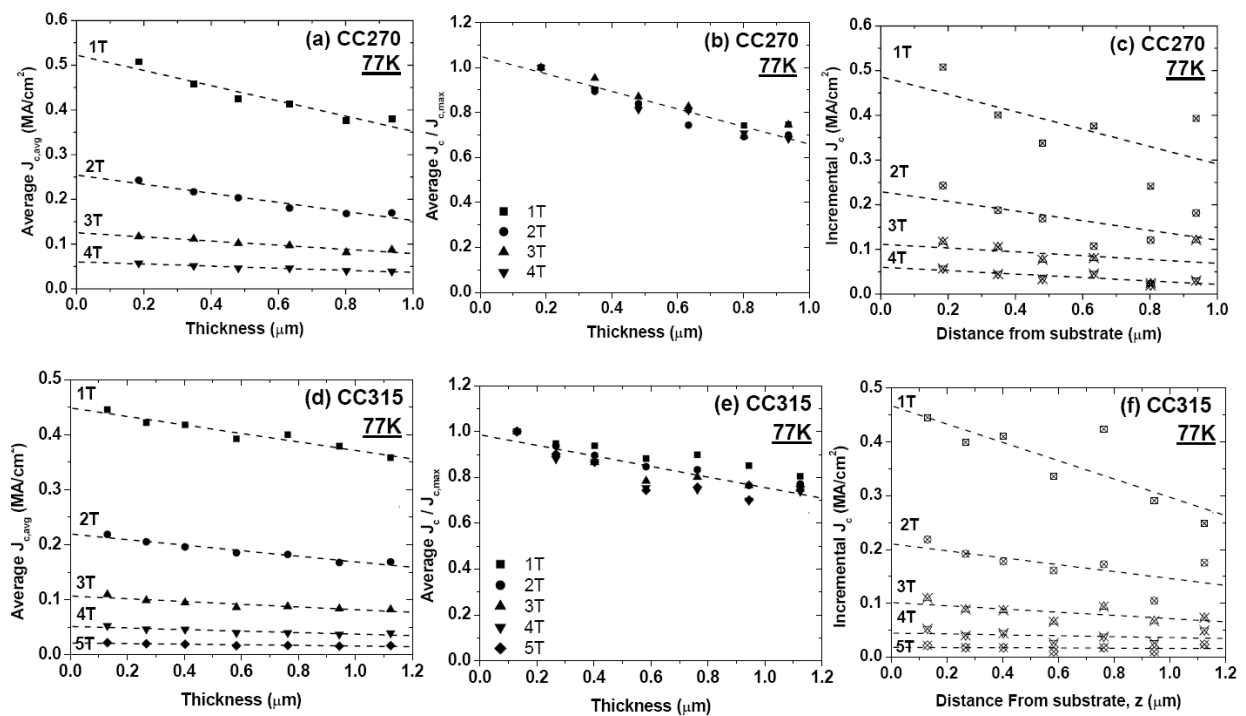


Figure V.16 In-field $J_c(t)$ data for CC270 and CC315. The $J_c(t)$ or incremental $J_c(t)$ data in fields is more or less identical to that at self-field.

Figures V.16 show a more detailed data set for the average and incremental in-field $J_c(t)$ for CC270 and CC315. The functional dependence is essentially identical to that seen at self field, showing that the thickness dependence is practically unaffected by the magnetic field, whether below or above the field (~ 2 T at 77 K) at which grain boundaries cease to limit the magnitude of J_c of these films [26].

Figure V.17(a) shows the room temperature resistivity, ρ_{300K} as a function of t . The 3 samples have rather high ρ_{300K} of 365 – 380 $\mu\Omega\text{cm}$ at their full thickness, compared to the typical 200 – 250 $\mu\Omega\text{cm}$ of high-quality, dense YBCO films [20,34,35]. The room temperature resistivity shows a monotonic decrease to ~ 300 $\mu\Omega\text{cm}$, as the YBCO layer is thinned to ~ 0.15 μm , the values being ~ 220 - 270 $\mu\Omega\text{cm}$ at small thicknesses < 0.15 μm . The asymptotic ρ value at zero thickness is ~ 200 $\mu\Omega\text{cm}$, a value expected for well oxygenated, dense YBCO films. We only see such a dense structure very near the interface, as described later. Insets to Fig. 17(a) show the local volume fraction of pores for CC270 and CC315 calculated using an effective medium theory (EMT), as detailed in the discussion, using a room temperature resistivity ρ_{300K} appropriate for dense high quality YBCO films of 200 $\mu\Omega\text{cm}$. Figure V.17(b) indicates the room temperature resistivity, ρ_{300K} as a function of t , when calculated from the total measured thickness of Fig. V. 15(a). Without the renormalization incited by the non-zero intercepts, the ρ_{300K} values increase rapidly below ~ 0.2 - 0.3 μm to physically unreasonable values, which are quite inconsistent with the rather uniform depth profiled superconducting properties shown in Figures V.18 and 19.

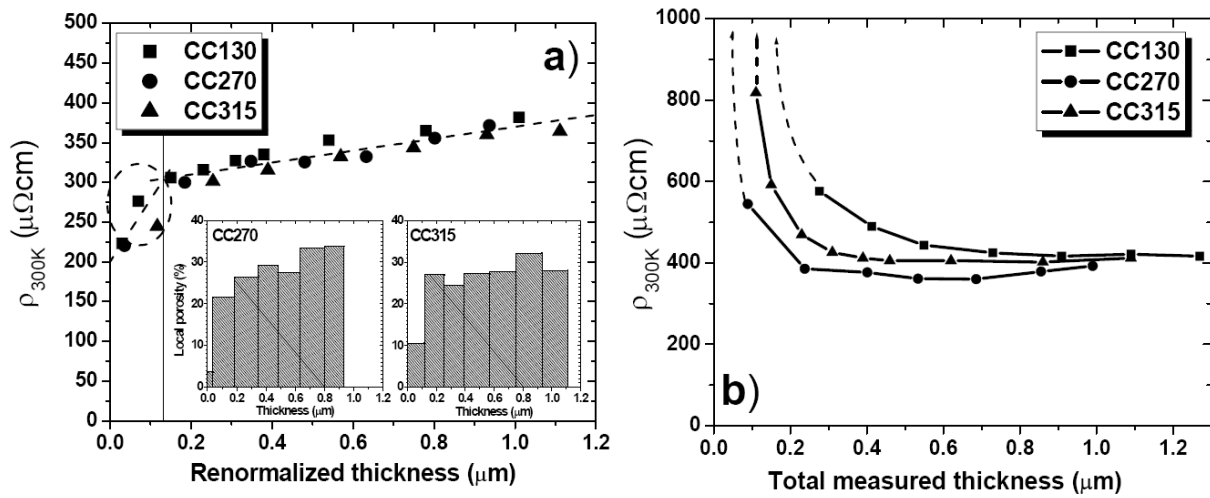


Figure V.17 (a) The room temperature resistivity, ρ_{300K} , as a function of thickness. The ρ_{300K} values at full thickness are high, reaching $\sim 365 - 380 \mu\Omega\text{cm}$ for all samples. However, the ρ_{300K} values show a general linear decline with decreasing thickness down to $\sim 0.15 \mu\text{m}$, and steeper decreasing below to a limiting value of $\sim 200 \mu\Omega\text{cm}$ at zero thickness. This value is typical for dense, well-oxygenated YBCO. The insets show the local porosity of CC270 and CC315 calculated by effective medium theory. (b) ρ_{300K} as a function of t , when calculated from measured thickness (which is shown in Fig. V.14(a)). The ρ_{300K} values increase rapidly below $\sim 0.2\text{-}0.3 \mu\text{m}$ to physically unreasonable values.

Figures V.18(a)-(c) show the $\rho(T)$ curves normalized to ρ_{300K} . An important feature is that the curve shapes are independent of thickness for each sample, demonstrating both that the oxygenation state is identical through thickness and that repeated ion milling did not deoxygenate the film. The curves of CC130 and CC270 show similar slight upward curvatures and negative intercepts with the ρ axis for the linear extrapolation of $\rho(T)$, which indicates that these two films are slightly oxygen over-doped [21], consistent with their lower T_c values. The curve shape of CC315 shows almost linear $\rho(T)$ and the highest T_c , consistent with this sample being close to optimum doping. Figures V.18(d)-(f) indicate that the T_c transition behavior is independent of thickness too, both with respect to T_c and

the T_c transition width ΔT_c . Only a relatively small T_c variation of 1-2 K is observed for each film, as shown in Figure V.19. This result also supports our conclusion that the oxygenation state of each film is independent of thickness.

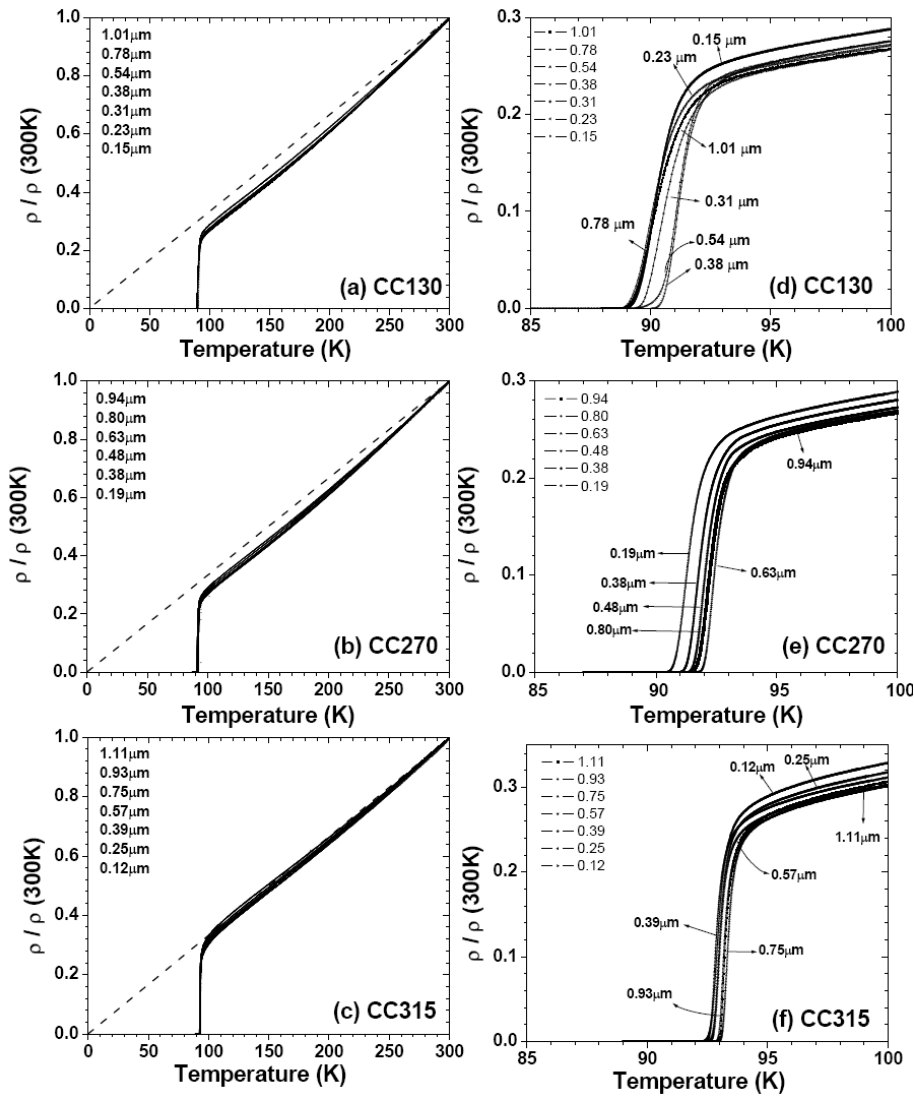


Figure V.18 The plots show the $\rho(T)$ curves normalized to $\rho_{300\text{K}}$ for (a)(d) CC130, (b)(e) CC270, and (c)(f) CC315. Remarkably, the curve shapes are identical for all thicknesses for each sample. The curves of CC130 and CC270 show slight upward curvature and a slight negative linear intercept typical of overdoped YBCO, while CC315 shows almost linear $\rho(T)$. All samples are well oxygenated through their whole thickness.

Figure V.20 shows the $J_c(H)$ curves, irreversibility field H^* and the normalized bulk pinning force ($F_p/F_{p,max}$) for CC315 as a function of reduced field H/H^* , where the irreversibility field H^* is defined at $J_c = 100 \text{ A/cm}^2$ or by extrapolation of $F_p(H)$ to zero. Although the magnitude of $J_c(H)$ increases somewhat at smaller t , it is striking that $H^*(77\text{K})$ for all 3 samples and the shapes of the pinning force curves are also quite independent of thickness, indicating that the dominant vortex pinning mechanisms are also independent of film thickness.

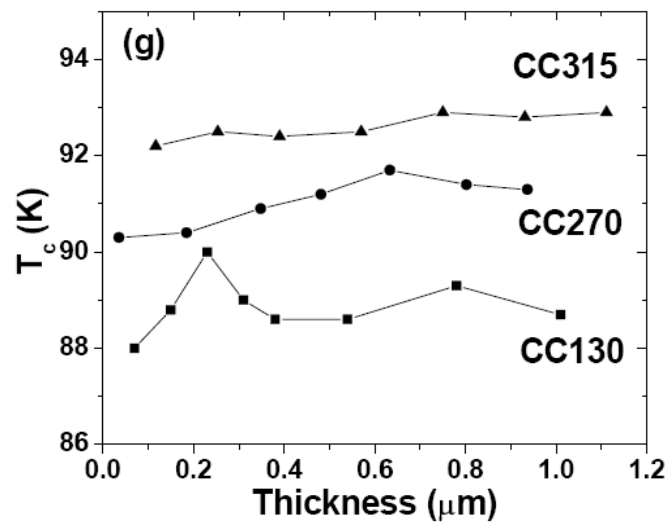


Figure V.19 T_c as a function of thickness, where T_c is determined at the onset of $\rho=0$. The relatively small T_c variation within 1-2 K is seen for each sample.

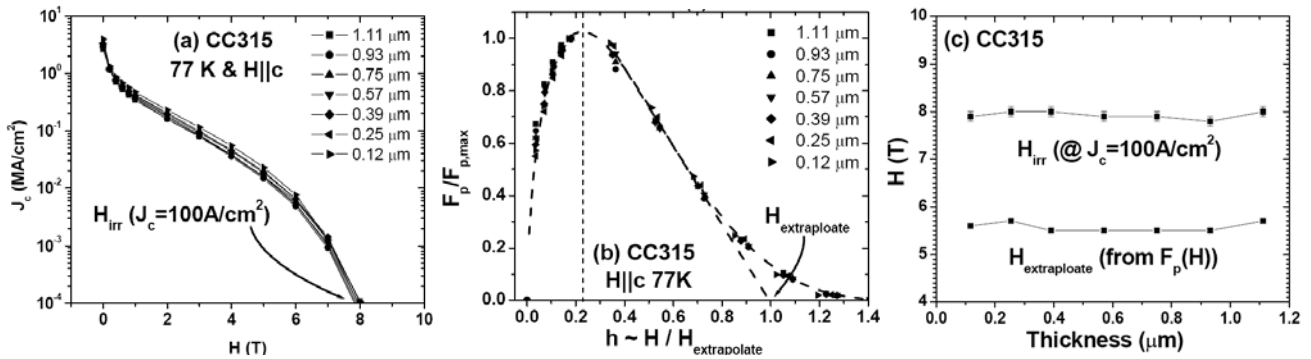


Figure V.20 (a) The critical current density as a function of applied field $J_c(H)$ for CC315. (b) Normalized bulk pinning force ($F_p/F_{p,max}$) vs. reduced field ($H/H_{extrapolate}$) for CC315. $H_{extrapolate}$ is defined by extrapolation of linear sections of the high-field curves, as indicated. Neither the shapes of the pinning force curves or $J_c(H)$ change as a function of thickness. (c) The irreversibility field $-H_{irr}$ at $J_c=100A/cm^2$ and $H_{extrapolate}$ in $F_p(H)$ plot - as a function of thickness is shown. The irreversibility field is constant as a function of thickness.

Figure V.21 shows plan-view SEM images of the original top surface of the 1 μm CC130 and of the milled surfaces at thicknesses of 0.78, 0.38, and 0.15 μm . Evidently, the original surface is quite rough and porous, but this roughness and porosity decreases continuously towards the substrate. The porosity variation is qualitatively consistent with the ρ_{300K} vs. t results and local porosity of inset of Fig. V.17(a) if one assumes that the resistivity at any t is controlled by the local porosity-controlled cross-sectional area.

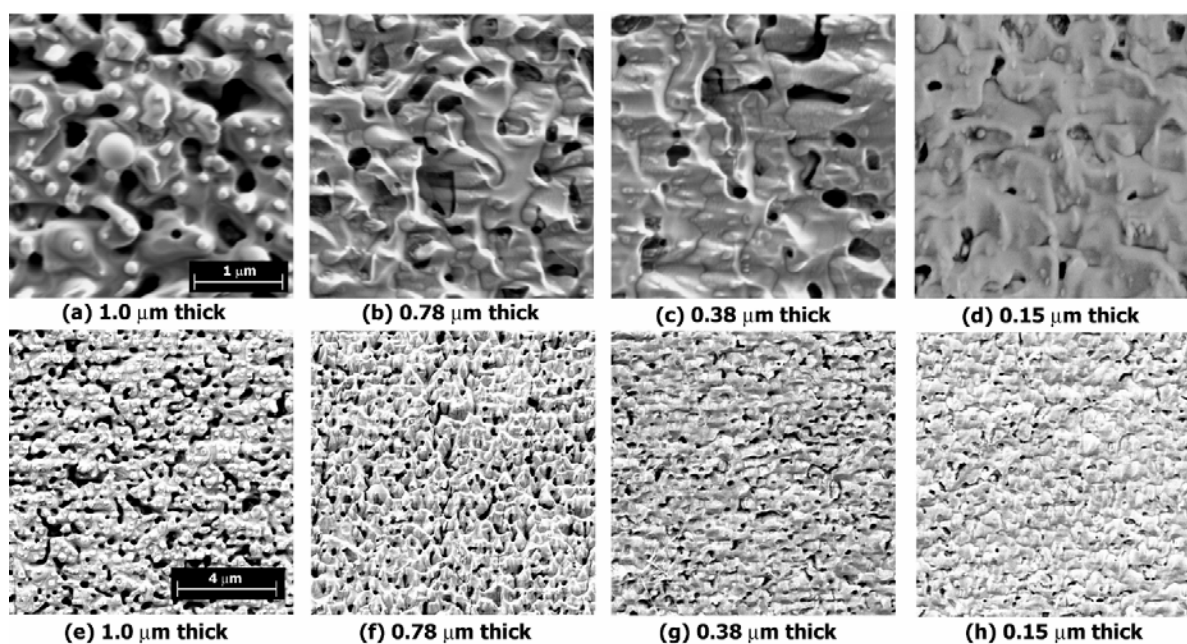


Figure V.21 Plan view SEM images of (a)(e) the original surface of CC130 at 1 μm thickness and after milling the CC130 sample to (b)(f) 0.78, (c)(g) 0.38, and (d)(h) 0.15 μm thickness. The rough and porous nature of the film surface is quite evident, as is the decline in porosity near the substrate.

Figure V.22(a) shows a longitudinal section TEM image of CC270 that gives a broad overview of the porosity, while Figures V.22(b) and (c) show higher resolution images of the same CC, which was taken by Dr. Terry Holesinger, Los Alamos National Laboratory. Porosity with a scale in the range 0.2-0.5 μm which steadily increases towards the top of the YBCO is evident, as is the variability of porosity from place to place. The rather uneven top YBCO surface where it contacts the silver cap layer has a height variation of up to 0.2 μm . The film also shows many planar stacking faults parallel to the YBCO *ab* planes. These faults are typically 30 – 50 nm apart along the *c*-axis, are of high density, and distributed rather evenly through the film thickness. The laminar and porous

microstructure is in strong contrast to the columnar and dense microstructure of PLD conductors.

Figure V.23 shows two plan-view TEM images of the CC270 sample which also indicate porosity change through thickness (taken by Dr. Xueyan Song of University of Wisconsin). Fig. V.23(a) is taken $\sim 0.2 \mu\text{m}$ below the top surface and shows high porosity. In contrast, the image taken near the bottom shows much less porosity [Fig. V.23(b)]. The pores present in Fig V.23(a) vary in scale from 80 – 400 nm.

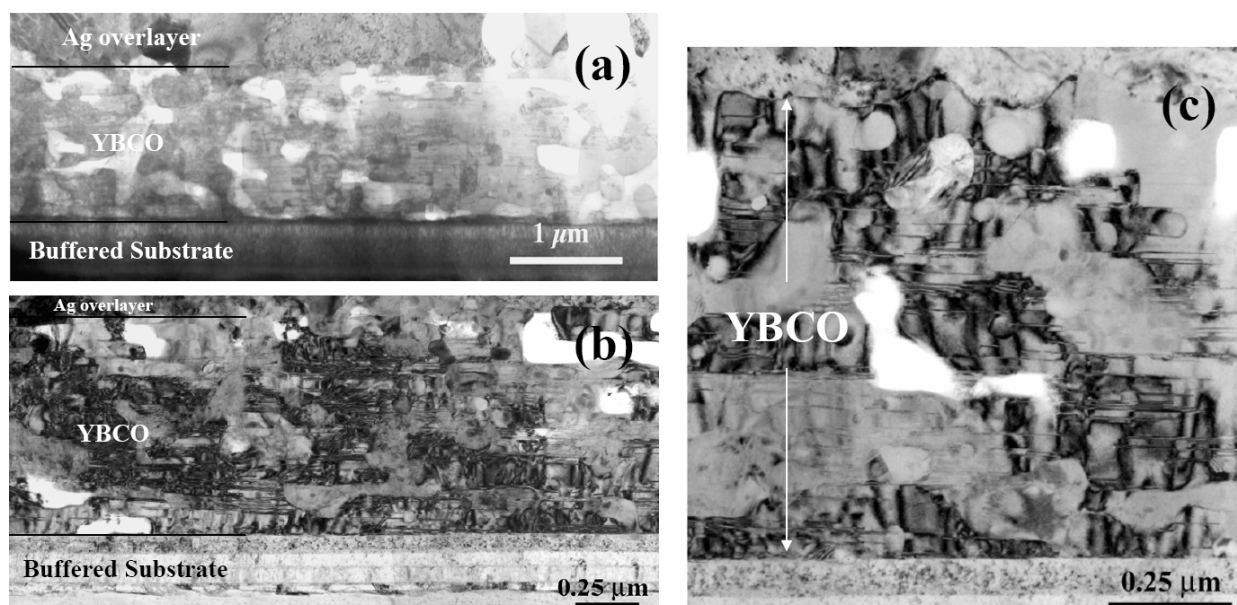


Figure V.22 Cross-sectional TEM images of the CC270 sample; (a) a broad overview of the porosity, (b)(c) in higher resolution. Porosity with a scale in the range 0.2-0.5 μm increases towards the top of the YBCO. The rather uneven top YBCO surface where it contacts the silver cap layer has a height variation of up to 0.2 μm . The film also shows many planar stacking faults parallel to the YBCO *ab* planes, which are typically 30 – 50 nm apart along the *c*-axis, are of high density, and distributed rather evenly through the film thickness. The laminar and porous microstructure is in strong contrast to the columnar and dense microstructure of PLD conductors (by Dr. Terry Holesinger).

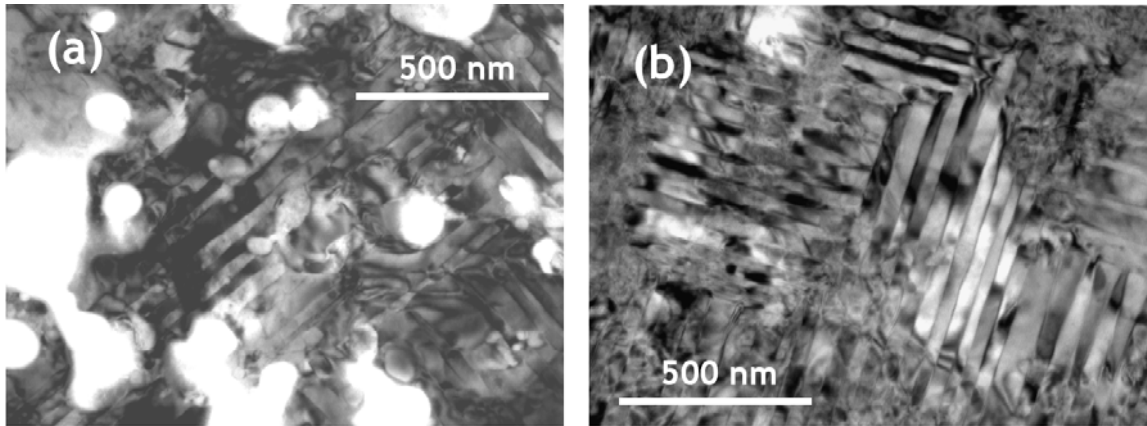


Figure V.23 Plan-view TEM images of the CC270 sample. (a) a image taken $\sim 0.2 \mu\text{m}$ below the top surface and shows high porosity, indicating porosity in various scales. (b) a image taken near the bottom shows much less porosity (by Dr. Xueyan Song).

V.5.3 Discussion

A striking feature of these MOD CCs is their high average $J_c \sim 3 \text{ MA/cm}^2$ and high I_c values ($\sim 300 \text{ A/cm}$) at thicknesses of $\sim 1 \mu\text{m}$, even though these J_c or I_c values are definitely limited by higher angle grain boundaries [26] and by their significant porosity. They also have a $J_c(t)$ dependence much weaker than most PLD films [1-7], including the PLD films studied in section V.3, and earlier standard process PVD-BaF₂ processed conductors [15,36]. The present MOD films have uniform local properties, as indicated by the thickness independence of T_c , ΔT_c , the shape of the bulk flux pinning curve $F_p(H)$, the irreversibility field H_{irr} and the resistivity curve $\rho(T)$ shape. Consistent with these observations, microscopy shows no significant change of microstructure with thickness, except for a marked increase in porosity with increasing thickness. Moreover, these samples also show marked changes in the *magnitudes* of room temperature resistivity $\rho_{300\text{K}}$

and both the average J_c and the incremental J_c that plausibly correlate to a thickness-dependent *area degradation*. From the effective medium calculations of the resistivity discussed below, we conclude that the local vortex-pinning-determined J_c is nearly independent of thickness but that the average critical current density $J_{c,avg}(t) = I_c/A$ defined by the whole YBCO cross-section A depends on t precisely because the thickness dependence of porosity causes the current-carrying cross-section to vary. The striking paradox of such a conclusion is that it is these porous and somewhat rough MOD films that show higher J_c and weaker $J_c(t)$ than the denser PLD films because vortex pinning is enhanced by small nanoscale pores, even as larger or locally clustered pores may obstruct current flow. As coated conductor process scale up continues and the ultimate limits of coated conductor technology are explored, the mechanisms which control the thickness dependence of the critical current density demand a better understanding of this apparent paradox.

The irregular surface and porosity of MOD films shown in Figs. V.21-23 is a direct consequence of the coating technique, which lays down a precise quantity of YBCO precursor over a defined substrate area. The decomposition of the carboxylate precursors and subsequent evolution of gas-phase HF, produce ~50% reduction in original YBCO precursor thickness [37]. Local variations of porosity produced by these processes result in an unavoidable variation in the local cross-section of YBCO. The profilometer may also over-estimate the thickness t because its 12.5 μm tip radius is much larger than the local thickness variation due to rough surface $\sim 0.1 \mu\text{m}$ (Fig. V.22). After ion milling, top-surface roughness does propagate to smaller thicknesses with some smoothing and with a

cross-sectional uncertainty compounded by porosity inside the film. We believe that these factors contribute to the non-zero intercept seen in Fig. V.14(a). Fig. V.17(b) also indicates the physically unreasonable ρ_{300K} values when the total measured (over-estimated) thickness is taken into account. Indeed, the $\rho_{300K}(t)$ is inconsistent with other results, including uniform superconducting properties through thickness and observed porosity change. Actually, Fig. V.22(a) suggests a local thickness of $\sim 1.1 \mu\text{m}$ for CC270 with peak-to-valley variation $> \sim 0.1 \mu\text{m}$. It appears that the thickness of this type of MOD conductor cannot be determined to better than $\sim \pm 10 \%$. Collectively these measurements lead to an over-estimate of film thickness, thus leading to a small under-estimate of the J_c value derived from the whole cross-section.

The effect of porosity on J_c can manifest itself in different ways. Large scale porosity and surface roughness on the scale larger than the London penetration depth $\lambda(77K) \sim 0.4 \mu\text{m}$ mainly obstruct current flow. However, close examination of Figs. V.21-23 shows that pores have multiple scales, many smaller than $0.4 \mu\text{m}$. Such nanoscale porosity can enhance flux pinning by either caging the vortex screening currents (magnetic pinning) or by vortex-core interactions with small pores (vortex core pinning). An additional positive feature of the porosity is that it should enhance full oxygenation of the film, a property which is consistent with the through-thickness uniformity of T_c , ΔT_c , $F_p(H)$, H_{irr} and the normalized shape of $\rho(T)$ [Figs. V.17-19].

In trying to understand the mechanisms underlying individual $J_c(t)$ data sets, several points should be addressed:

- (1) *Is the pinning microstructure independent of thickness?*
- (2) *Is the current-carrying cross-section independent of thickness?*
- (3) *Are grain boundary limitation effects present?*

Turning to the first question, it seems that the pinning microstructure of our MOD films is independent of thickness, as judged from the thickness independence of T_c , ΔT_c , the shape of the bulk flux pinning curve $F_p(H)$, the irreversibility field H_{irr} , and the normalized resistivity curve $\rho(T)$ shape. Microscopy also suggests no significant change of microstructure with thickness, except for porosity. In this respect these MOD samples appear to be very different from the PLD samples of Foltyn *et al.* [22] which exhibit very high interface J_c up to $\sim 7 \text{ MA/cm}^2$ that the authors associate with an interface dislocation array. The question of whether the current-carrying cross-section is independent of thickness is particularly relevant to our MOD conductors, for which increase of porosity is observed with increasing thickness, as shown in the cross-sectional TEM image of Fig. V.22, the plan-view SEM images of Fig. V.21 and the plan-view TEM images of Fig. V.23. Only in Fig. V.21b taken at the bottom of the YBCO layer is the porosity apparently absent. Such large-scale porosity must limit the connected cross-section, a result that is seldom seen for well-made PLD films. As for the third question of whether grain boundary cross-section limitation effects are present, an earlier study answers this question [26]. These conductors were made on highly textured RABiTS, but even for the two better textured samples, major grain boundary network limitation effects are present below $\sim 2T$, as seen in

our previous work [26]. CC270 and an MOD single crystal film had 77 K, self-field average $J_{c,avg}$ values of ~ 2.6 and ~ 5.3 MA/cm² respectively. This latter value of 5.3 MA/cm² unambiguously places the MOD-process films as strong vortex-pinning YBCO films, in spite of their significant porosity and their increased ρ_{300K} values.

To estimate the effect pores in of reducing the current-carrying cross section A_{eff} , we use a conventional effective medium theory (EMT) [38], assuming that the sample contains pores of volume fraction $1 - x$ embedded in a metallic matrix with anisotropic resistivity ρ_a in the ab plane and ρ_c along the c -axis. As shown in the Appendix, the anisotropic EMT gives the following expression for the measured in-plane resistivity ρ , and A_{eff}

$$\rho = \rho_a \frac{1 - x_c}{x - x_c}, \quad A_{eff} = A \frac{x - x_c}{1 - x_c}, \quad (V.3)$$

where A is the geometrical cross-sectional area, and x_c depends on the anisotropy ratio $\varepsilon = \rho_a/\rho_c < 1$:

$$x_c = \frac{1}{2(1 - \varepsilon)} \left[1 - \frac{\varepsilon}{2\sqrt{1 - \varepsilon}} \ln \frac{1 + \sqrt{1 + \varepsilon}}{1 - \sqrt{1 - \varepsilon}} \right] \quad (V.4)$$

Eq. (V.3) shows that ρ increases and A_{eff} decreases as the volume fraction x of the conductor decreases. The resistivity becomes infinite and A_{eff} vanishes if x is smaller than the EMT percolation threshold x_c , which varies between 1/2 for the highly anisotropic 2D case $\varepsilon \rightarrow 0$ and 1/3 for the isotropic 3D case, $\varepsilon \rightarrow 1$. For YBCO, $\varepsilon = \rho_a/\rho_c = 0.2$ and Eq. (V.4) yields $x_c = 0.42$. Next we calculate the current-carrying volume fraction x of YBCO in our films, re-writing Eq. (V.3) in the form:

$$x = x_c + (1 - x_c) \frac{\rho_a}{\rho} \quad (\text{V.5})$$

Taking $\rho_a \sim 200 \mu\Omega\text{cm}$ (the asymptotic value at zero thickness in Fig.V.17) and $\rho = 380 \mu\Omega\text{cm}$, we obtain a connected cross-section $x = 0.73$. This result is in general accord with the microstructural images in Figs. V.21-23. This total 27% pore volume obviously can considerably obstruct current flow, as well as providing some vortex pinning by the smaller pores. The substantial thickness variation of the normal state resistivity is a clear evidence that significant obstruction of the normal-state current occurs, when supported by the lack of through-thickness change to the local superconducting properties. Using Eq. (V.3) to extract the EMT-current-carrying cross-section from the resistivity data in Fig. V.17, we then calculated the thickness-dependent porosity which is shown in insets to Fig. V.17(a) and then used these data to calculate a porosity-renormalized critical current density $J_c = I_c/A_{eff}$ for each t , as shown with open symbols in Figures V.24(a) and (b). Consistent with our deduction that the *local* properties do not change significantly through thickness, this porosity-renormalized J_c (but not yet grain boundary renormalized) exhibits even less thickness dependence and even higher average $J_{c,avg}$ values 4–5 MA/cm². Although the incremental $J_c(t)$ data in Fig. V.24(b) are more scattered than the full-thickness averages in Fig. V.22a, the incremental $J_c(t)$ data now suggest that there is NO thickness dependence in the bottom half of the films. Beyond about 0.6 μm thickness, $J_c(t)$ then falls off from the plateau of $\sim 4.5 \text{ MA/cm}^2$ to $\sim 2 \text{ MA/cm}^2$ at $\sim 1.1 \mu\text{m}$. The basis for this change is not certain, although one possibility is that the porosity is smaller and closed

towards the bottom of the film and thus more useful for flux pinning than the more open, crevasse-like, current-blocking porosity that appears at the top of the film.

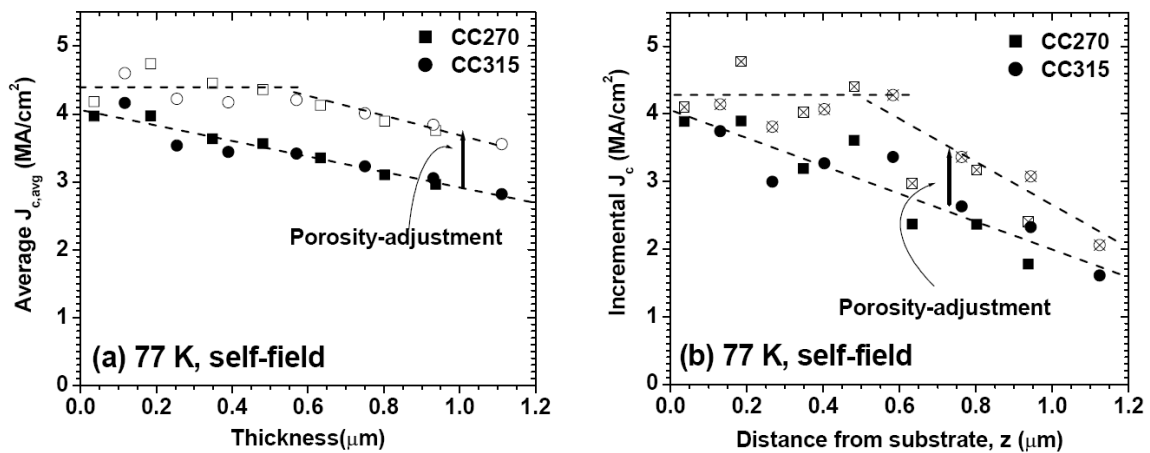


Figure V.24 (a) Porosity-renormalized average $J_{c,avg}(t)$ using effective medium theory (EMT) is shown with open symbols to take account the porosity change through thickness. (b) Porosity-renormalized incremental $J_c(t)$.

The high J_c values reported here may originate from multiple defect structures, including pores, twins, point defects, stacking faults, Y_2O_3 particles, as well as atomic-scale disorder. Civale et al. [39] have pointed out that there is a strong ab plane pinning peak in these MOD films, which they correlate to the significant volume fraction of ab planar defects observed clearly in Figs. V.21(b) and (c). Thus, we conclude that these MOD films are always in the strong 3D vortex pinning regime, for which J_c should indeed be independent of thickness as suggested by Fig. V.24, because strong pins spaced by 10 – 100 nm subdivide vortices into short, nearly decoupled segments much smaller than the film thickness ($t \gg d$). This conclusion is consistent both with the observed independence of J_c on t and the estimate based on Eq. (V.2), which requires a mean pin spacing of order 30 nm.

(Observed J_c value of $\sim 4 \text{ MA/cm}^2$ gives mean pin spacing of order $\sim 30 \text{ nm}$.) By contrast, the $t^{-1/2}$ dependence of J_c seen in PLD films may indicate that vortex lines are pinned by many weaker defects which do not disrupt the continuity of the vortex lines.

V.6 Two dimensional collective pinning vs. three dimensional strong pinning

Three sets of samples were investigated to better understand the thickness dependence behavior of YBCO films, so the current-carrying capability of coated conductors can be maximized and optimized for applications. First, pure, essentially single phase and uniform YBCO thin film samples were studied to examine the physics of vortex dimensionality responsible for the J_c reduction. These relatively thin films with the least materials-related effects and few or no strong pinning centers exhibited clear evidence of weak 2D collective pinning and large thermal fluctuation effects at small thickness. Secondly, $1 \mu\text{m}$ thick YBCO thin film containing $\sim 5 \text{ vol.}\%$ of insulating Y_2BaCuO_5 (Y211) nanoparticles was tested in order to understand how the insulating nanoparticles, capable of executing a strong core pinning interaction within the YBCO matrix can affect the J_c thickness dependence. It was found that J_c in the body of the film was high, uniform and independent of thickness, except very near the interface where the defect density was significantly enhanced too. The addition of nanoscale Y211 precipitates resulted in strong, 3D pinning characterized by a pin spacing much smaller than the film thickness, contrary to the pure YBCO films without evident precipitations. Lastly, the thickness dependence of J_c of $1 \mu\text{m}$ thick YBCO films made by an *ex situ* metal-organic deposition (MOD) process

was explored. The MOD films exhibited only a weak dependence of J_c on increasing t . It was concluded that these MOD films exhibit strong 3D pinning behavior along with many evidences of strong pinning of high J_c , H_{irr} , and $F_{p,max}$. Their weak thickness-dependent J_c reduction is due to degradation of microstructure, mostly to porosity which increases with thickness, thus progressively changing from being a strong pinning defect near film bottom to a current blocking defect near the film top.

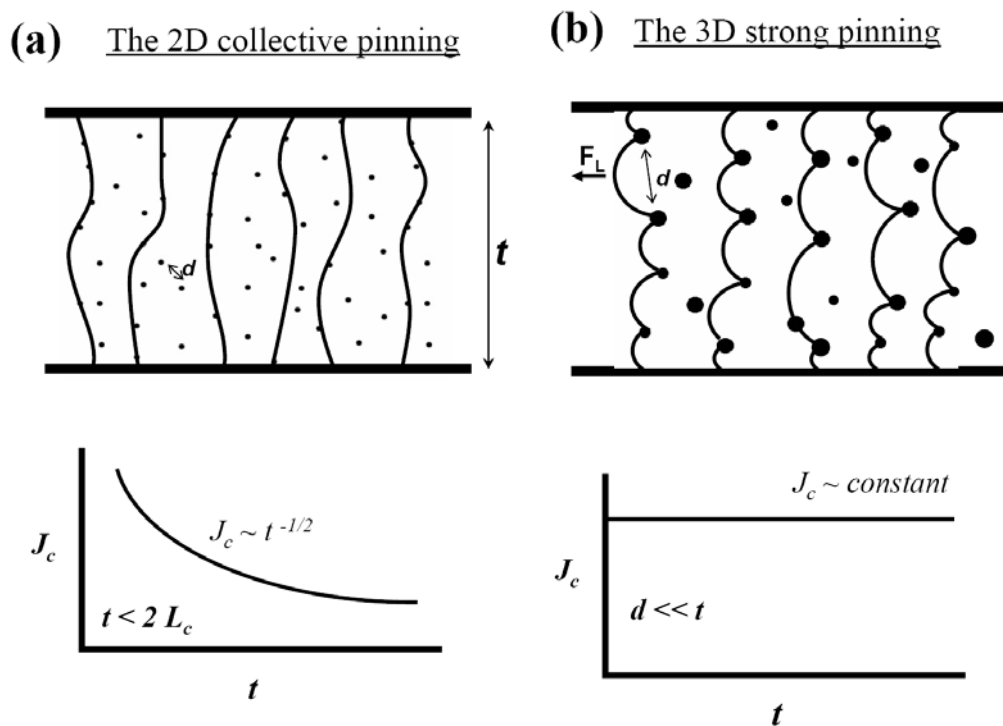


Figure V.25 (a) Illustration of continuous vortex lines in a dense array of weaker pins, which leads to the inverse square root dependence on thickness seen in many normally made PLD films without major pinning features. (b) Illustration of the way that vortex lines can be chopped into short discontinuous segments by strong pinning defects which enforce depinning by the bending of a vortex segments into a critically sized vortex loop, whose diameter is equal to the separation d between pins. This case corresponds to the PLD film with Y211 particles and to the MOD films.

The first two sets of PLD samples represent two possible different types of pinning behavior, as illustrated by Figure V.25, if ignoring the presence of interface layer in Y211-dispersed sample where its microstructure is different. Figure V.25(a) illustrates *the 2D collective pinning*, observed in the pure YBCO sample set. A weak, but dense array of pins perturbs the vortex lines but does not make them discontinuous. J_c in this case can be estimated using 2D collective pinning theory for a rigid vortex line in a thin film where the bending distortions of the vortex are negligible [9,10] as describe earlier in section V.3.2. In order to emphasize, this point equation V.1 is repeated here (For detail, see section V.3.3).

$$J_c \cong \frac{\pi^{1/2} f_p r_p}{\phi_0 d^{3/2} t^{1/2}} \approx \frac{J_d r_p \xi}{d^{3/2} t^{1/2}} \propto t^{-1/2} \quad (\text{V.1})$$

This gives the inverse square root dependence $J_c \propto t^{-1/2}$ (or $I_c \propto t^{1/2}$) observed in the pure PLD films. Eq. (V.1) also can be used to estimate the mean pin spacing d from observed self-field values. Usually, the mean spacing $d \sim \xi (J_{d,p}/J_c \xi)^{2/3} (\xi/t)^{1/3}$ is 5-10 nm of the interaction radius for J_c of 2-4 MA/cm². Pinning in this case may be provided only by clusters of oxygen vacancies or cation disorder, which evidently are weak pins incapable of effectively resisting thermal fluctuations.

Figure V.25(b) illustrates *3D strong pinning* by which vortex lines can be chopped into discontinuous segments by strong pinning defects, e.g. Y211 nanoparticles. This 3D pinning case produces the thickness-independent J_c . J_c can be estimated in the strong pinning limit, for which the ends of vortices are fixed only by surface irregularities or other defects near the interface. In this case J_c is determined by depinning of a critical vortex loop

whose diameter is equal to the separation d between the fixed ends of the vortex segment [27] (Figure V.25(b)) as describe earlier in section V.4.3. The equation V.2 is repeated here.

$$J_c = \frac{\phi_0}{2\pi\mu_0\lambda_a\lambda_c d} \ln \frac{d}{\xi_c} \propto \text{const.} \quad (\text{V.2})$$

The 3D pinning behavior results in constant J_c though thickness. However, if the vortex pin density varies, as it does here near the interface of the PLD film with Y211 pins, or if there is a variable connectivity such as porosity in the MOD film, the J_c thickness dependence will be adjusted due to microstructure-dependent effects. The PLD film with Y211 dispersion exhibited the enhancement of pinning due to their denser pinning structure, including Y211 particles and stacking faults, near the interface. The MOD films showed the microstructure degradation (porosity increase), which explains its J_c reduction in the upper half of the film.

These experiments clearly show that introducing strong pinning centers can avoid 2D collective pinning and thermal fluctuation depinning effects, and drive samples into the more desirable 3D pinning regime. Strong pinning defects, such as small pores, insulating nanoparticles, and planar defects, chop vortex lines into discontinuous segments and enhance the J_c . Thus, in principle, this should permit a high and a thickness-independent J_c in thick films, provided that thickness degradation of vortex-pinning microstructure is avoided.

Some other types of YBCO films that now incorporate strong pinning centers such as BaZrO₃ [40] are also capable of putting samples into this strong 3D pinning regime. Sm-doped YBCO coated conductors made by MOCVD [32,33] also exhibits a very high

density of $(\text{Sm,Y})_2\text{O}_3$ nanoparticles which show evidence of strong 3D pinning. For these strong pinning samples, there was no evidence of thermal fluctuation effect at any thickness at which we examined them.

V.7 Summary

Using sequential ion milling the depth profiling of the critical current density $J_c(H)$ was measured for three sets of YBCO samples, including thin pure PLD samples, 1 μm thick PLD sample with Y211 dispersion, and MOD films, in order to better understand what causes the thickness dependence of J_c . It was found that the thin pure YBCO films without evident strong pinning centers exhibited clear evidence of 2D collective pinning subject to large thermal fluctuation effects. The second set of samples with strong pinning centers (Y211) exhibited a quite different J_c thickness dependence from that of the pure PLD sample. This YBCO film with fine and dense insulating nanoparticles exhibited high and uniform J_c through thickness (3D pinning behavior) except near the interface where the defect density was highly enhanced. These two sets of PLD films represent two distinctively different $J_c(t)$ behaviors, which can be deduced from the 2D collective pinning and the 3D pinning. The 2D collective pinning behavior is affected by an array of weak pinning centers, which only perturb the continuity of vortex lines. In this case, J_c decreases as $t^{-1/2}$ as film thickness increases. But in 3D pinning, strong pinning centers decouple the vortices into short segments. The J_c is high and independent of thickness, since the J_c is determined by the spacing between strong pins. The last sample set, MOD coated

conductors, exhibited a weak degradation (quasi-linear) of J_c on increasing t . It is found that the MOD films exhibited strong 3D pinning by pinning defects, including pores, insulating Y_2O_3 particles, second phase particles, and planar defects, while thickness-dependent changes in microstructure, mostly porosity which increases with thickness, were responsible for the observed weak reduction of J_c .

The production of uniform, dense arrays of nanoprecipitates is a natural route to a high J_c and a uniform through-thickness J_c . Critical current can be maximized by increasing film thickness, if the thickness degradation of pinning structure or current-carrying cross-section is avoided. The significant potential of nanoscale pinning engineering has been well illustrated both by the results of PLD film with Y211 particles. In addition, the analysis of real MOD coated conductors illuminates that the current-blocking defects or other microstructure degradation must also be avoided.

References

- [1] S. R. Foltyn, P. Tiwari, R. C. Dye, M. Q. Le & X. D. Wu, *Appl Phys Lett* **63**, 1848 (1993).
- [2] S. R. Foltyn, Q. X. Jia, P. N. Arendt, L. Kinder, Y. Fan & J. F. Smith, *Appl Phys Lett* **75**, 3692 (1999).
- [3] X. D. Wu, S. R. Foltyn, P. Arendt, J. Townsend, I. H. Campbell, P. Tiwari, Q. X. Jia, J. O. Willis, M. P. Maley, J. Y. Coulter & D. E. Peterson, *IEEE Trans Appl Supercon* **5**, 2001 (1995).
- [4] B. W. Kang, A. Goyal, D. R. Lee, J. E. Mathis, E. D. Specht, P. M. Martin, D. M. Kroeger, M. Paranthaman & S. Sathyamurthy, *J Mater Res* **17**, 1750 (2002).
- [5] J. R. Groves, P. N. Arendt, S. R. Foltyn, Q. X. Jia, T. G. Holesinger, H. Kung, E. J. Peterson, R. F. DePaula, P. C. Dowden, L. Stan & L. A. Emmert, *J Mater Res* **16**, 2175 (2001).
- [6] S. R. Foltyn, P. N. Arendt, Q. X. Jia, H. Wang, J. L. MacManus-Driscoll, S. Kreiskott, R. F. DePaula, L. Stan, J. R. Groves & P. C. Dowden, *Appl Phys Lett* **82**, 4519 (2003).
- [7] R. L. S. Emergo, J. Z. Wu, T. Aytug & D. K. Christen, *Appl Phys Lett* **85**, 618 (2004).
- [8] K. Develos-Bagarinao, H. Yamasaki, J. C. Nie & Y. Nakagawa, *Supercond Sci Tech* **18**, 667 (2005).
- [9] P. H. Kes & C. C. Tsuei, *Phys Rev B* **28**, 5126 (1983).
- [10] A. Gurevich, Presentation at http://www.energetics.com/meetings/supercon04/pdfs/presentations/f_uw_coated_conductor_peer_rev_04final.pdf
- [11] L. Civale, B. Maiorov, A. Serquis, J. O. Willis, J. Y. Coulter, H. Wang, Q. X. Jia, P. N. Arendt, J. L. MacManus-Driscoll, M. P. Maley & S. R. Foltyn, *Appl Phys Lett* **84**, 2121 (2004).
- [12] T. Ohnishi, R. H. Hammond & W. Jo, *J Mater Res* **19**, 977 (2004).
- [13] W. Wong-Ng, I. Levin, R. Feenstra, L. P. Cook & M. Vaudin, *Supercond Sci Tech* **17**, S548 (2004).

- [14] W. Wong-Ng, L. P. Cook, J. Suh, I. Levin & R. Feenstra, *Supercond Sci Tech* **18**, 442 (2005).
- [15] D. M. Feldmann, D. C. Larbalestier, R. Feenstra, A. A. Gapud, J. D. Budai, T. G. Holesinger & P. N. Arendt, *Appl Phys Lett* **83**, 3951 (2003).
- [16] T. G. Holesinger, P. N. Arendt, R. Feenstra, A. A. Gapud, E. D. Specht, D. M. Feldmann & D. C. Larbalestier, *J Mater Res* **20**, 1216 (2005).
- [17] S. R. Foltyn, H. Wang, L. Civale, Q. X. Jia, P. N. Arendt, B. Maiorov, Y. Li, M. P. Maley & J. L. MacManus-Driscoll, *Appl Phys Lett* **87**, 162505 (2005).
- [18] A. Gurevich, *private comm.*
- [19] T. S. Wang, X. F. Duan, W. F. Hu, W. Liu, L. Li, W. Peng & Y. F. Chen, *Supercond Sci Tech* **15**, 1199 (2002).
- [20] C. B. Eom, A. F. Marshall, Y. Suzuki, T. H. Geballe, B. Boyer, R. F. W. Pease, R. B. Vandover & J. M. Phillips, *Phys Rev B* **46**, 11902 (1992).
- [21] R. Feenstra, D. K. Christen, C. E. Klabunde & J. D. Budai, *Phys Rev B* **45**, 7555 (1992).
- [22] S. R. Foltyn, H. Wang, L. Civale, Q. X. Jia, P. N. Arendt, B. Maiorov, Y. Li, M. P. Maley & J. L. MacManus-Driscoll, *Appl Phys Lett* **87**, (2005).
- [23] T. L. Hylton & M. R. Beasley, *Phys Rev B* **41**, 11669 (1990).
- [24] T. Haugan, P. N. Barnes, R. Wheeler, F. Meisenkothen & M. Sumption, *Nature* **430**, 867 (2004).
- [25] S. I. Kim, Z. Chen, A. Gurevich, F. Kametani, K.-J. Choi, C.-B. Eom & D. C. Larbalestier, *unpublished*
- [26] S. I. Kim, D. M. Feldmann, D. T. Verebelyi, C. Thieme, X. Li, A. A. Polyanskii & D. C. Larbalestier, *Phys Rev B* **71**, 104501 (2005).
- [27] E. H. Brandt, *Phys Rev Lett* **69**, 1105 (1992).
- [28] K. Matsumoto, T. Horide, A. Ichinose, S. Horii, Y. Yoshida & M. Mukaida, *Jpn J Appl Phys pt 2* **44**, L246 (2005).
- [29] M. Miura, Y. Yoshida, Y. Ichino, Y. Takai, K. Matsumoto, A. Ichinose, S. Horii & M. Mukaida, *Jpn J Appl Phys pt 2* **45**, L11 (2006).

- [30] J. Gutierrez, A. Llordes, J. Gazquez, M. Gibert, N. Roma, A. Pomar, F. Sandiumenge, N. Mestres, T. Puig & X. Obradors, *Nature Materials* **6**, 367 (2007).
- [31] S. I. Kim, A. Gurevich, X. Song, X. Li, W. Zhang, T. Kodenkandath, M. W. Rupich, T. G. Holesinger & D. C. Larbalestier, *Supercond Sci Tech* **19**, 968 (2006).
- [32] X. Y. Song, Z. J. Chen, S. I. Kim, D. M. Feldmann, D. Larbalestier, J. Reeves, Y. Y. Xie & V. Selvamanickam, *Appl Phys Lett* **88**, (2006).
- [33] Z. Chen, D. M. Feldmann, X. Song, S. I. Kim, A. Gurevich, J. Reeves, Y. Y. Xie, V. Selvamanickam & D. C. Larbalestier, *to be published in Supercond Sci Tech* 2007
- [34] A. C. Westerheim, A. C. Anderson, D. E. Oates, S. N. Basu, D. Bhatt & M. J. Cima, *J Appl Phys* **75**, 393 (1994).
- [35] O. Castano, A. Cavallaro, A. Palau, J. C. Gonzalez, M. Rossell, T. Puig, F. Sandiumenge, N. Mestres, S. Pinol, A. Pomar & X. Obradors, *Supercond Sci Tech* **16**, 45 (2003).
- [36] R. Feenstra, A. A. Gapud, F. A. List, E. D. Specht, D. K. Christen, T. G. Holesinger & D. A. Feldmann, *IEEE T Appl Supercon* **15**, 2803 (2005).
- [37] M. W. Rupich, W. Zhang, X. Li, T. Kodenkandath, D. T. Verebelyi, U. Schoop, C. Thieme, M. Teplitsky, J. Lynch, N. Nguyen, E. Siegal, J. Scudiere, V. Maroni, K. Venkataraman, D. Miller & T. G. Holesinger, *Physica C* **412-14**, 877 (2004).
- [38] J. P. Clerc, G. Giraud, J. M. Laugier & J. M. Luck, *Adv Phys* **39**, 191 (1990).
- [39] L. Civale, B. Maierov, A. Serquis, S. R. Foltyn, Q. X. Jia, P. N. Arendt, H. Wang, J. O. Willis, J. Y. Coulter, T. G. Holesinger, J. L. MacManus-Driscoll, M. W. Rupich, W. Zhang & X. Li, *Physica C* **412-14**, 976 (2004).
- [40] J. L. Macmanus-Driscoll, S. R. Foltyn, Q. X. Jia, H. Wang, A. Serquis, L. Civale, B. Maierov, M. E. Hawley, M. P. Maley & D. E. Peterson, *Nat Mater* **3**, 439 (2004).

Chapter VI. Summary

The purpose of this thesis work was to explore critical scientific issues of YBCO coated conductors, especially the *current limiting mechanisms of low angle grain boundaries* and *the thickness dependence of J_c* . The study of grain boundaries started by taking a broad view of the current-limiting mechanism of the grain boundary network in real coated conductors, then transitioning to a study of how to improve low angle grain boundary supercurrent transparency by Ca^{2+} or Nd^{3+} doping using specially grown films in which segregation doping was used to control the grain boundary properties. To address the nature of vortex pinning within YBCO grains, the thickness dependence of J_c of three different types of sample from multiple sources was investigated so as to better understand the way that high critical currents can and should be built up in thick coated conductors.

VI.1 Grain Boundaries in Coated Conductors

One of the most important obstacles standing in the way of developing high current YBCO coated conductors is the current-limiting obstacle that many grain boundaries become. In order to better understand the current limiting mechanism of the polycrystalline grain boundary network in coated conductors, variously textured coated conductors were investigated. We found that the global texture exercises a significant effect on J_c especially in low fields. By cutting various width tracks ranging from several to about one grain width,

it was possible to emphasize the grain boundary dissipation, and to distinguish the magnetic field and temperature domain in which the grain boundary network controls $J_c(H,T)$, *the grain-boundary-limited* domain from that in which the grain boundary network becomes transparent and $J_c(H,T)$ becomes limited by vortex pinning in *the grain-limited* domain. The *grain-boundary-limited* domain became larger as field and temperature decreases. One striking result was that the coated conductors produced by metal organic deposition technique exhibited much attenuated grain boundary dissipative signatures for grains of a given misorientation θ , compared to typical samples made by pulsed laser deposition technique. Later, more explicit work by my colleague Matthew Feldmann, has shown that the origin of this reduced dissipation is due to the highly meandered geometry of grain boundaries formed by the *ex situ* MOD process, as opposed to the epitaxial and planar geometry of films grown by *in situ* methods such as PLD.

Even though the current-blocking influence of the grain boundary network is lessened by grain boundary meandering, the low-field performance (i.e. $J_{c,gb}$) of coated conductors is still limited by the grain-to-grain misorientation distribution of the grain boundary network. Prior to my work, *Ca doping* was known to improve the grain boundary superconducting properties by adding charge carrier density at grain boundaries, which are in general charge carrier depleted compared to the grains. In order to better understand the ability to modify GB properties, *Ca-doping in low angle (6 – 9°) grain boundaries of YBCO* was investigated. The framework for the study was established by an earlier investigation of George Daniels and Xueyan Song in our group of the influence of 30 % Ca substitutions for Y which showed a closely correlated enhancement of the transport current

density across the GB and very strong segregation of Ca to the tensile regions of the GB dislocations. Gurevich developed a model of this segregation that was in very close accord with the experimental measurement of the Ca segregation and we then used this model to consider various ways in which varying the charge and size of the substitution could affect GB segregation. My first test was to vary the Ca-doping level of quasi-ideal, single grain boundaries on bicrystals. It was found that 15% Ca substitution was more effective than the usually chosen 30% Ca substitution for enhancement of $J_{c,gb}$ in the crucial intermediate field range of 7° [001]-tilt GBs. Recall that the critical angle beyond which $J_{c,gb}$ falls off in virtually all previous experiments (the “Dimos” law) is $2-3^\circ$. I then studied the Ca-doping influence in low angle grain boundaries of the small rare-earth ion analogue of YBCO, $YbBa_2Cu_3O_{7-x}$. Significant $J_{c,gb}$ enhancement and much weaker (or no) grain boundary dissipation was observed. By showing the $J_{c,gb}$ improvement, the viability of Ca-doping approach to improve GB properties has been established. But the rather large T_c reduction due to excess charge carrier density in the grains remains the largest drawback of this Ca doping approach.

Based on the cation segregation model, Nd doping was then investigated as a way to improve $J_{c,gb}$ without significant T_c reduction. The Nd^{3+} ion is expected to segregate to the grain boundary dislocation cores, relieving the lattice distortion and recovering the missing charge carrier density near grain boundary dislocation cores that occurs for Ca^{2+} segregation. In addition, Nd^{3+} substitution for Y^{3+} (i.e. isovalent substitution) was expected to avoid degradation the T_c of grains significantly. Very interestingly, the Nd-doped YBCO exhibited the full recovery of inter-grain J_c at 6° up to its intragrain J_c without significant

T_c reduction. T_c of the samples was a little lower than normal YBCO at around 84 – 86 K, which was yet acceptable. This appears to be a film growth effect that is not fundamental since bulk samples and other films have achieved T_c values of 93 – 95 K. This work thus showed the feasibility of adopting Nd doping in real applications. Other large rare earth ions such as Gd^{3+} , Eu^{3+} , and Sm^{3+} will very likely work the same way too. This work will be completed by state-of-the-art analytical electron microscopy, including Z-contrast scanning transmission electron microscopy imaging and electron energy loss spectroscopy, to determine the segregation composition profiles and local electronic state by Dr. Yan Xin after submission of the thesis.

VI.2 Thickness dependence of J_c in Coated Conductors

Another serious obstacle in the development of high current YBCO coated conductors is loss of critical current density as YBCO films thicken. In order to better understand the J_c thickness dependence behavior, depth profiling of the critical current density $J_c(H)$ was employed for YBCO thin film samples from various sources. First, relatively thin pure YBCO films carefully grown in Professor Chang-beom Eom's group, University of Wisconsin - Madison on planar and miscut substrates at higher growth temperature by pulsed laser deposition were investigated. These films exhibited strong J_c reduction with increasing thickness, with clear evidence of 2D collective pinning affected by large thermal fluctuation effects. These films demonstrated the intrinsic limitation of critical current enhancement by thickening pure YBCO films without strong pinning

centers. In contrast, a YBCO film grown by Dr. Tim Haugan at Air Force Research Laboratory with strong pinning centers, Y_2BaCuO_5 nanoparticles, exhibited a high and uniform J_c through thickness, characteristic of strong 3D pinning behavior in the situation where the defect density is independent of thickness. (We should also note that in fact the J_c was strongly enhanced near the interface where the defect density was also highly enhanced and pinning even more effective.) These two very different YBCO film sets contrasted two distinctively different $J_c(t)$ behaviors. The last sample set were coated conductors made by American Superconductor Corporation using the metal organic decomposition technique. Such films contain various pinning defects, including pores, insulating Y_2O_3 particles, second phase particles, and planar defects which can provide strong pinning, making them conceptually similar to the strongly pinning Y_2BaCuO_5 film described above. They exhibited a weak, quasi-linear degradation of J_c on increasing thickness. The pinning defects drive their $J_c(t)$ dependence into the 3D pinning regime, but the thickness-dependent degradation in microstructure, mostly enhanced porosity at greater thickness, was found to be responsible for the degradation of J_c . Thus my broad study of the thickness dependent critical current density in 3 distinctly different types of YBCO films shows rather clearly that dense and uniform arrays of pinning defects are required to achieve the desirable 3D pinning behavior with a high and uniform J_c through thickness. In this case, the critical current of the conductor can be maximized by increasing film thickness, provided that the thickness degradation of pinning structure or current-carrying cross-section is avoided.

APPENDIX; Calculation of porosity from effective medium theory

(Alex Gurevich)

To calculate the effective resistivity ρ of a conductor with spherical pores we calculate the electric field distribution $\mathbf{E}(\mathbf{r}) = -\nabla\varphi$ in a medium with a randomly inhomogeneous conductivity $\sigma(\mathbf{r})$. The equation for the electric potential φ is:

$$\frac{\partial}{\partial x}\sigma_a\frac{\partial\varphi}{\partial x} + \frac{\partial}{\partial y}\sigma_a\frac{\partial\varphi}{\partial y} + \frac{\partial}{\partial z}\sigma_c\frac{\partial\varphi}{\partial z} = 0 \quad (\text{A1})$$

where $\sigma_a(\mathbf{r}) = 1/\rho_a$ and $\sigma_c(\mathbf{r}) = 1/\rho_c$ are the normal state conductivities along the ab plane and the c-axis, respectively between the pores and $\sigma = 0$ in the pores. Next, we transform the z coordinate along the c-axis, $z \rightarrow (\sigma_c/\sigma_a)^{1/2}z$ so that σ in Eq. (A1) cancels. In the new coordinates each pore becomes an ellipsoid stretched along the c-axis with the in-plane to the out-of-plane semi-axis ratio $\varepsilon = (\sigma_c/\sigma_a)^{1/2}$. In the EMT models the electric field distribution in a heterogeneous conductor results from local electric fields produced by randomly-distributed ellipsoids with a different local in-plane resistivities ρ_i , embedded in a uniform effective medium with the exact global resistivity ρ . The electric field in the ellipsoid is uniform and independent of its size [42]:

$$E_i = \frac{E\rho_i}{(1-n_x)\rho_i + n_x\rho} \quad (\text{A2})$$

where E is the mean electric field, and n_x is the depolarization factor of the ellipsoid along the x-axis:

$$n_x = \frac{1}{2(1-\varepsilon)} \left[1 - \frac{\varepsilon}{2\sqrt{1-\varepsilon}} \ln \frac{1+\sqrt{1+\varepsilon}}{1-\sqrt{1-\varepsilon}} \right] \quad (\text{A3})$$

Averaging Eq. (A2) with the distribution function $F(\rho_i)$ gives the main EMT self-consistency equation for the global resistivity ρ :

$$1 = \int_0^{\infty} \frac{F(\rho_i) \rho_i d\rho_i}{(1-n_x)\rho_i + n_x \rho} \quad (\text{A4})$$

If a heterogeneous conductor has a volume fraction $1 - x$ of pores with $\rho_i = \infty$ in a uniform metallic matrix with $\rho_i = \rho_a$, Eq. (A4) becomes

$$1 = \frac{x\rho_a}{(1-n_x)\rho_a + n_x \rho} + \frac{1-x}{1-n_x} \quad (\text{A5})$$

Solving Eq. (A5) for ρ , we obtain Eq. (1) with the percolation threshold, $x_c = n_x$.